RELATIVISTIC RADIATIVE HYDRODYNAMICS CALCULATION OF ACCRETION FLOW INTO SUPERMASSIVE BLACK HOLE

BY

PO KIN LEUNG

DISSERTATION

Submitted in partial fulfillment of the requirements
for the degree of Doctor of Philosophy in Astronomy
in the Graduate College of the
University of Illinois at Urbana-Champaign, 2010

Urbana, Illinois

Doctoral Committee:

Professor Charles Forbes Gammie, Chair
Professor Ronald F. Webbink
Professor Paul Milton Ricker
Professor Athol J. Kemball

Abstract

The compact radio source Sagittarius A* (Sgr A*) is the nearest and most-intensively-studied supermassive black hole candidate. With a broadband spectrum which likely requires several emission mechanisms for explanation, and structure of innermost accretion flow not yet well constrained, the understanding of accretion into Sgr A* demands advances in both theories and computational calculation.

To increase the understanding of Sgr A* in particular, and low-luminosity active galactic nuclei in general, we perform relativistic radiative transfer (RT) calculation with general relativistic magnetohydrodynamic (GRMHD) simulation of accretion flow simulation. We are able to use the models to constrain observational parameters of Sgr A*.

We also compute the synchrotron emissivity and absorptivity from first principles, in order to verify improved approximate equations for the RT calculation. The code can handle a wide range of electron distributions, therefore the application is not limited to accretion disk simulation.

In order to explain a feature in the observed flaring spectrum, we add nonthermal component to the electron distribution. We then perform relativistic Monte Carlo RT calculation of the disk model, and show that a small amount of power-law electron is enough to modify the spectral slope.

Finally, we describe a recipe for performing relativistic polarized RT, which would allow a further study to constrain model parameters with polarization observations from Sgr A*.

Reason for doing radiative transfer:

Nothing has really happened until it has been recorded.
– Virginia Woolf

Acknowledgments

First of all, I would like to thank my adviser, Charles Gammie, without whom I would not have been able to complete this dissertation. You are such an good astrophysicist. I am always amazed by the breadth and depth of knowledge and experience that you have shown in all these years. Besides scientific achievement, you are also such a great gentleman who always see the goods in others. Also, seldom do I meet a person who genuinely cares for others to such an extent. Your unselfishness is beyond description. To quote the Squeeze Toy Aliens [Pixar 1999], I am eternally grateful.

I would also like to thank Ronald Webbink, Paul Ricker, and Athol Kemball for their willingness to serve on my defense committee. It is my honor to learn from your comments and advice. Also many thanks to those who have helped me academically throughout all of these years. Any attempt to make a list is bound to fail, but I am still going to try. In rough chronological order, they are Keqing Xia, Chiu Man Ho, Ming-Chung Chu, Chung Ming Mak, Chi Wang Chan, Xiaoyue Guan, Yuk Tung Liu, Jon McKinney, Stuart Shapiro, Bryan Johnson, Scott Noble, Monika Mościbrodzka, Josh Dolence, and Hotaka Shiokawa.

I would also like to thank my beloved wife, Nicole. Your love, encouragement and support have been my major sources of energy. I am blessed to have you in my life, and I am sorry for the sacrifices that you have made during all these years. Personally I can't imagine marrying a scientist myself because there are too many uncertainties along their chosen path, and it is always hard to really understand them. To me, *Rocket Man* [John 1972] is the best description of their lives. Luckily you are not like me, and you always see me better than I really am.

Thanks to the Lord, for He has given me strength, endurance and peace. Without Him all these are not possible.

Many thanks to mom and dad, who have dedicated their lives to our welfare. Even when I was young, you were always supportive of me. You let me choose my own way, and provide the guidance and support that I need. Words simply are not enough to describe my gratitude. Thanks to my brother and sisters: Philip, Karen

and Ka. Your encouragement and care have meant a lot to me. You've always had my back, and for that I am grateful. Thanks to all other family members and friends who have been supporting me in all these years. Among them I especially like to mention Chi Yat Hong, who believed in me even when I did not. Uncle Edward, Aunt Teresa and Joyce Lam are always encouraging. Other good friends who have been supporting me include Chiu Man Ho, Samantha Wong, Chung Ming Mak, Chi Wang Chan, Leo & Anne Chan, Patrick Chan, Florrie Ng, David Wong, Christine Tang, Jacky Lie, Shirley Cheng, Alex Kong, and Jessica Kuong. I am also thankful for the friendship of people in the "UIUC CUHK Physics Alumni Association", ICCF and CCCC. Whenever I am in need, so many of you just offer help without asking any question.

Last but not least, thanks to the Astronomy Department and the Physics Department, for providing me with financial means to pursue my dream.

Table of Contents

List of Tables

List of Figures

List of Abbreviations

ADAF	Advection-dominated accretion flow
AGN	Active galactic nucleus
BH	Black hole
BB04	Broderick & Blandford 2004
CDF	Cumulative density function
CP	Circular polarization
FF	Fluid frame
GCF	Guiding center frame
GR	General relativity
GRMHD	General relativistic magnetohydrodynamic
IR	Infrared
ISM	Interstellar medium
LINER	Low ionization nuclear emission-line region
LLAGN	Low-luminosity AGN
LP	Linear polarization
MBS	Magneto-bremsstrahlung
MHD	Magnetohydrodynamic
MRI	Magnetorotational instability
NIR	Near infrared
PDF	Probability density function
QSO	Quasi-stellar Object

SED	Spectral energy distribution
RT	Radiative transfer
RIAF	Radiatively inefficient accretion flow
Sgr A*	Sagittarius A*
VLBI	Very-Long-Baseline Interferometry
WKB	WentzelKramersBrillouin (approximation)

Chapter 1

Introduction

1.1 Low-luminosity AGN

Active Galactic Nuclei (AGNs) are the central energetic compact regions of galaxies for which the bright emission cannot be accounted for only by stars and interstellar medium (ISM). Among the common AGN subclasses are quasars, Seyfert galaxies, quasi-stellar objects (QSOs), BL Lacs objects, radio galaxies and Low Ionization Nuclear Emission-line Regions (LINERs). As with any kind of classification, there are overlaps in the categories. There are also sub-categories and exceptional cases; AGNs come in many different forms, and show a large variety in broadband spectra and line emission.

Despite the vast diversity in the observational properties among different types of AGNs, efforts to construct a unified model of AGN have had moderate success through the years [see Tadhunter, 2008, Urry, 2003, for review]. The unified models suggest that different types of AGNs are similar objects at different evolutionary stages and at different orientation angles. Now the general understanding is that all AGNs (indeed, virtually all galaxies) host a supermassive black hole (mass $M_{\rm BH} \geq 10^6 M_\odot$) and an accretion disk. Many models also include a relativistic jet which extends from the region near the black hole to up to tens of kpc.

Besides the "classical" AGNs, there are situations in which the galactic nuclei are relatively dim, both relative to the Eddington luminosity $L_{\rm edd} \equiv 1.5 \times 10^{44}$ erg s^{-1} $(M_{\rm BH}/10^6 M_\odot)$, and relative to the host galaxy as a whole. The structure of the accretion disk in a low-luminosity AGN (LLAGN) could be different from that in a quasar. Among the LLAGNs, the most carefully observed objects are Sagittarius A* (Sgr A*) and M87.

1.1.1 Sagittarius A*

The Galactic center contains a high density of stars and plasma within a small region, which is coincident with the location of a compact and powerful radio source called Sgr A*. By measuring the orbits of the short-period stars, the enclosed mass is estimated to be $4.1 \times 10^6 M_\odot$ [Ghez et al., 2008, Gillessen et al., 2009], and distance is 8.4 kpc [Reid et al., 2009]. Very-Long-Baseline Interferometry (VLBI) measurements provide a constraint of the size of the source, which implies the mass density is at least $9.3 \times 10^{22}\ M_\odot\ \mathrm{pc}^{-3}$ [Doeleman et al., 2009]. The evidence that Sgr A* is a supermassive black hole is compelling [1]. Most alternate theories are ruled out by applying dynamical constraints to the measured mass and density [Maoz, 1998]. See Genzel, Eisenhauer, & Gillessen [2010] for a review of why the alternatives are ruled out.

Sgr A* is the most studied supermassive black hole candidate. One of the reasons is that it is relatively easy to observe due to its angular size and proximity. The Schwarzschild radius of Sgr A* is about 0.1 AU, which corresponds to an (unlensed) angular size of 10 μas. Its angular scale is twice as large as the next largest black hole candidate, M87. The close distance also allows Sgr A* to be observed with high angular resolution. Recent VLBI observations have achieved a resolution which could be just enough to resolve the black hole event horizon. The 1.3 mm VLBI observations indicate that the intrinsic diameter of Sgr A* is 37^{+16}_{-10} μas, whereas the minimum apparent diameter (due to gravitational lensing) is 52 μas [Doeleman et al., 2009]. It is possible that most of the emission from Sgr A* may not be centered on the black hole [Doeleman et al., 2009].

As stated before, an intriguing property of Sgr A* is its low luminosity. In fact it is the faintest in terms of Eddington luminosity among the known supermassive black hole candidates. The bolometric luminosity of Sgr A* is at least 7 order of magnitude below the Eddington limit [Baganoff et al., 2003, Ghez et al., 2005]. Most of the energy emitted from the system is at sub-millimeter (sub-mm) wavelengths. The emission in X-rays is about 2 order of magnitude fainter, and therefore $L_\mathrm{X}/L_\mathrm{edd} \lesssim 10^{-9}$.

1.1.2 Emission from Sgr A*

According to observations, most of the time Sgr A* is in a steady, quiescent state. Figure (1.1) shows a compilation of the observations. The quiescent state has been detected in radio to sub-mm. There are also claims of detection at near infrared (NIR)

[1] We use the name Sgr A* loosely as the light source and also the unseen central mass.

and X-ray. Upper limits are determined at mid-infrared (MIR) and NIR. One of the dominant features is the "sub-millimeter bump", which is commonly believed to be produced by thermal synchrotron emission [Özel, Psaltis, & Narayan, 2000, Yuan, Quataert, & Narayan, 2003]. On the low-frequency side of the bump, the emission in radio and centimeter could originate from power-law synchrotron emission from the extended accretion disk at $r \gg GM/c^2$ [Mahadevan, 1998, Özel, Psaltis, & Narayan, 2000]. On the high-frequency side in the infrared (IR) wavelengths, strong flares have been detected [Genzel et al., 2003, Schödel et al., 2007]. Due to the enormous extinction, there is currently no observational data around the ultraviolet band, where it is believed the first Compton-scattering bump should be located. In the X-rays, a low-luminosity quiescent state has been observed.

On top of the quiescent state, Sgr A* also has flares that last for up to about three hours. Flares were first detected in the X-rays [Baganoff et al., 2001], then in the NIR band [Genzel et al., 2003, Schödel et al., 2007] and most recently in the sub-mm [Marrone et al., 2008] and radio bands [Yusef-Zadeh et al., 2008]. A NIR flare has about a factor of 10 increase in brightness [Genzel et al., 2003], while the flux of Sgr A* can increase by over 100 times in an X-ray flaring event [Eckart et al., 2004, Porquet et al., 2003]. The NIR flares occur a couple of times each day [Eckart et al., 2006, Yusef-Zadeh et al., 2006]. The X-ray flares have a lower rate of about once per day [Baganoff et al., 2003]. There is not enough data to determine the rate of sub-mm flares.

It is natural to suspect that flares at different frequencies are related. In fact, all X-ray flares are associated with NIR flares [Eckart et al., 2004, 2006, Yusef-Zadeh et al., 2006], whereas NIR flares can occur independently [Hornstein et al., 2007]. X-ray flares occur simultaneously with NIR flares [Eckart et al., 2004, 2006, Yusef-Zadeh et al., 2006]. It is claimed that radio flares occur about 20 minutes after X-ray flares, and sub-mm flares occur about 100 minutes after an X-ray flares [Yusef-Zadeh et al., 2008].

To further complicate the picture, quasi-periodic oscillations (QPOs) with a period of 20 minutes have been claimed in the NIR and X-rays [Aschenbach et al., 2004, Belanger et al., 2006, Genzel et al., 2003, Meyer et al., 2006]. However, newer statistical analyses do not find a significant indication of QPO in the NIR [Do et al., 2009, Meyer et al., 2008]. Meyer et al. [2008] also claim that quasi-periodicities in the X-rays are ruled out statistically, but they only reference an unpublished work. It is still under debate whether quasi-periodic sub-structure does exist.

Spectra of flares have also been observed. The NIR νL_ν spectral indices are

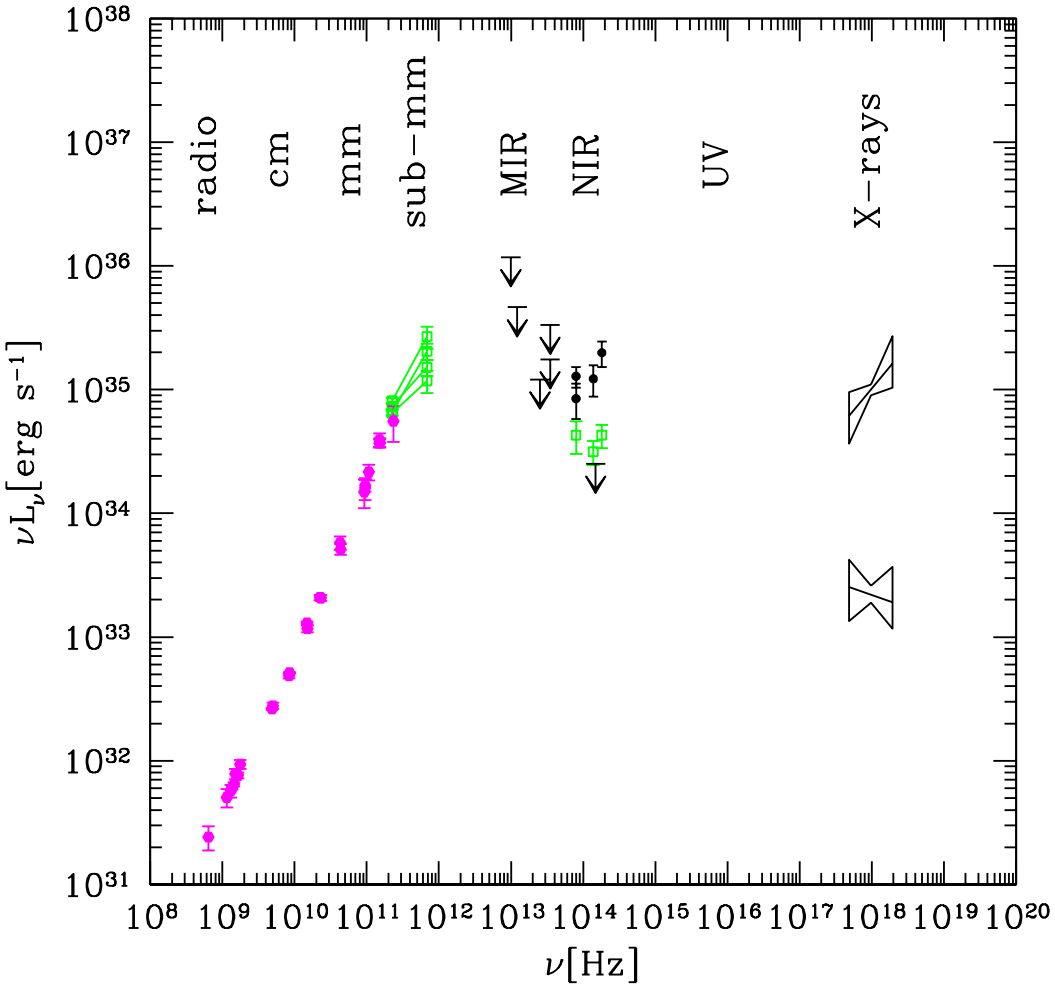

Figure 1.1 Compilation of quiescent and flaring observations of Sgr A* from radio to X-ray regime. Quiescent data from the left to the right are from An et al. [2005], Falcke et al. [1998], Marrone et al. [2006] at radio bands, Genzel et al. [2003] at NIR and Baganoff et al. [2003] at X-rays. Upper limits at NIR are from Hornstein et al. [2007], Melia & Falcke [2001], Schödel et al. [2007]. Flaring data are from from Dodds-Eden et al. [2009], Genzel et al. [2003] at NIR, and Baganoff et al. [2001] at X-ray.

claimed to be positive ($\simeq 0.4$) for strong flares [Gillessen et al., 2006, Hornstein et al., 2007] and negative for weak flares [Eisenhauer et al., 2005, Krabbe et al., 2006]. Some X-ray flares are reported to have a positive spectral index [Porquet et al., 2008]. However, more data are needed to show whether all X-ray flares have the same spectral properties.

1.1.3 Polarization of Sgr A*

Besides the unpolarized observations, polarization of emission from Sgr A* is also measured. Information contained in the polarized radiation is important for understanding the emission mechanism and the disk structure. For example, synchrotron emission is expected to be highly polarized, especially if the magnetic field configuration is coherent across the source. Polarized radiation is also produced by Compton scattering, which provides further information to probe the condition near to the source.

In the radio band, linear polarization (LP) is not detected ($< 0.1\%$) while circular polarization (CP) is found to be up to $\sim 0.1\%$ [Bower et al., 2001] in the quiescent state. This is different from high-luminosity AGNs which typically have larger LP compared to CP [Bower et al., 2001, Bower, 2003]. During flaring events, LP in the radio band could be as high as $\sim 1\%$ [Yusef-Zadeh et al., 2007, 2008]. LP of Sgr A* is found to be 2.1% in the mm regime [Macquart et al., 2006] and about 10% in the sub-mm band [Aitken et al., 2000, Marrone et al., 2007]. However, no CP is detected at sub-mm frequencies [Marrone et al., 2006]. NIR flares are found to be highly polarized [up to $\sim 20\%$; Eckart et al., 2006].

Below sub-mm bands, LP is small and the CP fraction is an increasing function of frequency [Aitken et al., 2000, Bower et al., 2001, Bower, 2003, Sault & Macquart, 1999]. This is counter-intuitive because both synchrotron radiation and Faraday conversion produce a large LP and a CP fraction that drops as frequency increases.

Polarization information also allows one to understand conditions along the line of sight from Sgr A*. It is now possible to measure Faraday rotation, which is the frequency-dependent change of polarization orientation. Marrone et al. [2007] find that the rotation measure RM $= -(5.6 \pm 0.7) \times 10^5$ rad m^{-2} between 227 and 343 GHz. Another observation constrains RM between 22 to 43 GHz to $\sim -2.5 \times 10^3$ to 5×10^5 rad m^{-3}, depending on the detailed assumption [Yusef-Zadeh et al., 2007].

1.1.4 Comparison of Sgr A* and M87

M87 is another underluminous AGN (in terms of its Eddington value). The mass of the central supermassive black is $3.4 \times 10^9 M_\odot$, which is significantly heavier than Sgr A*. Therefore, even though M87 is much further away (~ 16 Mpc) than Sgr A*, the angular diameter of M87's event horizon is only about half as large as Sgr A*.

There are many differences between M87 and Sgr A*. Due to the larger mass of M87, the dynamical timescale is about 5 hours and the orbital timescale at the

innermost stable circular orbit (ISCO) is of order days. Both are much longer than the corresponding timescale for Sgr A*. Therefore observations of M87 could have higher temporal resolution (in terms of timescales of the object) compared to that of Sgr A*.

Another major difference between M87 and Sgr A* is M87's prominent relativistic jet; it is one of the closest radio galaxies with a bright radio jet. Because we are on the galactic plane, observation of Sgr A* is obscured in different levels throughout the spectrum. On the other hand, there is no evidence of interstellar scattering of sub-mm and mm observations of M87 [Broderick & Loeb, 2009].

1.2 Accretion flow

So far we have discussed the properties of LLAGNs in general, and Sgr A* and M87 in particular. We now have to explain details of accretion flow, which is a central concept in AGN models. While it is obvious that accretion of matter could occur when the gravity of the central object dominates, the details and geometry of accretion are not trivial.

We will first introduce the simplest model of the flow, namely steady spherically symmetric accretion. It captures a lot of the physics found in more complicated situations, despite its simplicity. We will then discuss accretion flow in a disk. One of the limits is the thin disk, in which the thickness is much smaller than the radius. This approximation allows one to greatly simplify the calculation of flow structure, especially if one parametrizes the angular momentum transport with a single parameter. Although the thin disk model is simple and it has been successfully applied to classical AGNs, it may not represent the physical conditions of accretion around LLAGNs. We will also discuss the geometrically thick disk, which is more realistic in slowly accreting systems such as Sgr A* and M87.

1.2.1 Spherical accretion

Let us consider an idealized situation in which an isolated central mass is surrounded only by interstellar medium (ISM) that extends to infinity, and furthermore the accretion is independent of time. Any property that could lead to asymmetry—such as spin of the central object, angular velocity of ISM with respect to the central mass, and magnetic field—is assumed to be negligible. If the luminosity of the central mass is smaller than the Eddington limit, at which the radiation force on the ISM ex-

ceeds the gravitational pull, then the surrounding matter will fall towards the center. While this scenario is simple, it may crudely model the accretion at large distance from a supermassive black hole, and also provides some insights that are applicable to non-spherical accretion flow.

The governing fluid equations of an accretion flow, like any fluid motion, are the continuity equation, the Euler equation and the energy equation. They express conservations of mass, momentum and energy respectively. The steady condition means that the time derivatives in the equations are zero. Then the accretion flow can be described by a 1D model such that all fluid variables are functions of radius R. While the continuity and Euler equations are differential equations in R, the energy equation is commonly replaced by the equation of state, which is parametrized by Γ if a Γ-law gas, $p = (\Gamma - 1)u$, is assumed (here u is the internal energy).

This accretion problem is known as Bondi accretion because it was first solved by Bondi [1952]. The details of solving the set of fluid equations can be found in Frank, King, & Raine [2002]. Here we only review the major features of the flow structure. The ISM at a large distance r from the central mass has velocity $v = 0$. As r decreases, the gas is further down the gravitational well and v increases monotonically. Velocity eventually becomes supersonic ($v > c_{\rm s}(r) \equiv$ sound speed) inside the sonic point. The mass accretion rate is $\dot{M} = \pi G^2 M^2 (\rho_\infty / c_{s,\infty}^3) f(\Gamma)$, whereas $f(\Gamma)$ is a dimensionless factor of order unity.

One of the lesson for accretion onto AGN is that $\dot{M}$ and in fact the flow structure depend on the property of the gas. An isothermal ($\Gamma = 1$) accretion flow therefore is different from an adiabatic ($\Gamma = 5/3$) flow, even if both flows have the same central mass and initial conditions. Interaction of outgoing radiation with the accretion flow can also modify $\dot{M}$. Besides, to find a meaningful value of $\dot{M}$ of an AGN, one should consider a large distance at which the gravitational influence of the central black hole is unimportant. Finally, the accretion flow eventually becomes supersonic when the inflowing matter is close enough to the black hole.

1.2.2 Accretion disk

While spherical accretion onto a central gravitating object could be a good approximation at large distance, the accreting matter in general has nonzero angular momentum that prevents it from falling directly onto the central object. A disk-like structure is formed as the gas and plasma spiral in. Although it is common to use the word disk, the flow can actually have a height-to-radius ratio of order unity. Then instead of a

pancake-like disk, the accretion flow forms a donut-like torus. The exact geometry and structure of the disk depend on many factors such as the accretion rate and properties of the accreting matter.

Before we move on with our discussion of disk models, notice that it is not *just* a theoretical exercise, because accretion disks have been directly observed in many vastly different systems. Examples range from protostars such as HH30 [Burrows et al., 1996] and Cepheus A HW2 [Patel et al., 2005], to centers of elliptical galaxies such as NGC 4261 [Jaffe et al., 1993], to centers of spiral galaxies such as NGC 4388 [Yoshida et al., 2002]. There are also other lines of evidence such as spatially resolved maser emission from NGC 4258 [Herrnstein, Greenhill, & Moran, 1996, Herrnstein et al., 2005] and spatially unresolved Fe Kα line from BLRG 4C 74.26 [Ballantyne & Fabian, 2005]. There is no doubt that accretion disks are of great importance in the understanding of many astronomical systems.

Thin accretion disk

We have already talked about Bondi accretion, in which a 1D model is sufficient to solve the flow structure due to the symmetric property of the system. Now we go to thin-disk limit, which allows one to treat the accretion flow as a 2D structure. A steady, azimuthally-symmetric, thin disk is the situation that the disk is geometrically thin, and the disk structure is independent of time. In such case the governing equations reduce from differential equations to algebraic equations.

Here we first provide the conditions for "steadiness" and "thinness", then we move on to discuss the governing equations and a particular thin disk model. Matter drifts towards the center due to angular momentum transport, which is often modeled as turbulent transport within the disk by a "viscosity" ν. Therefore, disk structure changes in the radial direction on the viscous timescale $t_{\rm visc} \sim R^2/\nu$, which depends on the radius R and kinematic viscosity ν (not to be confused with frequency that is also represented by ν in this thesis). A disk is steady if the evolution time scale is longer than $t_{\rm visc}$.

The condition for "thinness", on the other hand, depends on the vertical structure. A thin disk is formed when the matter has subsided vertically into the central plane. Then hydrostatic balance implies

$$\frac{1}{\rho}\frac{\partial P}{\partial z} = -\frac{GM}{R^3}z = -\Omega^2 z, \tag{1.1}$$

where ρ is density, P is pressure, G is gravitational constant, M is the mass of central

object, and $\Omega = \sqrt{GM/R^3}$ is the Keplerian angular velocity. The last equality in equation (1.1) is only true for Keplerian disk, though it is commonly used as an approximation when one does not have better knowledge about the angular velocity. The scale height of the disk can then be defined as $H = (1/P)\partial P/\partial z$. Here we assume the isothermal condition, otherwise equation (1.1) cannot be solved without the energy equation. With the definition of isothermal sound speed $c_s^2 = P/\rho$, one has

$$\frac{H}{R} = c_s \left(\frac{R}{GM}\right)^{1/2}. \tag{1.2}$$

A disk is thin if $H/R \ll 1$. Then the thin disk condition can also be written as

$$c_s \ll \left(\frac{GM}{R}\right)^{1/2}. \tag{1.3}$$

In other words, the disk has to be sufficiently cold in order to be thin.

The governing equations again include the time-independent forms of the fluid dynamics equations such as equation (1.1). In addition, a radiative transport model is needed to find temperature as a function of z. Finally a model for turbulent transport of angular momentum is needed, because the aforementioned inward drifting of matter is a result of the presence of kinematic viscosity ν in the equations. One popular recipe is to parametrize ν as

$$\nu = \alpha c_s H, \tag{1.4}$$

which results in the famous α-disk model.

Now that we have the thin-disk condition, let us put our thin-disk discussions into perspective. Luminosity is high (relative to Eddington) for classical AGNs, and the accreting matter is cooled efficiently by radiating away the internal energy [2]. Therefore the disk is cold and a thin-disk approximation can be applied. However, as one lowers the luminosity of an AGN, the more internal energy is "trapped" in the gas and the temperature raises. At some point the thin-disk approximation breaks down [3]. This is exactly the case of a LLAGN. The disks of Sgr A* and M87 are therefore geometrically thick (H/R is of order unity).

[2] This statement is not entirely true because the thin-disk condition breaks down near to the black holes if mass accretion rate is large [Chen et al., 1995]. However, even for those cases, except for the innermost region, the accretion disk can still be described by the thin-disk model.

[3] Besides thin-disk and thick-disk models, there are a branch of models that consider the case that luminosity is comparable to the Eddington value [Bjoernsson et al., 1996, Chen et al., 1995]. Those are known as slim disks. We choose not to discuss those models to reduce complication in the discussion.

Thick accretion disk

Now we switch focus and discuss the thick accretion disk, or torus. In our previous discussion of thin accretion disks, we have already briefly mentioned thick disk. Notice that we have in fact made an implicit assumption that the disk is formed in an AGN, but in fact it is possible for thick accretion disks to form around other astrophysical objects (e.g. in massive star formation [Banerjee & Pudritz, 2007]). However, those thick disks could have different properties compared to what we describe here (except that $H/R \sim 1$, by definition).

In this section, we summarize the properties of a thick disk. Then we discuss the details of a type of theoretical models which can explain the geometry of the flow and the emission properties.

As we now understand from previous sections, thick disks are underluminous in terms of its Eddington value. In other words, the emission is only a small portion of the energy in the accreting matter. Without a very low radiative efficiency, most of the gravitational potential energy released by the accreting matter is converted into heat. Therefore thick disk is very hot. At the event horizon, the temperature of proton is $T_{\rm p} \sim GMm_{\rm p}/(3k_{\rm B}R) = m_{\rm p}c^2/(6k_{\rm B}) \sim 10^{12}$ K. The temperature of electron is less certain. If the estimated densities around Sgr A* and M87 are to believed, Coulomb collisions alone are not enough to equalize the temperatures of proton and electron. However, plasma instabilities may equalize the temperatures. The exact electron temperature also depends on whether shocks and magnetic reconnection are important.

There are many attempts to construct theoretical models of thick accretion disks. Due to their low luminosity, it is only natural that such models are called radiatively inefficient accretion flows (RIAFs). One of the most popular models is an advection-dominated accretion flow (ADAF), due to its relatively simple analytical form. The name itself is a bit misleading because Bondi accretion and RIAFs are all advection-dominated. In fact, ADAFs refer to models that include quasi-spherical flow structure, rotation, α-viscosity, and a two-temperature plasma [Narayan, 2002].

ADAFs assume at least two parameters. The first one is the dimensionless viscosity parameter α, which also enters $\dot{M} \sim \alpha \dot{M}_{\rm B}$, where $\dot{M}_{\rm B}$ is the accretion rate in a Bondi flow far away from the center. Typical value of $\alpha \sim 0.1$ leads to a small $\dot{M}$ in the Eddington value. Another parameter, δ, is the fraction of the turbulent energy heating of the electrons, is typically chosen to be ~ 0.01 for quiescent models. Later models introduced other parameters, such as one that allows the density scaling to deviate from that for spherical accretion because of outflows. The choices of these

parameters allow ADAFs to account for the broadband spectrum and the low luminosity of Sgr A*. The comparison of ADAFs with observation suggested that both a low accretion rate and a low radiative efficiency are important to explain why Sgr A* is very dim.

Despite the success of ADAFs and other analytic RIAF models, they are time-independent by nature and could not explain the time variation observed in Sgr A* and M87. They also do not contain information about the turbulent flow and magnetic field structure, which could be important in the predicting the emission from the accretion flow. Therefore there have been efforts in recent years to perform global, time-dependent numerical simulations of thick disks.

Besides the progress of numerical method and improvement of computational power in recent years, there are two major reasons why simulations of thick accretion disks are feasible. First reason is that radiation is dynamically unimportant in the system. This simplifies the calculation, and allows post-processing of accretion flow simulation to produce spectra and images. Another reason is that the geometry allows one to resolve the flow structure relatively easily. A thin disk with $H \ll R$, on the other hand, requires a large number of zones in the vertical direction.

1.3 Emission and radiative transfer

We have learned about how thick accretion disk models are applicable to the LLAGNs such as Sgr A* and M87. Then the next questions are: How do we predict the spectrum and image of the models? The answer consists of two closely related parts. In this section, first we discuss how radiation is produced at the accretion disk by various emission and absorption processes. Then we are going to answer the second part of the question, namely, the details of how radiation is transported to us.

1.3.1 Synchrotron radiation

Thick accretion disk is relativistically hot and ionized. Magnetic field also exists naturally in the system. Therefore synchrotron radiation, which is due to acceleration of relativistic charged particles by magnetic field, is one of the major emission mechanisms. Since electrons are much lighter than protons despite having the same charge, most of the emission comes from electrons, unless electron temperature is much lower than proton temperature in a particular disk model.

One of the ways to calculate synchrotron emission is to consider the classical

Liénard-Wiechert potentials, as seem by a distant observer. By assuming a constant energy loss rate from an accelerated electron, one can calculate the so-called single-particle emissivity. In real life, electrons have a range of energy and direction (with respect to magnetic field lines). The total emissivity is found by integrating the single-particle emissivity over the electron distribution function.

For an electron with Lorentz factor γ, the synchrotron radiation is concentrated in a narrow cone (with opening angle $\Delta\theta \sim 1/\gamma$) in the direction of motion. Consider a group of electrons moving in random direction, the emission will be linearly polarized to a high degree because the net electric vector oscillates perpendicular to the magnetic field line. This is a reason that magnetic field geometry in an accretion disk is important in the prediction of polarized radiation.

For Sgr A*, it is found that power-law synchrotron emission from the extended disk can account for the radio spectrum. The sub-mm bump, can be predicted by synchrotron emission from thermal electrons in the innermost (within tens of Schwarzschild radii) part of the disk.

1.3.2 Other emission mechanisms

Unlike synchrotron emission, bremsstrahlung does not depend on magnetic field in the plasma. Bremsstrahlung, or free-free radiation, is produced when a charge is accelerated by the Coulomb field of another particle. For Sgr A*, it is expected that bremsstrahlung from the outer disk will produce X-ray emission, probably observable during the quiescent state.

Another possible emission mechanism is pair production. When temperature is very high, virtual photons can produce electron-positron pairs, which then collide and produce gamma ray photons. It is unclear whether pair production is important in the disk or the relativistic jet.

1.3.3 Radiative transfer

With an accretion disk model, and ways of calculating the emission, we are now in a position to talk about how the radiation transports from the LLAGNs to the observer. The radiative transfer (RT) equation is basically the Boltzmann equation. The basic form of the RT equation, which consists of a source term describing emission

of radiation, and a sink term describing absorption [4], can be written as

$$\frac{dI_\nu}{ds} = j_\nu - \alpha_\nu I_\nu \ , \tag{1.5}$$

where I_ν is the specific intensity, or radiation energy within a solid angle $d\Omega$ crossing area dA in time dt and in frequency range $d\nu$, j_ν is the emissivity, and α_ν is the absorption coefficient.

An important concept related to RT is optical depth τ_ν. Consider the special case of equation (1.5) that emissivity is zero, the specific intensity drops by an e-fold over a distance l, when $\tau_\nu \equiv \alpha_\nu l = 1$. Therefore $\tau_\nu > 1$ is referred to as optically thick, whereas $\tau_\nu < 1$ is optically thin.

This concept has an important implication both to the observation, and to the numerical calculation of Sgr A*. RIAF models predict a density that is optically thin in radio and sub-mm, until very close to the central black hole. In fact, it is possible to observe the image of Sgr A* in radio bands by VLBI, up to a scale comparable to the Schwarzschild radius of the black hole. Numerically, in order to produce the image and spectrum around sub-mm bump, it is possible to simulate only the disk up to tens of Schwarzschild radii, and perform radiative transfer for the simulation data.

Equation (1.5) is a simplification in two ways. First, due to the strong gravity near to the black hole, relativistic form of equation (1.5) has to be used in the calculation. Effects such as gravitational redshift and ray bending are included naturally in the relativistic RT equation. The so-called "silhouette" of the central black hole is also produced by gravitational lensing, which is predicted by calculation using the relativistic RT equation.

Second, Compton scattering is ignored in equation (1.5). For Sgr A*, scattering is not important in the radio and sub-mm bands, but it can dominate the spectrum at smaller wavelength. For Sgr A*, it is expected that Compton scattering of photons in the sub-mm bump will produce a lower bump at ultraviolet. It is also possible that Compton scattering contributes to the X-ray emission, especially in the flaring state.

Finally, if one wants to calculate the polarization from an accretion disk, one needs to generalize equation (1.5) to the polarized RT equation. For nonrelativistic calculation, instead of the total intensity, the Stokes parameters are needed to describe the state of polarization.

[4] In general, there is also stimulated emission, which is not important in our application.

1.4 Summary of the thesis

In the last few sections we first discussed the observational data of Sgr A* in particular, and LLAGNs in general. Then we developed the arguments suggesting the thick-disk model is applicable to LLAGNs. We also explained the different ingredients needed for a RT simulation of an accretion disk. Here we give a very brief introduction of how different chapters in this thesis are related in this study.

In chapter 2 of this thesis, we describe an unpolarized RT calculation from a general relativistic magnetohydrodynamic (GRMHD) simulation of an accretion disk, with application to Sgr A*. Only thermal electrons are included in the study. We provide simulated images of the disk, observed at different orientation angles. We also compare our simulated spectra with observational data, which allow us to constrain the spin and orientation of the system. We also analyze jets in our disk simulation.

Emissivity j_ν and absorptivity α_ν are needed in the RT calculation. For numerical purpose, simple approximate equations are used. However, some of the equations from the literature are not accurate enough for our study. Therefore, in order to estimate the errors produced by the approximate equations, we perform the extra calculation of j_ν and α_ν. We also find an improved approximate equation for thermal emissivity. The efforts are described in chapter 3.

With the improved approximate equation, Mościbrodzka et al. [2009] calculated the spectrum by RT, and performed a parameter survey to find the best-bet model of the quiescent state of Sgr A*. Only thermal electrons were included in the calculation. In chapter 4 we include nonthermal component to the electron distribution, in order to explain a feature in the observed flaring spectrum. With a code that calculates the exact j_ν and α_ν, we are able to test the accuracy of power-law approximate equations.

The next natural step is to use the polarized observations to constrain the accretion flow at Sgr A*. In chapter 5 we describe a recipe of the relativistic polarized RT equation. That would allow a future study of the polarized emission from Sgr A*.

1.5 References

Aitken, D. K. et al. 2000, ApJ, 534, L173

An, T., et al. 2005, ApJ, 634, L49

Aschenbach, B., et al. 2004, A&A, 417, 71

Baganoff, F. K., et al. 2001, Nature, 413, 45

Baganoff, F. K., et al. 2003, ApJ, 591, 891

Ballantyne, D. R. & Fabian, A. C. 2005, ApJ, 622, L97

Banerjee, R., & Pudritz, R. E. 2007, ApJ, 660, 479

Belanger, G., et al. 2006, J. Phys. Conf. Ser., 54, 420

Bjoernsson, G., et al. 1996, ApJ, 467, 99

Bondi, H. 1952, MNRAS, 112, 195

Bower, G. C., et al. 2001, ApJ, 571, 843

Bower, G. C. 2003, Astro. and Space Sci., 288, 69

Broderick, A. E. & Loeb, A. 2009, ApJ, 697, 1164

Burrows, C. J., et al. 1996, ApJ, 473, 437

Chen, X., et al. 1995, ApJ, 443, 61

Cotera, A. et al. 1999, ASP Conf. Ser., 186, 240

Do, T., et al. 2009, ApJ, 691, 1021

Dodds-Eden, K., et al. 2009, ApJ, 698, 676

Doeleman, S. S., et al. 2009, Nature, 455, 78

Eckart, A., et al. 2004, A&A, 427, 1

Eckart, A., et al. 2006, A&A, 450, 535

Eckart, A., et al. 2006, A&A, 455, 1

Eckart, A., et al. 2006, J. Phys. Conf. Ser., 54, 391

Eisenhauer, F., et al. 2005, ApJ, 628, 246

Falcke, H., et al. 1998, ApJ, 499, 731

Frank, J., King, A., & Raine, D. 2002, Accretion Power in Astrophysics, 3rd ed. (Cambridge: Cambridge)

Genzel, R., et al. 2003, Nature, 425, 934

Genzel, R., Eisenhauer, F., & Gillessen, S. 2010, submitted to Rev. Mod. Phys.; arXiv:1006.0064

Gezari, D. 1999, ASP Conf. Ser., 186, 234

Ghez, A. M., et al. 2005, ApJ, 620, 744

Ghez, A. M., et al. 2008, ApJ, 689, 1044

Gillessen, S., et al. 2006, ApJ, 640, L163

Gillessen, S., Eisenhauer, F., Trippe, S., Alexander, T., Genzel, R., Martins, F., & Ott, T. 2009, ApJ, 692, 1075

Herrnstein, J. R., Greenhill, L. J., & Moran, J. M. 1996, ApJ, 468, L17

Herrnstein, J. R., Moran, J. M., Greenhill, L. J., & Trotter, A. S. 2005, ApJ, 629, 719

Hornstein, S. D. et al. 2002, ApJ, 577, L9

Hornstein, S. D., et al. 2007, ApJ, 667, 900

Jaffe, W., Ford, H. C., Ferrarese, L., van den Bosch, F., O'Connell, R. W. 1993, Nature, 364, 213

Krabbe, A., et al. 2006, J. Phys. Conf. Ser., 54, 406

Macquart, J.-P., et al. 2006, ApJ, 646, L111

Mahadevan, R. 1998, Nature, 394, 651

Maoz, E. 1998, ApJ, 494, L181

Marrone, D. P., et al. 2006, J. Phys. Conf. Ser., 54, 354

Marrone, D. P., Moran, J. M., Zhao, J.-H., & Rao, R. 2006, ApJ, 640, 308

Marrone, D. P., et al. 2007, ApJ, 654, L57

Marrone, et al. 2008, ApJ, 682, 373

Melia, F., & Falcke, H. 2001, ARA&A, 39, 309

Meyer, L., et al. 2006, A&A, 458, L25

Meyer, L., et al. 2008, ApJ, 688, L17

Mościbrodzka, M., Gammie, C. F., Dolence, J. C., Shiokawa, H., & Leung, P. K. 2009, ApJ, in press

Narayan, R. 2002, ESO Sym.: Lighthouses of the Universe, 405

Özel, F., Psaltis, D., & Narayan, R. 2000, ApJ, 541, 234

Patel, N. A., et al. 2005, Nature, 437, 109

Porquet, D. et al. 2003, A&A, 407, L17

Porquet, D. et al. 2008, A&A, 488, 549

Reid, M. J., et al. 2009, ApJ, 700, 137

Sault, R. J., & Macquart, J.-P. 1999, ApJ, 526, 85

Schödel, R. et al. 2007, A&A, 462, L1

Serabyn, E. et al. 1997, ApJ, 490, L77

Sharma, P., Quataert, E., & Stone, J. M. 2007, ApJ, 671, 1696

Tadhunter, C. 2008, New Astronomy Reviews, 52, 227

Urry, C. M. 2003, ASP Conf. Series, 311, 49

Yoshida, M., et al. 2002, ApJ, 567, 118

Yuan, F., Quataert, E., & Narayan, R. 2003, ApJ, 598, 301

Yusef-Zadeh, F., et al. 2006, ApJ, 644, 198

Yusef-Zadeh, F., et al. 2007, ApJ, 668, L47

Yusef-Zadeh, F., et al. 2008, ApJ, 682, 361

Zhao, J.-H., Bower, G. C., & Goss, W. M. 2001, ApJ, 547, L29

Zylka, R. et al. 1995, A&A, 297, 83

Chapter 2

Emission and Outflows from Black Hole Accretion Disks

2.1 Introduction

One of the most attractive areas of astrophysics lies at the intersection of astronomy and gravitational physics, in the rapidly growing observational and theoretical study of black holes in their natural setting. Candidate black holes are found in binary systems, with mass $M \sim 10\,\mathrm{M}_\odot$, and in the nuclei of galaxies, with $M \sim 10^6$ to $10^{10}\,\mathrm{M}_\odot$. Intermediate-mass candidates exist but are much less secure. Observational facilities that operate across the electromagnetic spectrum are gathering a wealth of new data about black hole candidates, primarily by observing radiation from a hot, luminous plasma deep in the object's gravitational potential [Ferrarese & Ford, 2005, Remillard & McClintock, 2006]. In some cases this plasma is streaming outward and will be observed as a collimated *jet* at large radius; in other cases the plasma is believed to be moving inward, forming an *accretion disk*.[1] Both the origin of the jet and the structure of the disk are poorly understood, and new developments in the theory of both are the subject of this paper.[2]

The massive dark object in the center of our galaxy, which coincides with the radio source Sgr A*, is one of the most interesting black hole candidates; from here on we will dispense with the word *candidate* for Sgr A* as the evidence for a black hole there is so strong as to make alternative models highly contrived; see, e.g. Broderick & Narayan [2006]. At a distance of $R \simeq 8$kpc [Beloborodov et al., 2006, Eisenhauer et al., 2005, Ghez et al., 2005], this $M \simeq 4 \times 10^6\,\mathrm{M}_\odot$ black hole has a larger angular size than all candidate black holes, and therefore offers the best opportunity for directly imaging the silhouette (or "shadow" [Falcke, Melia, & Agol, 2000]) of an event horizon. However, its remarkably small bolometric luminosity of $L \approx 10^3 L_\odot \approx 10^{-8} L_{\rm edd}$—where $L_{\rm edd}$ is the Eddington luminosity—provides a challenge for theoretical models.

[1] We use the term disk to mean any accretion flow with angular momentum. In some cases a ring-like structure is directly observed (NGC 4258).

[2] This work was published in Classical and Quantum Gravity [Noble et al., 2007]. Reproduction for this dissertation is authorized by the copyright holder IOPP.

If one assumes that the accretion rate $\dot{M}_{\rm X-rays} \simeq 4 \times 10^{-5}\,{\rm M}_\odot{\rm yr}^{-1}$ at $r \approx 0.1{\rm pc} \approx 5.6 \times 10^5 GMc^{-2}$, based on a Bondi model and X-ray observations [Baganoff et al., 2001, 2003], holds for all r and that accretion flow is a thin disk near the black hole, then the observed luminosity is approximately

$$L \approx 10^{-5} \left(\frac{0.1}{\eta}\right) L_{\rm thin} = 10^{-5} \left(\frac{0.1}{\eta}\right) c^2 \dot{M}_{\rm X-rays} \quad , \tag{2.1}$$

(η is the radiative efficiency) so either $\dot{M}$ varies with r, the thin disk model is irrelevant, or both. The spectral energy distribution (SED) shows no sign of the multitemperature black body distribution expected from a thin disk [e.g. Narayan, 2002]. Recent millimeter and sub-millimeter polarimetry observations, folded through a model of the accretion flow, require $\dot{M} \lesssim 10^{-7} - 10^{-9}\,{\rm M}_\odot{\rm yr}^{-1}$ [Macquart et al., 2006, Marrone et al., 2006b] near the hole. All this suggests that $\dot{M}$ drastically diminishes as $r \to 0$.

Current popular theories of Sgr A* fall into two categories: jet models and radiatively inefficient accretion flow (RIAF) models. The former suppose that the most luminous part of Sgr A* is a pair of relativistic jets of plasma propagating perpendicular to the accretion flow that emit via synchrotron and/or synchrotron self-Compton processes [Falcke et al., 1996, Falcke & Markoff, 2000]. The RIAF theories suggest that the disk is quasi-spherical but rotating, and emits via synchrotron, bremsstrahlung and Compton processes [Yuan, Quataert & Narayan, 2003]. In order to account for the low luminosity, the RIAF disk is taken to be an inefficient emitter that retains much of its heat and maintains a geometrically thick profile. Each of these models are freely specified by a number of unknown parameters such as the radius of the jet's sonic point or the fraction of heat shared between electrons and protons in the RIAF disk. With this considerable freedom, each model can predict the spectrum quite well.

These two theories neglect GR effects and do not account for dynamical variations of the spectrum self-consistently. General relativistic calculations of the emission have been performed, though they have used RIAF solutions [Broderick & Loeb, 2006a] or simple orbiting spheres of hot plasma [Broderick & Loeb, 2005, 2006b] as sources. They also use an isotropic (angle-averaged) synchrotron emissivity. A radiative transfer calculation based on Newtonian magnetohydrodynamic (MHD) simulation data has been performed using the Paczynski-Witta potential to approximate the black hole's effect [Goldston, Quataert & Igumenshchev, 2005], but this cannot fully account for light-bending, gravitational redshift, and Doppler effects, particularly if the

black hole is rapidly rotating.

Here we will present the first self-consistent optically thin calculations of Sgr A*'s image and spectrum at about $\lambda = 1$mm, near the peak of its SED. This band of radiation is particularly interesting since it originates near the horizon and will, consequently, be strongly affected by the hole's curvature. Improvements in millimeter and sub-millimeter Very Long Baseline Interferometry (VLBI) will soon permit features at the scale of the horizon to be resolved [Doeleman & Bower, 2005]; this makes the construction of accurate, detailed models that incorporate relativistic effects even more pressing.

Another active subject relevant to accretion disks is the study of relativistic jets. Whether they are black hole of a few solar masses [Fender & Belloni, 2004, Mirabel & Rodríguez, 1999] or are extragalactic and supermassive [Ferrari, 1998, Harris & Krawczynski, 2006], jets are observed emanating from them. Following the recent surge of interest in general relativistic magnetohydrodynamic (GRMHD) simulations, several groups have begun to investigate the outflows that appear spontaneously in weakly radiative accretion disk simulations [De Villiers, Staff & Ouyed, 2005, Hawley & Krolik, 2006, McKinney, 2006]. We contribute to this body of work by presenting recent evolutions of jets launched from geometrically thick disks. We describe the large-r scaling of the jet and explain its dependence on numerical parameters.

The outline of the paper is the following. We describe the theory and methodology used for our GRMHD disk simulations in Section 2.2.1. These simulations serve as the dynamic radiative source for our radiative transfer calculations, which are described in Section 2.2.2. Images and spectra of Sgr A* for a variety of situations are presented in Section 2.3. Section 2.4 describes our work on jets, and Section 2.5 gives a summary.

2.2 Theoretical Foundation

In many accreting black hole systems, the inner part of the material flow is well explained by the ideal MHD approximation. We employ this assumption in our dynamical evolutions of black hole accretion disks as described in the Section 2.2.1. Emission from these simulations is calculated via a ray-tracing technique described in Section 2.2.2.

2.2.1 General Relativistic Magnetohydrodynamics

We present in this section an outline of the equations and methodology used to calculate accretion disk evolutions. More thorough descriptions can be found in Gammie, McKinney, & Tóth [2003], Noble et al. [2006], yet we repeat a few points here to provide a context for the rest of the paper.

Throughout this paper we follow standard notation [Misner, Thorne & Wheeler, 1970]. We work in a coordinate basis with metric components $g_{\mu\nu}$ and independent variables t, x^1, x^2, x^3. The quantity $n_\mu = (-\alpha, 0, 0, 0)$ is the dual of the 4-velocity of a "normal observer" that moves orthogonal to constant t foliations of spacetime, where $\alpha^2 = -1/g^{tt}$ is the square of the lapse. Greek indices refer to all spacetime components, while Roman indices represent only spatial components. Geometrized units are used so $G = c = 1$ unless otherwise noted.

The GRMHD equations of motion include the continuity equation,

$$\nabla_\mu \left(\rho_\circ u^\mu\right) = 0 \quad , \tag{2.2}$$

the equations of local energy conservation

$$\nabla_\mu T^\mu{}_\nu = 0 \quad , \tag{2.3}$$

and Maxwell's equations

$$\nabla_\nu {}^*F^{\mu\nu} = 0 \quad . \tag{2.4}$$

Here, $\rho_\circ$ is the rest-mass density, u^μ is the fluid's 4-velocity, $T^\mu{}_\nu$ is the MHD stress-energy tensor, and the Maxwell tensor ${}^*F^{\mu\nu}$ is the dual of the electromagnetic field tensor $F^{\mu\nu}$. The ideal MHD approximation,

$$u_\mu F^{\mu\nu} = 0 \tag{2.5}$$

eliminates three of the six degrees of freedom inherent in the electromagnetic field. The remaining degrees of freedom can be represented by the three non-trivial components of the magnetic field in the frame of the normal observer:

$$\mathcal{B}^\mu \equiv -n_\nu {}^*F^{\mu\nu} \quad . \tag{2.6}$$

A convenient tensor related to $\mathcal{B}^\mu$ is one proportional to the projection of the field

into a space normal to the fluid's frame:

$$b^{\mu} \equiv \frac{1}{\gamma} \left(\delta^{\mu}{}_{\nu} + u^{\mu} u_{\nu} \right) \mathcal{B}^{\nu} \quad . \tag{2.7}$$

Using these definitions, one can easily show that the MHD stress-energy tensor can be expressed as

$$T^{\mu\nu} = \left(\rho_{\circ} + u + p + b^2 \right) u^{\mu} u^{\nu} + \left(p + \frac{b^2}{2} \right) g^{\mu\nu} - b^{\mu} b^{\nu} \quad , \tag{2.8}$$

where p is the fluid's pressure, u is the fluid's internal energy density, and $b^2 \equiv b_{\mu} b^{\mu}$. Further, one can show that the GRMHD equations of motion can take the following flux conservative form

$$\partial_t \mathbf{U}(\mathbf{P}) = -\partial_i \mathbf{F}^i(\mathbf{P}) + \mathbf{S}(\mathbf{P}) \quad , \tag{2.9}$$

where $\mathbf{U}$ is a vector of "conserved" variables, $\mathbf{F}^i$ are the fluxes, and $\mathbf{S}$ is a vector of source terms. Explicitly, these are

$$\mathbf{U} = \sqrt{-g} \left[\rho_{\circ} u^t, T^t{}_t + \rho_{\circ} u^t, T^t{}_j, \mathcal{B}^k / \alpha \right]^T \tag{2.10}$$

$$\mathbf{F}^i = \sqrt{-g} \left[\rho_{\circ} u^i, T^i{}_t + \rho_{\circ} u^i, T^i{}_j, \left(b^i u^k - b^k u^i \right) \right]^T \tag{2.11}$$

$$\mathbf{S} = \sqrt{-g} \left[0, T^{\kappa}{}_{\lambda} \Gamma^{\lambda}{}_{t\kappa}, T^{\kappa}{}_{\lambda} \Gamma^{\lambda}{}_{j\kappa}, 0 \right]^T \quad , \tag{2.12}$$

where $\Gamma^{\lambda}{}_{\mu\kappa}$ is the metric's associated affine connection coefficients. Note that Maxwell's equations are rewritten as the last three components of (2.9)—also known as the induction equations—and a constraint equation

$$\partial_i \left(\sqrt{-g} \mathcal{B}^i / \alpha \right) = 0, \tag{2.13}$$

which must be upheld during the evolution. Since the equations are solved in flux conservative form, energy is conserved to machine precision. This means that small-scale structures in the velocity and magnetic field are erased by numerical smoothing, but that the associated kinetic and electromagnetic energy is captured as entropy.

We use the HARM code [Gammie, McKinney, & Tóth, 2003] to evolve axisymmetric disks on a fixed background. Because of axisymmetry our numerical models will fail to capture some aspects of the disk dynamics. For example, axisymmetric MHD flows cannot sustain turbulence due to the anti-dynamo theorem and fail to properly capture the dynamics of magnetic Rayleigh-Taylor instabilities. 3D models

will eventually be required to include these effects.

A central, Lax-Friedrich-like flux method similar to that proposed by Kurganov and Tadmor Kurganov & Tadmor [2000] is used. The Flux-CT method [Tóth, 2000] is used to impose the "no-monopoles" constraint, and the monotonized central limiter scheme is used to reconstruct at each cell interface. In order to calculate $\mathbf{F}^i$ we need to invert the conserved variable definitions for the primitive variables. This is performed using the "2D" method of Noble et al. [2006]. In all of the results shown here, the equation of state

$$p = (\Gamma - 1)\, u \tag{2.14}$$

is used with $\Gamma = 4/3$. Also, we use a grid that is uniformly spaced in a slightly modified version of the usual spherical Kerr-Schild coordinates t, r, θ, ϕ, which are regular on the horizon. The modifications concentrate numerical resolution toward the event horizon and toward the midplane of the disk.

Our initial data consists of a torus in hydrodynamic equilibrium [Fishbone & Moncrief, 1976][3] On top of this Fishbone-Moncrief torus we add a weak magnetic field with vector potential $A_\phi = \mathrm{Max}\,(\rho_\circ/\rho_{\max} - 0.2, 0)$ where $\rho_{\max}$ is the maximum of the disk's rest-mass density. The magnetic field amplitude is normalized so that the ratio of gas to magnetic pressure within the disk has a minimum of 100. With the addition of the field the disk is no longer strictly in equilibrium, but because the field is weak it is only weakly perturbed. The initial state is unstable to the MRI [Balbus & Hawley, 1991], so turbulence develops in the disk and material accretes onto the black hole. Since HARM is incapable of evolving a vacuum, we surround the disk in an artificial atmosphere, or "floor" state, with $\rho_{\circ,\mathrm{atm}} = 10^{-4}(r/M)^{-3/2}$ and $u_{\mathrm{atm}} = 10^{-6}(r/M)^{-5/2}$. Whenever $\rho_\circ$ and u fall below the floor they are artificially set to the floor.

2.2.2 General Relativistic Radiative Transfer

We consider non-polarized, optically thin emission from a thermal distribution of electrons at wavelengths near the sub-millimeter peak in Sgr A*'s spectrum. At these wavelengths, the disk is expected to be optically thin and thermal synchrotron emission is expected to dominate. We include both synchrotron and bremsstrahlung, confirming that the former dominates. Even though much of the disk is calculated to be optically thin for frequencies of interest here, there are small regions where

[3]The Fishbone-Moncrief solution has a single key parameter $u_\phi u^t$, which is by assumption constant. In units where $GM = c = 1$, our solution is such that $u_\phi u^t = 4.28$.

absorption is important. For this reason, our calculations include absorption and the radiative transfer equation is solved.

Numerical methods for calculating emission in curved spacetimes have become more refined and sophisticated since their introduction decades ago. One of the first calculations including light bending, lensing, gravitational redshifts and Doppler redshifts in general relativity was done by Cunningham [1975] through the use of the so-called "transfer function," which maps the specific intensity of a luminous source to what would be observed at infinity[4]. Polarization transfer functions were implemented in a Monte Carlo algorithm by Connors, Stark & Piran [1980], who modeled polarized X-ray emission from geometrically thick clouds around Kerr black holes. This method was later developed by Laor, Netzer & Piran [1990] to study the effects of self-illumination on the emission from accretion disks [Cunningham, 1976]. An algebraic expression for the polarization transfer function in the Schwarzschild spacetime was derived by Chen & Eardley [1991] to study the polarization of line emission from thin disks. Time-dependent emission from accretion disk hot spots was calculated using a code by Karas, Vokrouhlicky & Polnarev [1992] that "compressed" and stored geodesic curves as Chebyshev polynomials so that many transfer calculations could be done without repeating the laborious geodesic integrations. An efficient and somewhat complicated semi-analytical way of integrating the geodesic equations in Kerr spacetimes was developed by Rauch & Blandford [1994]. The variability from indirect photons (i.e. those that follow highly curved geodesics) on Sgr A* IR emission was estimated by Hollywood & Melia [1997]. Modern techniques for efficiently calculating optically thin line emission from general sources and spacetimes have been developed by a number of groups [e.g. Bromley, Chen & Miller, 1997, Beckwith & Done, 2005, Dovčiak, Karas & Yaqoob, 2004]. The theory of polarized radiation propagation and transfer through a magnetized plasma was derived and implemented in Broderick & Blandford [2003, 2004]. This work and another [Fuerst & Wu, 2004] solves the radiative transfer equations with absorption in covariant form. More recently, a radiative transfer code that uses data from GRMHD disk simulations has been used to investigate the presence of quasi-periodic oscillations in calculated thermal radiation [Schnittman, Krolik & Hawley, 2006].

In our work, radiation is modeled as discrete bundles of photons that follow null geodesics from the disk to a "camera" 8kpc from Sgr A*. The geodesic equation is

[4]An implementation of the algorithm described in Cunningham [1975] was written and made publicly available by Speith, Riffert & Ruder [1995].

solved in first-order form:

$$\frac{\partial x^\mu}{\partial \lambda} = N^\mu \quad , \quad \frac{\partial N_\mu}{\partial \lambda} = \Gamma^\nu{}_{\mu\eta} N_\nu N^\eta \quad , \tag{2.15}$$

where $\Gamma^\nu{}_{\mu\eta}$ are the connection coefficients, and $N^a = \left(\frac{\partial}{\partial \lambda}\right)^a$ is the tangent vector along the geodesic that is parametrized by the affine parameter λ. As usual [Broderick & Loeb, 2006b, Bromley, Chen & Miller, 1997, Dovčiak, Karas & Yaqoob, 2004, Schnittman & Bertschinger, 2004], the geodesics are calculated in reverse from a camera pixel back through the simulation volume. We assume that the camera is a static observer in our coordinates and is centered on the black hole. From the far ends of the geodesic, the radiative transfer equations are integrated forward to obtain the final specific intensity values. The initial intensities are set to zero since the bundles either start at the event horizon or originate from past null infinity.

The equations of general relativistic radiative transfer naturally develop from a generalization of Liouville's theorem to non-inertial frames [Lindquist, 1966] (see also Misner, Thorne & Wheeler [1970] and Mihalas & Weibel-Mihalas [1999]), which states that the number of photons, $d\mathcal{N}$, per phase space volume, $d\mathcal{V}$, is invariant along the photon trajectory in vacuum:

$$\frac{d}{d\lambda}\frac{d\mathcal{N}}{d\mathcal{V}} \equiv \frac{df}{d\lambda} = 0 \quad ; \tag{2.16}$$

here λ is the affine parameter of the geodesic that the bundle follows and f is the photon distribution function. It is more common to describe the radiation field by the specific intensity $I_\nu \propto \nu^3 f$ at frequency ν, or with the invariant intensity $\mathcal{I} = I_\nu/\nu^3$.

When ionized matter is present, photons can be scattered in and out of the bundle, converted to material degrees of freedom (absorbed) or can be added to the bundle via spontaneous or induced emission. In the optically thin limit, scattering events are rare and can be ignored. Since the rate of absorption is proportional to the bundle's intensity and the rate of emission is not, the frame-independent radiative transfer equation takes the simple source/sink form:

$$\frac{d\mathcal{I}}{d\lambda} = \mathcal{J} - \mathcal{A}\mathcal{I} \quad , \tag{2.17}$$

where $\mathcal{J}$ and $\mathcal{A}$ are the Lorentz invariant emissivity and absorption coefficient, respectively, which are related to their frame-dependent counterparts j_ν and α_ν by

$$\mathcal{J} = \frac{j_\nu}{\nu^2} \quad , \quad \mathcal{A} = \nu\alpha_\nu \quad . \tag{2.18}$$

The dimensions of λ can be deduced by reducing equation (2.17) to the usual inertial-frame version:

$$\frac{dI_\nu}{ds} = j_\nu - \alpha_\nu I_\nu \quad , \tag{2.19}$$

where $ds = cdt_\nu$ is the path length the photon traverses over time interval dt_ν as measured in a frame in which the photon's frequency is ν. For these to be equivalent we must define λ so that the tangent vector appearing in the geodesic equation is

$$N^\mu = \frac{c}{2\pi} k^\mu \quad , \tag{2.20}$$

and k^μ is the photon wavevector.

In practice, using λ as an integration variable leads to loss of precision near the horizon. We instead use $d\lambda' = d\lambda/n(r)$ where

$$n(r) = \frac{r}{r_h} - 1 \quad , \tag{2.21}$$

and r_h is the radius of the event horizon.

A single time slice of the disk evolution is used to calculate j_ν and α_ν. This crude approximation will be accurate where the matter distribution varies slowly compared to a light crossing time, as it is in the bulk of the disk. It will also be accurate for observations over timescales longer than the light-crossing time; this applies to VLBI observations of Sgr A*. The primitive variables, $\{\rho, u, \tilde{u}^i, \mathcal{B}^i\}$, from the time slice are bilinearly-interpolated at each point along the geodesic and stored; $\tilde{u}^i \equiv (\delta^i{}_\mu + n^i n_\mu)\, u^\mu$ is the spacelike velocity perpendicular to n^μ. The step size is a tunable fraction of the local grid spacing so that the simulation data is well sampled.

The interpolated data is then used to integrate equation (2.17) using one or several emission models. The Lorentz invariant emissivity $\mathcal{J}$ is calculated from the local observer's value of j_ν. We assume a thermal distribution function for the electrons so that $\alpha_\nu = j_\nu / B_\nu$ where B_ν is Planck's distribution. We use an anisotropic, angle-dependent approximation to j_ν taken from Wardziński & Zdziarski [2000]. We have confirmed that this expression yields results to an accuracy no worse than any of our other assumptions or approximations [Leung, Noble & Gammie, 2007].

2.3 Sgr A* Emission

Observations indicate that most of Sgr A*'s radiation originates as optically thin emission near the event horizon at a wavelength of $\lesssim$ 1mm [e.g. Marrone et al.,

2006b]. Even if the accreting plasma has very little angular momentum, it is expected to have circularized in this region. If the magnetic field is weak at large radii, it is expected to be amplified to near equipartition with the disk's internal energy via the magnetorotational instability (MRI) [Balbus & Hawley, 1991]. This makes previous accretion disk simulations [McKinney & Gammie, 2004] suitable for our study since they yield statistically steady flows within $r \lesssim 12M$.

The electrons are assumed to follow a thermal distribution which is consistent with modern models that find a power-law distribution of electrons is needed to simultaneously match radio and X-ray observations, but that thermal electrons are the dominant emitters at sub-millimeter/millimeter wavelengths [Yuan, Markoff & Falcke, 2002, Yuan, Quataert & Narayan, 2003]. Further, we assume that the electrons and ions are at the same temperature, although some successful models of Sgr A*'s spectrum and variability assume a two-temperature flow [Goldston, Quataert & Igumenshchev, 2005, Yuan, Quataert & Narayan, 2003]. Cooling times for synchrotron and bremsstrahlung emission are long compared with the inflow time in our model, as expected for the matter near Sgr A*. Numerically integrated optical depths indicate that that the disk is everywhere optically thin (i.e. optical depth is less than unity) when $\lambda \lesssim 1$mm. We can therefore neglect the radiation's effect on the the GRMHD simulations for these wavelengths.

Table 2.1 Parameters for the accretion disk evolutions used to model Sgr A* emission. All quantities are given in geometrized units unless explicitly stated otherwise. The radii r_1, r_2 and $r_{\rm ISCO}$ are—respectively—the radius of the inner edge of the equilibrium torus at $t = 0$, radius of the pressure maximum at $t = 0$, and the radius of the ISCO for the given spacetime. $\dot{M}_{\rm 4Jy}$ is the accretion rate resulting in a flux density of 4Jy at Earth; this is used to set the scale of the rest-mass density. The quantities $\langle \dot{M} \rangle$, $\langle \dot{E} \rangle$, $\langle \dot{L} \rangle$ are—respectively—the average accretion rates of the rest-mass, energy, and angular momentum, taken over $1100M < t < 1500M$.

a_* (M)	r_1 (M)	r_2 (M)	$r_{\rm ISCO}$ (M)	$\dot{M}_{\rm 4Jy}$ ($10^{-9}\,{\rm M}_\odot{\rm yr}^{-1}$)	$\langle \dot{M} \rangle$	$\langle \dot{E} \rangle / \langle \dot{M} \rangle$	$\langle \dot{L} \rangle / \langle \dot{M} \rangle$
0.0	6.4	15.05	6.00	7.34	0.88	0.95	3.01
0.5	6.0	13.02	4.23	3.60	0.75	0.94	2.58
0.75	6.0	12.35	3.16	2.05	0.41	0.90	2.15
0.88	6.0	12.10	2.48	1.15	0.30	0.89	1.96
0.94	6.0	12.00	2.04	0.82	0.23	0.86	1.62
0.97	6.0	12.00	1.75	1.23	0.33	0.86	1.65

The degrees of freedom of our model include the spin of the black hole (a_*),

the accretion rate ($\dot{M}_{\rm scale}$), the inclination (angle $i_{\rm inc}$ between the black hole angular momentum vector and the line of sight to the black hole), and the time at which we make the image ($t_{\rm pic}$). The spin and inclination are unknown for Sgr A*, though a recent periodicity in X-ray flux that has been seen may be evidence of $a_* \gtrsim 0.22$ [Belanger et al., 2006]. Disk simulations with different a_* and initial disk distributions are used and are tabulated in Table 2.1. Each simulation used 256×256 cells with the algorithm described in Section 2.2.1. This resolution proves to be sufficient for our purposes since higher resolution simulation data (using 512×512 and 1024×1024 cells) produced differences easily accounted for by time variability. We set r_1 and r_2—the radii of the inner torus edge and the pressure maximum—so that all tori have similar shapes and sizes initially. The density is scaled until the flux density at 1mm matches an observationally determined 4Jy [Marrone et al., 2006a]; this yields an accretion rate we will call $\dot{M}_{\rm 4Jy}$. Finally, we find insignificant dependence on the simulation's floor model in our emission calculations since its flux is always many orders of magnitude smaller than that of the rest of the flow.

It is interesting to note that $\dot{M}_{\rm 4Jy}$ are always consistent with the observational limits $\dot{M} \lesssim 10^{-7}$–$10^{-9}\,{\rm M}_\odot{\rm yr}^{-1}$ [Macquart et al., 2006, Marrone et al., 2006b] obtained by folding measurements of the rotation measure through a model for Faraday rotation within the accretion source. Because they use a RIAF-like model the agreement with the simulations may in part be coincidental; it would be very interesting to see self-consistent calculations of the rotation measure from the numerical simulations.

An outstanding concern for future millimeter/sub-mmVLBI experiments is whether there will be any observable effect from the black hole's curvature. For this purpose, we present images of a single snapshot ($t_{\rm pic} = 1250M$) of a simulation ($a_* = 0.94$) at $\lambda = 1$mm for different inclination angles in Figure 2.1. The raw images, in which each pixel represents a unique ray, are shown next to their convolved counterparts. The convolution is performed using a circular Gaussian beam to simulate the appearance of an image taken with VLBI using a baseline 8000km at $\lambda = 1$mm [Doeleman & Bower, 2005, Falcke, Melia, & Agol, 2000]. As expected, we find that the brightest regions of the disk lie in the inner equatorial region of the flow where u and b^2 are largest. The part of the disk approaching the camera is brightest because of relativistic beaming. The brightest region is especially interesting since most, if not all, of the geodesics that pass through it originate near the horizon and orbit the black hole multiple times before reaching the camera. Please note that the asymmetry seen in the $i_{\rm inc} = 5^\circ$ images is expected since the disk is slightly inclined to the viewer. Even though it is much more noticeable in the convolved image, the asymmetry is

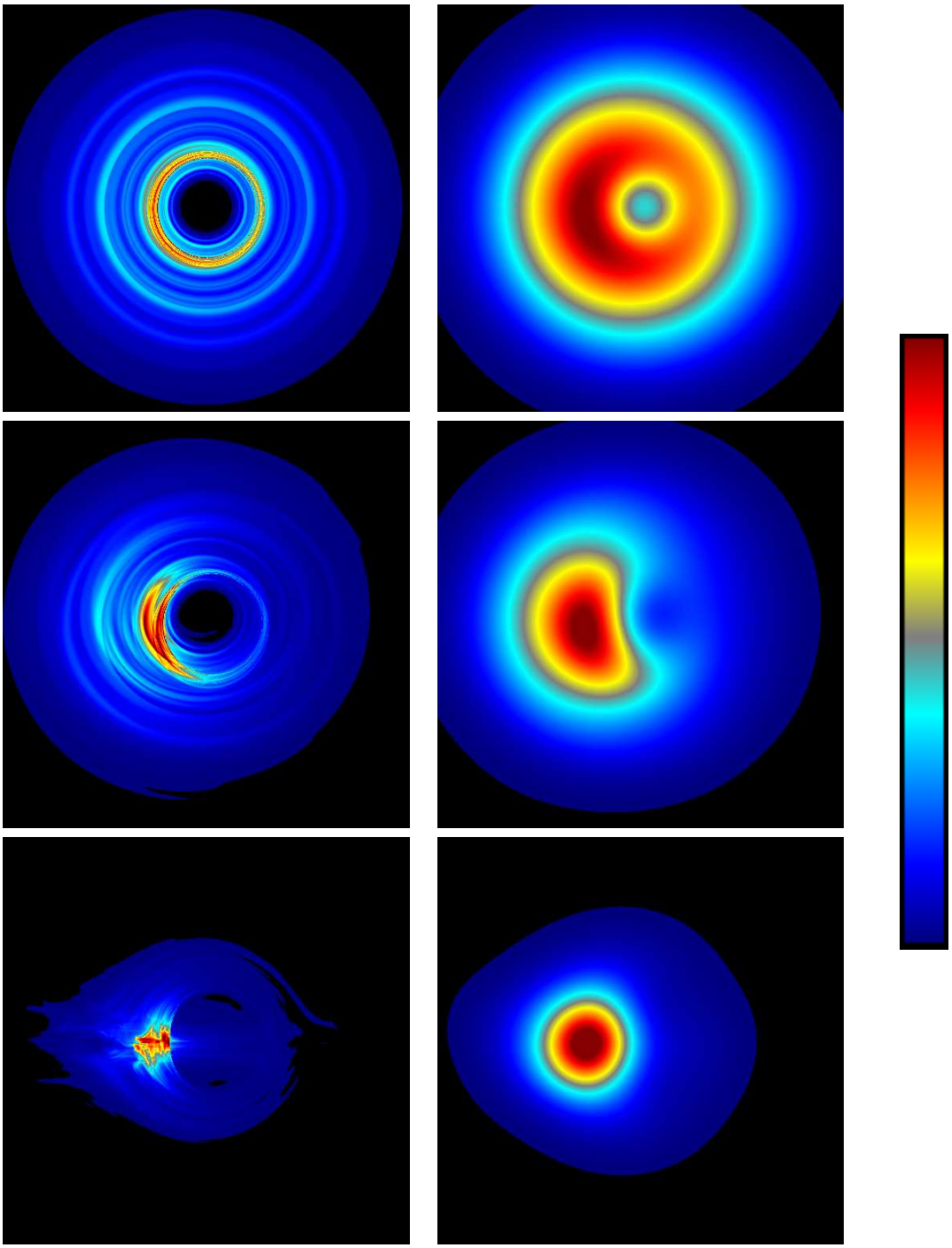

Figure 2.1 Images of the accretion disk viewed at a wavelength of 1mm seen at inclination angles of 5° (top), 30° (middle) and 90° (bottom). Each frame shows a view $40M$ wide in the plane of the singularity. Frames in the left column are "infinite" resolution images, while those in the right column have been convolved with a symmetric Gaussian beam to simulate a 8000km baseline VLBI observation. The linear colour map used is shown at the right of the images. Each image has been scaled by its maximum intensity for illustrative purposes.

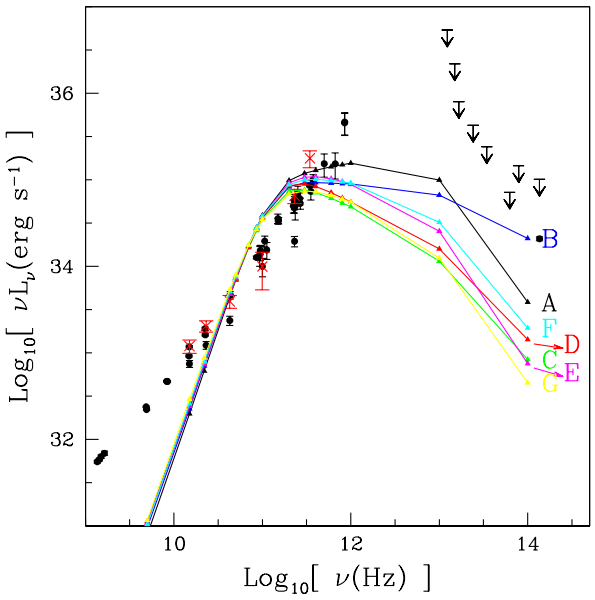

Figure 2.2 Spectra taken at $i_{\rm inc} = 30°$ using snapshots of the $a_* = 0.94$ disk at different points along its evolution. Lines A-G respectively represent $t_{\rm pic} = 1150M, 1250M, 1326M, 1434M, 1500M, 1560M, 1666M$.

also present in the high resolution image.

The black hole silhouette is obvious in the raw images at all inclinations, though may only be observable in practice if $i_{\rm inc} \lesssim 30°$. This does not necessarily mean that other observables—such as variability and polarization fraction—are not sensitive to relativistic effects at other inclinations.

We have also calculated spectra for a survey over $t_{\rm pic}$, a_*, and $i_{\rm inc}$, shown in Figures 2.2 - 2.4. A standard model was used for comparison: $t_{\rm pic} = 1250M$, $a_* = 0.94$, $i_{\rm inc} = 30°$. The filled circles with error bars in these plots represent observed flux values of Sgr A* during quiescence [Falcke et al., 1998, Hornstein et al., 2002, Macquart et al., 2006, Marrone et al., 2006a, Serabyn et al., 1997, Zhao et al., 2003]. The red exes are found from flux measurements during flare events [Zhao et al., 2003], and the arrows indicate upper limits at NIR/IR wavelengths [Serabyn et al., 1997]. Error bars indicate the measured errors quoted in the references. We calculate L_ν assuming isotropic emission.

Our calculations are most relevant in the vicinity of $\nu \simeq 3 \times 10^{11}$Hz. At lower frequencies the emission likely arises from plasma outside the computational domain, and so we cannot model it. The absence of this material may explain why the calculated luminosities are too large at $\nu \approx 10^{11}$Hz. For $\nu \gtrsim 10^{13}$Hz, both Compton scattering and direct synchrotron emission from a power-law distribution of electrons

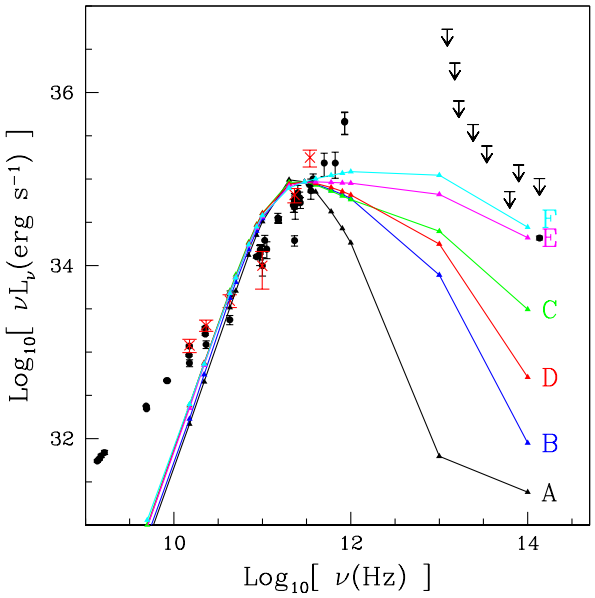

Figure 2.3 Spectra taken at $i_{\rm inc} = 30°$ and $t_{\rm pic} = 1250M$, but using simulation data from evolutions with different black hole spins. Lines A-F respectively represent $a_* = 0, 0.5, 0.75, 0.88, 0.94, 0.97$.

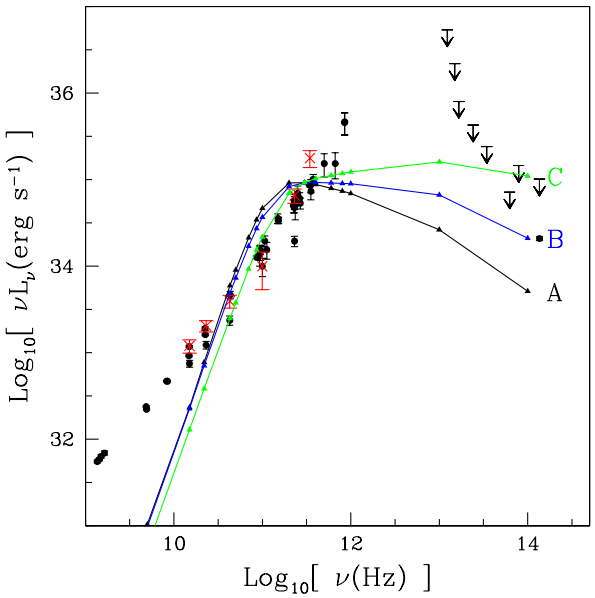

Figure 2.4 Spectra taken at $t_{\rm pic} = 1250M$ using $a_* = 0.94$ simulation data at different $i_{\rm inc}$. Lines A-C respectively represent $i_{\rm inc} = 5°, 30°, 90°$.

may be important; these effects are not modeled here.

Temporal variations in the spectrum are small at $\nu \simeq 10^{11}$Hz. Near the peak, the variation is comparable to current observational sensitivities and may be able to account for some flares. The complexity of the radiative transfer calculation is evident in the nonuniformity of the time variability with frequency.

The sensitivity of the spectrum to the time slice used to calculate the spectrum is dwarfed by the sensitivity of the spectrum to the choice of black hole spin a_*. We find a fairly uniform trend of increasing bolometric luminosity with spin (while holding the 1mm flux at 4Jy); the $a_* = 0.75$ and $a_* = 0.88$ cases break this trend, but this may just be the result of a temporary fluctuation. The variation of the spectrum with a_* may be attributable to an increase in relativistic beaming with spin, and an increase in temperature and magnetic field strength near the horizon with spin. The latter is not as strong an effect as the former since $\dot{M}_{4\mathrm{Jy}}$ at $a_* = 0$ is about 7 times the value at $a_* = 0.97$.

The SED dependence on i_{inc} is the most telling in that NIR/IR upper limits likely rule out edge-on disks with large a_*. Assuming the same trend in i_{inc} at comparable values of a_*, the NIR/IR upper limits constrain our models to have $i_{\mathrm{inc}} \lesssim 30^\circ$ for $a_* \gtrsim 0.88$ and any inclination for smaller spins. Coincidentally, $i_{\mathrm{inc}} \lesssim 30^\circ$ is also the range in inclination angle that provides the best chance at observing the black hole's silhouette at $\lambda = 1$mm. Recently, the variability seen in flux and polarization angle at NIR wavelengths has been shown to be consistent with emission from an orbiting hot spot and ring inclined at $\gtrsim 35^\circ$ [Meyer et al., 2006]. Our results with their constraint on inclination angle then suggest that $a_* \lesssim 0.88$. Future fits from numerical models will more strongly constrain the inclination and spin.

2.4 Accretion Disk Jets

Jets are almost always seen in our accretion disk simulations. They produce very little emission in the Sgr A* models considered earlier because they are nearly empty of mass at small radii. As they mix with the surrounding material present at larger radii, the jets may become more luminous. Since they play no significant role in our calculation of Sgr A*'s emission, they are considered separately in this section.

Our simulations of jets launched from accretion flows extend to distances of $r \sim 10^3 M$. They are not dependent on the inner radial boundary condition since it is causally disconnected from the rest of the numerical domain (i.e. it lies within the event horizon), and we terminate their evolution before any matter reaches the outer

boundary. These outflows are generated spontaneously by a combination of forces very close to the black hole. They are interesting because they are easily observable, and their large observed Lorentz factors were used as one of the first arguments for relativistically strong gravitational fields in the engine that drives them.

Early attempts at studying jets with HARM were plagued by instabilities that we have since cured by using a new set of coordinates that improve the resolution along the symmetry axis. Specifically, we use

$$r = e^{x^1} \quad , \quad \theta = \pi x^2 + \frac{2h_2}{\pi} \sin(2\pi x^2) \arctan\left[s\left(x_0^1 - x^1\right)\right], \tag{2.22}$$

which are different from the modified Kerr-Schild coordinates described in Gammie, McKinney, & Tóth [2003]. Here x_0^1 is a transition radius where the grid begins to focus toward the axis, the parameter s controls how quickly this transition is made, and h_2 controls the strength of the focusing. We set $x_0^1 = \log(40)$, $s = 2$, and $h_2 = 0.35$ so that the cells become more focused along the axis at a radius beyond the bulk of the disk.

Using these coordinates we performed a run using 568×256 cells (more cells are needed to extend the grid radially). The same initial conditions were used as in the $a_* = 0.94$ run of Table 2.1. We present here data from $t = 1500M$, which is near the end of the period of time-steady accretion. At this point the jet has reached $r \simeq 800M$. Figure 2.5 shows snapshots of the Lorentz factor ($\gamma \equiv \alpha u^t$), rest-mass density ($\rho_\circ$), magnetic field density (b^2) and the toroidal component of the electromagnetic potential (A_ϕ). Notice that poloidal magnetic field lines follow isosurfaces of A_ϕ. The jet is magnetically-dominated and remains well collimated for at least the first $10^3 M$. The jet seems to be driven by Poynting flux near the poles, and—further away from the axis—by a relativistic wind driven both thermally and centrifugally.

The jet is relativistic, occasionally reaching $\gamma \sim 10$. But the maximum γ reached is sensitive to the magnitude and profile of the floor. To quantify this dependence, we performed three runs with 256×128 cells using the floor profiles: $\rho_{\circ\min} \in \{0.2, 1, 5\}\, 10^{-4}\, r^{-3/2}$, $u_{\min} \in \{0.2, 1, 5\}\, 10^{-6}\, r^{-5/2}$. The maximum values of γ averaged over $0 < \theta < 15^\circ$ at $t = 1500M$ are 6, 2.5, and 2—respectively—for these floors. Differences in the density and pressure profiles are also present since the floor is reached throughout the polar regions in all these instances. The lowest floor in this set is close to the stability limit for HARM. By using a higher-order reconstruction method, McKinney [2006] found that HARM can be extended to reliably evolve similar outflows with a

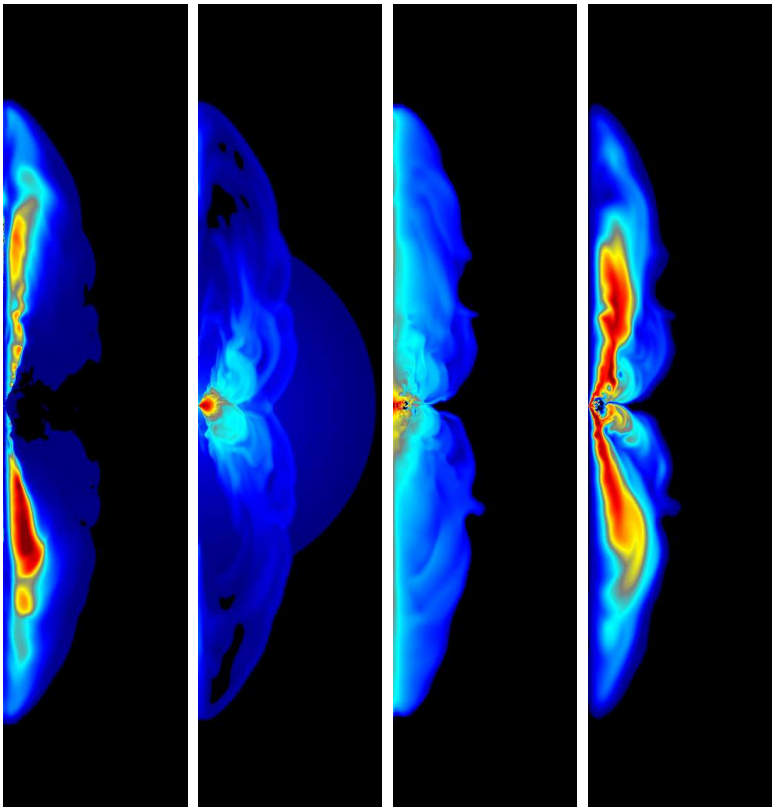

Figure 2.5 From left to right are snapshots of γ, $\rho_\circ$, b^2 and A_ϕ—whose isosurfaces follow poloidal magnetic field lines—at $t_{\rm pic} = 1500M$ for a run using 568×256 cells. The height of each image is $2000M$. White (red in the colour version) represents the maximum of the colour scale, and black (blue in the colour version) the minimum. Logarithmic colour scales are used for $\rho_\circ \in [10^{-8}, 1]$ and $b^2 \in [10^{-10}, 10^{-3}]$. Linear colour scales are used for $\gamma \in [1, 3.5]$ and $A_\phi \in [0, 0.08]$.

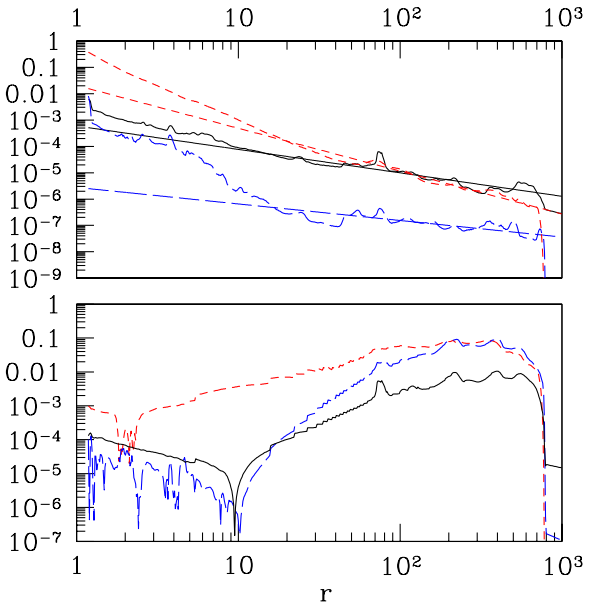

Figure 2.6 Profiles of $\rho_\circ$ (black solid line), p (blue long dashes) and $b^2/2$ (red short dashes) are shown in the top figure. The radial dependence of $\dot{m}$ (black solid line), η_M (blue long dashes), and η_{EM} (red short dashes) are shown in the bottom plot. All quantities are calculated at $t = 1500M$ using an opening angle of 15° from the axes.

floor which is sufficiently steep and that the floor is reached only near the base of the jet. Comparisons between these results and ours further indicate how the floor affects the jet; for example, our γ is almost a factor of 2 smaller.

The radial profiles of $\rho_\circ$, p and $b^2/2$ averaged over $\Delta\theta = 15°$ from both poles are shown in Figure 2.6. The thinner lines in the figure are power-law fits to the data at $r > 10M$. We find

$$\rho_\circ \sim r^{-0.9} \quad , \quad p \sim r^{-0.6} \quad , \quad b^2 \sim r^{-1.6} \quad . \tag{2.23}$$

The $\rho_\circ$ fit agrees with that seen by McKinney [2006] for $r < 120M$, but is much shallower than what they see for $r > 120M$. This is most likely attributable to the jet accumulating matter from our larger floor.

Also plotted are the jet luminosity and mass flux efficiencies. The matter and electromagnetic components of the jet's luminosity efficiency are

$$\eta_M = \frac{2\pi}{\epsilon\langle\dot{M}\rangle} \int_{d\theta_{\rm jet}} \left(-\hat{T}^r{}_t - \rho_\circ u^r\right) \sqrt{-g} d\theta \quad , \tag{2.24}$$

$$\eta_{EM} = \frac{2\pi}{\epsilon\langle\dot{M}\rangle} \int_{d\theta_{\rm jet}} -\tilde{T}^r{}_t \sqrt{-g} d\theta \quad , \tag{2.25}$$

where $d\theta_{\rm jet}$ represents the first 15° from both poles, $\hat{T}^r{}_t$ is the matter component of $T^r{}_t$, $\tilde{T}^r{}_t$ is the electromagnetic part of $T^r{}_t$, $\epsilon = 1 - \langle \dot{E} \rangle / \langle \dot{M} \rangle \simeq 0.13$ is an effective radiative efficiency, $\langle \dot{M} \rangle \simeq 0.30$ is the average mass accretion rate through the horizon over $1000M < t < 1500M$, and $\langle \dot{E} \rangle \simeq 0.26$ is the average energy accretion rate through the horizon over the same period. The mass flux efficiency is

$$\dot{m} = \frac{\dot{M}_{\rm jet}}{\langle \dot{M} \rangle} = \frac{2\pi}{\langle \dot{M} \rangle} \int_{d\theta_{\rm jet}} \rho_\circ u^r \sqrt{-g} d\theta \quad . \tag{2.26}$$

The electromagnetic luminosity component is significantly larger for $r \lesssim 100M$. The increase in the luminosity fraction with radius is partially due to collimation effects; the jet is wider than 15° at smaller radii and collimates further out. The similarity in the matter luminosity fraction and mass flux fraction is most likely from the jet's accumulation of mass from the floor. We, however, still see the conversion of electromagnetic flux into matter energy flux seen by others [McKinney, 2006]. Let us assume that the free energy in our jet at large r represents a reasonable estimate for the ultimate power of the jet. We can then estimate the jet to have a luminosity of

$$L_{\rm jet} \approx 0.013 \dot{M} c^2 \quad . \tag{2.27}$$

This value is similar to that calculated in other studies [Hawley & Krolik, 2006, McKinney, 2006], though each used different floor schemes.

2.5 Summary and Conclusion

We have presented numerical estimates of the optically thin emission from GRMHD accretion disk simulations scaled to Sgr A* conditions and commented on the character of the jet seen in similar runs.

Relativistic jets ($\gamma \lesssim 10$) are seen from our geometrically thick accretion disks that remain collimated at large distances ($r \gtrsim 1000M$). The energy flux is predominantly electromagnetic at small distances, but equipartition with the matter component is reached by $r \sim 100M$. Our results are qualitatively similar to other studies [Hawley & Krolik, 2006, McKinney, 2006].

The ray-traced images of Sgr A* predict that the black hole silhouette will only be obvious near $\lambda \simeq 1$mm if the disk is inclined less than $\sim 30°$ to the line of sight. By taking pictures of the disks at different frequencies, we were able to calculate spectra for different inclinations, black hole spins and time slices. Significant SED variations

were seen with respect to all these parameters, though degeneracies may exist for certain combinations of parameters. For instance, increasing a_* and $i_{\rm inc}$ seemed to increase the power at high frequencies, so a low spin hole with a large inclination angle may have a similar SED as a high spin hole with a small inclination angle.

Since the SED varies with time slice, we intend to take time averages of spectra to more accurately approximate real observations. In addition, we plan on adapting our ray-tracing code to consistently calculate polarization through plasma on a curved background. This will allow us to further constrain our model. Other improvements we plan to implement in the near future include removing the "frozen fluid" approximation which uses data from a single time slice to calculate the SED, adding Compton scattering and using 3D simulation data.

2.6 References

Baganoff, F. K., et al. 2001, Nature, 413, 45

Baganoff, F. K., et al. 2003, ApJ, 591, 891

Balbus, S. A., & Hawley, J. F. 1991, ApJ, 376, 214

Belanger, G., et al. 2006, arXiv:astro-ph/0604337v2

Beloborodov, A. M., et al. 2006, ApJ, 648, 405

Broderick, A. E., & Loeb, A. 2005, MNRAS, 363, 353

Broderick, A. E., & Loeb, A. 2006, ApJ, 636, L109

Broderick, A. E., & Loeb, A. 2006, MNRAS, 367, 905

Broderick, A. E., & Narayan, R. 2006, ApJ, 638, L21

Bromley, B. C., Chen, K., & Miller, W. A. 1997, ApJ, 475, 57

Beckwith, K., & Done, C. 2005, MNRAS, 359, 1217

Broderick, A., & Blandford, R. 2003, MNRAS, 342, 1280

Broderick, A., & Blandford, R. 2004, MNRAS, 349, 994

Chen, K., & Eardley, D. M. 1991, ApJ, 382, 125

Connors, P. A., Stark, R. F., & Piran, T. 1980, ApJ, 235, 224

Cunningham, C. T. 1975, ApJ, 202, 788

Cunningham, C. 1976, ApJ, 208, 534

De Villiers, J.-P., Staff, J., & Ouyed, R. 2005, arXiv:astro-ph/0502225v2

Doeleman, S., & Bower, G. 2004, Galactic Center Newsletter, 18, 6

Dovčiak, M., Karas, V., & Yaqoob, T. 2004, ApJS, 153, 205

Eisenhauer, F., et al. 2005, ApJ, 628, 246

Falcke, H., et al. 1996, ApJ, 464, L67

Falcke, H., et al. 1998, ApJ, 499, 731

Falcke, H., & Markoff, S. 2000, A&A, 362, 113

Falcke, H., Melia, F., & Agol, E. 2000, ApJ, 528, L13

Fender, R., & Belloni, T. 2004, ARAA, 42, 317

Ferrarese, L., & Ford, H. 2005, Sp. Sci. Rev., 116, 523

Ferrari, A. 1998, ARAA, 36, 539

Fishbone, L. G., & Moncrief, V. 1976, ApJ, 207, 962

Fuerst, S. V., & Wu, K. 2004, A&A, 424, 773

Gammie, C. F., McKinney, J. C., Tóth, G. 2003, ApJ, 589, 444

Ghez, A. M., et al. 2005, ApJ, 620, 744

Goldston, J. E., Quataert, E., & Igumenshchev, I. V. 2005, ApJ, 621, 785

Harris, D. E., & Krawczynski, H. 2006, ARAA, 44, 463

Hawley, J. F., & Krolik, J. H. 2006, ApJ, 641, 103

Hollywood, J. M., & Melia, F. 1997, ApJS, 112, 423

Hornstein, S. D., et al. 2002, ApJ, 577, L9

Karas, V., Vokrouhlicky, D., & Polnarev, A. G. 1992, MNRAS, 259, 569

Kurganov, A., & Tadmor, E. 2000, J. Comp. Phys., 160, 241

Laor, A., Netzer, H., & Piran, T. 1990, MNRAS, 242, 560

Leung, P. K., Noble, S. C., & Gammie, C. F. 2007, in progress

Lindquist, R. W. 1966, Ann. of Phys., 37, 487

Macquart, J.-P., et al. 2006, ApJ, 646, L111

Marrone, D. P., et al. 2006, ApJ, 640, 308

Marrone, D. P., et al. 2006, arXiv:astro-ph/0607432v2

McKinney, J. C. 2006, MNRAS, 368, 1561

McKinney, J. C., & Gammie, C. F. 2004, ApJ, 611, 977

Meyer, L., et al. 2006, A&A, 460, 15

Mihalas, D., & Weibel-Mihalas, B. 1999, Foundations of Radiation Hydrodynamics (Mineola: Dover)

Mirabel, I. F., & Rodríguez, L. F. 1999, ARAA, 37, 409

Misner, C. W., Thorne, K. S., & Wheeler, J. A. 1973, Gravitation (New York: Freeman)

Narayan, R. 2002, ESO Sym.: Lighthouses of the Universe, 405

Noble, S. C., et al. 2006, ApJ, 641, 626

Noble, S. C., Leung, P. K., Gammie, C. F., & Book, L. G. 2007, Class. Quantum Grav., 24, S259

Rauch, K. P., & Blandford, R. D. 1994, ApJ, 421, 46

Remillard, R. A., & McClintock, J. E. 2006, ARAA, 44, 49

Schnittman, J. D., & Bertschinger, E. 2004, ApJ, 606, 1098

Schnittman, J. D., Krolik, J. H., & Hawley, J. F 2006, ApJ, 651, 1031

Serabyn, E., et al. 1997, ApJ, 490, L77

Speith, R., Riffert, H., & Ruder, H. 1995, Computer Phys. Comm., 88, 109

Tóth, G. 2000, J. Comp. Phys., 161, 605

Yuan, F., Markoff, S., & Falcke, H. 2002, A&A, 383, 854

Yuan, F., Quataert, E., & Narayan, R. 2003, ApJ, 598, 301

Wardziński, G., & Zdziarski, A. A. 2000, MNRAS¡ 314, 183

Zhao, J.-H., et al. 2003, ApJ, 586, L29

Chapter 3

Numerical Calculation of Magnetobremsstrahlung Emission and Absorption Coefficients

3.1 Introduction

In many astronomical plasmas the electron distribution includes an approximately thermal, mildly relativistic component. One such system of particular interest to us is Sgr A*, the radio source that is likely sited in a plasma surrounding the black hole at the galactic center. As theoretical models of such systems advance, it is useful to have a fast, accurate scheme to calculate the magneto-bremsstrahlung (MBS), or cyclo-synchrotron, spectra. It is particularly desirable to be able to evaluate the necessary absorption and emission coefficients for polarized radiation from a general electron distribution, since in the collisionless conditions common in low luminosity active galactic nuclei electron distributions are unlikely to precisely follow the commonly assumed thermal or power-law forms.[1]

Usually MBS spectra are calculated using emission and absorption coefficients derived under an ultrarelativistic (synchrotron) approximation or, for mildly relativistic electrons, using approximate fitting formulae. The fitting formulae are accurate over a limited range in frequency ν, field strength B, observer angle θ (the angle between the emitted or absorbed photon and the magnetic field vector $\mathbf{B}$), or characteristic Lorentz factor for the electrons. In this work we provide, test, and apply a general scheme for calculating MBS emission and absorption coefficients. One potential application of our methods is to generate new, more accurate, computationally efficient fitting formulae over the range of interest.

Approximate calculations of MBS emission and absorption coefficients have a rich history. In the ultrarelativistic limit, emission of an electron with Lorentz factor γ is limited to a cone defined by the oscillating velocity vector of the electron, with angular width $1/\gamma$. This leads to an approximate expressions for $dP/d\nu$ [Bekefi, 1966, Rybicki & Lightman, 1979, Westfold, 1959], the power per unit frequency interval. However,

[1]This work were submitted in 2009 to ApJ [Leung, Gammie & Noble, 2009]. Reproduction for this dissertation is authorized by the copyright holder.

for $\gamma \sim 1$, the approximation worsens, cyclotron line features begin to appear in the spectrum, and the ultrarelativistic approximation must be abandoned.

For mildly relativistic electrons the emission is still mainly perpendicular to the magnetic field. This fact can be used to develop approximate analytic expressions for the emissivity. Petrosian [1981] used the method of steepest descent, and an asymptotic expansion of the Bessel functions, to find the emissivity of mildly relativistic thermal electrons (see also Pacholczyk [1970]).

Robinson & Melrose [1984] and Dulk [1985] improved Petrosian [1981]'s calculation for thermal electrons at temperature T by using more accurate asymptotic expansions of the Bessel functions that appear in the exact expression for the emissivity, and some interpolation formulae, to provide a thermal MBS emissivity that is valid over a wide range in T, ν, θ, and B. Brainerd & Lamb [1987] calculate numerically emissivity for various distributions and energy injection functions. Chanmugam et al. [1989] compared several approximate equations with numerical results in the cyclotron limit and concluded that Robinson & Melrose [1984] gave the best result. Mahadevan, Narayan & Yi [1996] found approximate formulae for θ-averaged emission coefficient by fitting to a direct numerical evaluation of the emissivity.

Wardzinski & Zdziarski [2000] combined the approximate equations in Petrosian [1981] and Petrosian & McTiernan [1983] to find an approximate emissivity accurate over a larger range of temperature. Their expressions contain a slight discontinuity, however, because they joined two asymptotic limits without smoothing the intermediate regime. They also found an approximate θ-averaged emissivity.

For polarized light, Kawabata [1964] and Meggitt & Wickramasinghe [1982] gave complicated but exact integral expressions for the specific emissivities in the Stokes formalism, but they did not provide any easily evaluated approximations. Väth & Chanmugam [1995] used the results of Robinson & Melrose [1984] to obtain the approximate equations and compared the results with a direct numerical evaluation of the emissivity in the cyclotron regime.

We began this work because, in attempting to calculate polarized emission spectra for Sgr A*, we found we needed to evaluate the accuracy of earlier approximate expressions in the regime of interest to us. Here we provide what we hope is a transparent, well-documented procedure that will enable others to avoid our descent into the minutiae of synchrotron theory. Our MBS calculator has a broad range of validity (described in §3.4) and should therefore be useful for anyone seeking to obtain or test approximate expressions in their domain of interest.

The main approximations we make are (1) $(\nu/\nu_{\rm p})^2 \gg 1$ and (2) $(\nu/\nu_{\rm p})^2(\nu/\nu_c) \gg 1$,

where the electron plasma frequency

$$\nu_{\rm p} \equiv \left(\frac{n_e e^2}{\pi m_e}\right)^{1/2} = 8980 n_e^{1/2}\,{\rm Hz} \tag{3.1}$$

(we use Gaussian/cgs units throughout) and the electron cyclotron frequency

$$\nu_c \equiv \frac{eB}{2\pi m_e c} = 2.8\times 10^6 B\,{\rm Hz}\ . \tag{3.2}$$

When these conditions are violated the index of refraction is noticeably different from 1 and corrections must be made throughout our formalism.

The plan of this paper is as follows. In §3.2 we fix notation by writing down the equations of polarized radiative transfer in Stokes and Cartesian polarization bases. In §3.3 we discuss methods for calculating the emission and absorption coefficients for a general distribution function. In §3.4 we recall the usual asymptotic expressions that can be used as code checks. In §3.5 we describe our numerical code, called `harmony`. In §3.6 we evaluate the accuracy of earlier work and provide a convenient fitting formula for the total emissivity (and therefore absorptivity) of thermal electrons with $\Theta_e \equiv kT_e/(m_e c^2) \gtrsim 0.5$. Appendix A.1 briefly describes the distinction between emitted and received power. Appendix A.2 describes an accurate and efficient scheme for evaluating high order Bessel functions.

3.2 Radiative Transfer

We are concerned with electromagnetic wave propagation at frequency ν in the frame of a magnetized, ionized plasma. The plasma may have a thermal electron component with dimensionless temperature Θ_e; there may also be a nonthermal component in the electron distribution.

In the regime of interest an electromagnetic wave can be written as a sum of the magnetoionic modes of the plasma, the ordinary (O) and extraordinary (X) modes. For a cold plasma these modes are nearly circularly polarized except for propagation in a narrow range of angles perpendicular to the field. In general the modes are elliptically polarized.

The polarization properties of the magnetoionic modes are described by a pair of orthonormal basis vectors $\mathbf{e}_O$ and $\mathbf{e}_X$. Let T_O (T_X) be the transverse component of the polarization vector of the ordinary (extraordinary) mode, with $|T_X| \le 1$. In other words, $|T_{O,X}|$ are the axial ratios of the orthogonal polarization ellipses, so that

$T_O T_X = -1$. Then

$$\mathbf{e}_O \equiv \{e_{O1}, e_{O2}\} = \frac{1}{\sqrt{T_X^2 + 1}} \{-1, iT_X\} \tag{3.3}$$

and

$$\mathbf{e}_X \equiv \{e_{X1}, e_{X2}\} = \frac{1}{\sqrt{T_X^2 + 1}} \{T_X, i\} \tag{3.4}$$

where $\{x, y\}$ are the Cartesian components of a vector in the plane perpendicular to the direction of propagation $\hat{z}$, and $\hat{y}$ is perpendicular to the magnetic field so that $\hat{x} \times \hat{y} \equiv \hat{z}$. The electric field of mode A is $\mathbf{E} = E\ \mathbf{e}_A\ \exp(ikz - i\omega t)$. In writing these equations we have assumed that the polarization modes are orthogonal, valid when $\nu^3/({\nu_\mathrm{p}}^2 \nu_c) \gg 1$.

3.2.1 Descriptions of Polarized Radiation

The polarized intensity is most familiarly described by the Stokes vector

$$I_S = \{I, Q, U, V\}\ ; \tag{3.5}$$

here all components have the usual intensity units, $dE/dtd^2x d\nu d\Omega$, i.e. energy per unit time per unit area per unit frequency per unit solid angle.

The polarized intensity can also be described in terms of a polarization tensor written in a Cartesian coordinate basis (* denotes complex conjugate):

$$I_{ij} \equiv \frac{I}{E^2} \langle E_i E_j^* \rangle = \frac{1}{2} \begin{pmatrix} I + Q & U + iV \\ U - iV & I - Q \end{pmatrix} \tag{3.6}$$

where $i, j \in \{x, y\}$ and the prefactor converts the tensor to intensity units.

Finally, the polarized intensity can be described by a polarization tensor in the mode basis

$$I_{AB} = e_{Ai}^* e_{Bj} I_{ij} = \frac{1}{2} \begin{pmatrix} I - Q\cos\chi - V\sin\chi & -V\cos\chi + Q\sin\chi - iU \\ -V\cos\chi + Q\sin\chi + iU & I + Q\cos\chi + V\sin\chi \end{pmatrix} \tag{3.7}$$

where $A, B \in \{O, X\}$ and $\chi = \tan^{-1} T_X$.

3.2.2 Polarized Radiative Transfer

In the Stokes basis in a uniform plasma the radiative transfer equation is

$$\frac{d}{ds} I_S = J_S - \mathbf{M}_{ST} I_T \tag{3.8}$$

where $J_S = \{j_I, j_Q, j_U, j_V\}^\mathsf{T}$ contains the emission coefficients, which have units of $dE/dtdVd\nu d\Omega$, and the Mueller Matrix $\mathbf{M}_{ST}$ is

$$\mathbf{M}_{ST} \equiv \begin{pmatrix} \alpha_I & \alpha_Q & \alpha_U & \alpha_V \\ \alpha_Q & \alpha_I & r_V & -r_U \\ \alpha_U & -r_V & \alpha_I & r_Q \\ \alpha_V & r_U & -r_Q & \alpha_I \end{pmatrix} . \tag{3.9}$$

The parameters α_i are the absorption coefficients and r_Q, r_U and r_V are what we will call Faraday mixing coefficients. j_U, α_U, r_U are zeros for our choice of basis vectors. Below, we will provide a scheme for evaluating the emission and absorption coefficients.

In the Cartesian polarization tensor basis in a uniform plasma the transfer equation is

$$\frac{dI_{ij}}{ds} = J_{ij} - \mu_{ijkl} I_{kl} \tag{3.10}$$

where the tensor μ describes absorption and Faraday rotation.

In the mode basis in a uniform plasma

$$\frac{dI_{AB}}{ds} = J_{AB} - \mu_{ABCD} I_{AB} \, . \tag{3.11}$$

We define α_A by

$$\frac{dI_{AA}}{ds} = -\alpha_A I_{AA} \, , \tag{3.12}$$

for radiation consisting of a single mode in the absence of emission and Faraday rotation we use

3.3 Magnetobremsstrahlung Emission and Absorption

We are now ready to calculate absorption and emission coefficients. These are frame-dependent. We will evaluate them in the plasma center-of-momentum frame (the

expressions given below do not assume this). The total emission and absorption coefficients can be transformed using the Lorentz invariance of j_ν/ν^2 and $\nu\alpha_\nu$. The transformation of the full absorption matrix will be discussed in future work.

3.3.1 Emissivity

A consistent procedure for calculating the emission and absorption coefficients can be found in Melrose & McPhedran [1991]. Beginning with their Eq. (22.20), rotating the velocity potentials V_i onto a basis where the z direction is aligned with the wavevector, and introducing appropriate leading constants, the emissivity in the Cartesian polarization basis is

$$J_{ij} = \frac{2\pi e^2 \nu^2}{c} \int d^3p \; f \sum_{n=1}^{\infty} \delta(y_n) \, K_{ij} \tag{3.13}$$

where

$$K_{xx} = M^2 J_n^2(z) \; , \tag{3.14}$$

$$K_{yy} = N^2 J_n'^2(z) \; , \tag{3.15}$$

$$K_{xy} = -K_{yx} = -iMN J_n(z) J_n'(z) \; , \tag{3.16}$$

and

$$y_n \equiv \frac{n\nu_c}{\gamma} - \nu(1 - \beta \cos\xi \cos\theta) = \frac{1}{2\pi}(\omega - n\Omega - k_\parallel v_\parallel) \tag{3.17}$$

is the argument of the δ function in the resonance condition, $\Omega = 2\pi\nu_c/\gamma$ is the relativistic electron cyclotron angular frequency, $\beta \equiv v/c$, v is the electron speed, ξ is the electron pitch angle,

$$z \equiv \frac{\nu\gamma\beta \sin\theta \sin\xi}{\nu_c} = \frac{k_\perp v_\perp}{\Omega} \tag{3.18}$$

$$M \equiv \frac{\cos\theta - \beta\cos\xi}{\sin\theta} \; , \tag{3.19}$$

$$N \equiv \beta \sin\xi \; , \tag{3.20}$$

$$f \equiv \frac{dN_e}{d^3x d^3p} = \frac{dn_e}{d^3p} \tag{3.21}$$

is the electron distribution function, d^3x and d^3p are differential volumes in real space and momentum space respectively. Subscripts $\parallel$ and $\perp$ refer to components of vectors parallel and perpendicular to $\mathbf{B}$.

The emissivity in the Stokes basis can be found using the transformation implied by equation (3.6):

$$J_S = \frac{2\pi e^2 \nu^2}{c} \int d^3p\, f \sum_{n=1}^{\infty} \delta(y_n)\, K_S \tag{3.22}$$

where

$$K_I = M^2 J_n^2(z) + N^2 J_n'^2(z)\ , \tag{3.23}$$

$$K_Q = M^2 J_n^2(z) - N^2 J_n'^2(z)\ , \tag{3.24}$$

$$K_U = 0 \tag{3.25}$$

and

$$K_V = -2MN J_n(z) J_n'(z)\ . \tag{3.26}$$

In the mode basis

$$J_{AB} = \frac{2\pi e^2 \nu^2}{c} \int d^3p\, f \sum_{n=1}^{\infty} \delta(y_n) K_{AB} \tag{3.27}$$

where

$$K_{XX} = \frac{\left[MT_X J_n(z) + N J_n'(z)\right]^2}{1+T_X^2}\ , \tag{3.28}$$

$$K_{OO} = \frac{\left[M J_n(z) - NT_X J_n'(z)\right]^2}{1+T_X^2}\ , \tag{3.29}$$

and

$$K_{XO} = K_{OX} = -\frac{\left[M J_n(z) - NT J_n'(z)\right]\left[MT J_n(z) + N J_n'(z)\right]}{1+T_X^2}\ . \tag{3.30}$$

In the cold plasma limit, the axial ratios are [e.g. Melrose, 1989]

$$T_{O,X} \equiv T_{\pm} \approx \frac{2\nu\cos\theta}{\nu_c \sin^2\theta \mp \sqrt{\nu_c^2 \sin^4\theta + 4\nu^2\cos^2\theta}} \qquad \text{for } \nu \gg \nu_{\rm p}\ . \tag{3.31}$$

The polarized emissivities are related to the total emissivity by

$$j_\nu \equiv J_I = J_{xx} + J_{yy} = J_{OO} + J_{XX} \equiv \int d^3p\, f\, \eta_\nu \tag{3.32}$$

where

$$\eta_\nu \equiv \frac{dE}{d\nu dt d\Omega} \tag{3.33}$$

is the single-electron emissivity.

3.3.2 Absorption coefficients

If the distribution function is thermal then the absorption coefficients follow from Kirchhoff's law. For a nonthermal plasma we must calculate the absorption coefficients directly.

If the plasma is weakly anisotropic (i.e. the anisotropic effect is perturbative) then it is possible to simply relate the absorption coefficients to the anisotropic, antihermitian part of the dielectric tensor. Starting with the dielectric tensor of a magnetized plasma (Eq. (22.47) of Melrose & McPhedran [1991], corrected by a factor of $4\pi/\omega^2$, or Eq. (10-48) of Stix [1992], and using the Plemelj relation to find the imaginary part of the integral over momentum space (and thus the antihermitian part of the dielectric tensor) we find

$$\mu_{ijkl} = \frac{ce^2}{\nu} \int d^3p \; Df \; \sum_{n=1}^{\infty} \delta(y_n) K_{ijkl} \tag{3.34}$$

where

$$K_{xxxx} = M^2 J_n^2(z) \; , \tag{3.35}$$

$$K_{xxyx} = K_{xyxx} = K_{xyyy} = K_{yyyx} = -\frac{i}{2} MN J_n(z) J_n'(z) \; , \tag{3.36}$$

$$K_{xxxy} = K_{yxxx} = K_{yxyy} = K_{yyxy} = \frac{i}{2} MN J_n(z) J_n'(z) \; , \tag{3.37}$$

$$K_{xyxy} = K_{yxyx} = \frac{1}{2} \left[M^2 J_n^2(z) + N^2 J_n'^2(z) \right] \; , \tag{3.38}$$

$$K_{yyyy} = N^2 J_n'^2(z) \; , \tag{3.39}$$

all other components of K vanish, and the operator D is

$$Df \equiv \left(\frac{\omega - k_\parallel v_\parallel}{v_\perp} \frac{\partial}{\partial p_\perp} + k_\parallel \frac{\partial}{\partial p_\parallel} \right) f \; . \tag{3.40}$$

In writing this equation we assume that the the energy of the absorbed photon is small compared to the width of the distribution function, permitting us to replace a difference with the derivative operator D. For a thermal distribution this requires that $h\nu/kT_e \ll 1$.

In terms of $p = |\mathbf{p}|$ and $\cos\xi$, the operator D is

$$Df = \frac{2\pi\nu}{c\beta} \left(\frac{\partial}{\partial p} + \frac{\beta\cos\theta - \cos\xi}{p} \frac{\partial}{\partial \cos\xi} \right) f \; , \tag{3.41}$$

and in terms of γ and $\cos\xi$,

$$Df = 2\pi\nu \left(\frac{1}{m_e c^2} \frac{\partial}{\partial \gamma} + \frac{\beta\cos\theta - \cos\xi}{p\beta c} \frac{\partial}{\partial \cos\xi} \right) f \ . \tag{3.42}$$

In the Stokes basis,

$$\alpha_S = -\frac{ce^2}{2\nu} \int d^3p \sum_{n=1}^{\infty} \delta(y_n) \ Df \ K_S \tag{3.43}$$

where subscript S is one of I, Q, U and V. In the mode basis

$$\alpha_A = -\frac{ce^2}{\nu} \int d^3p \sum_{n=1}^{\infty} \delta(y_n) \ Df \ K_{AA} \tag{3.44}$$

where subscript A is O or X.

Let us explicitly verify Kirchhoff's law for a thermal distribution function in the Stokes basis:

$$J_S - \alpha_S B_\nu = 0 \tag{3.45}$$

where $B_\nu = (2h\nu^3/c^2)[\exp(h\nu/kT_e) - 1]^{-1}$ is the Planck function. Using equations (3.22) and (3.43), and gathering like terms, this becomes

$$\int d^3p \sum_{n=1}^{\infty} \delta(y_n) K_S \left(\frac{2\pi e^2 \nu^2}{c} f + \frac{ce^2}{2\nu} Df \ \ B_\nu \right) = 0 \ . \tag{3.46}$$

If we make γ the nontrivial momentum space coordinate then $f = \mathcal{N} \exp(-\gamma/\Theta_e)$, where $\mathcal{N}(\Theta_e)$ is a normalization constant, and $Df = -2\pi\mathcal{N}\nu \exp(-\gamma/\Theta_e)/(m_e c^2 \Theta_e)$. This leaves

$$\int d^3p \sum_{n=1}^{\infty} \delta(y_n) K_S \left(\frac{2\pi e^2 \nu^2}{c} \right) \mathcal{N} e^{-\gamma/\Theta_e} \left(1 - \frac{h\nu/(kT_e)}{\exp(h\nu/(kT_e)) - 1} \right) = \mathcal{O}\left(\frac{h\nu}{kT_e} \right) \ . \tag{3.47}$$

This is consistent with the assumption that the energy of the absorbed photon is small compared to the width of the distribution function; to lowest order in $h\nu/kT_e$ Kirchhoff's law is satisfied.

3.3.3 Electron Distribution Function

The electron distribution can be written using a variety of momentum space coordinates, and this can be a source of some confusion. For example, with respect to the auxiliary momentum coordinates γ, ξ and ϕ (the longitudinal coordinate), d^3p can

be expressed as $m_e^3 c^3 \gamma^2 \beta d\gamma d(\cos\xi) d\phi$ and the distribution function as

$$f \equiv \frac{dn_e}{d^3p} = \frac{1}{m_e^3 c^3 \gamma^2 \beta} \frac{dn_e}{d\gamma d(\cos\xi) d\phi} = \frac{1}{2\pi m_e^3 c^3 \gamma^2 \beta} \frac{dn_e}{d\gamma d(\cos\xi)} \ , \tag{3.48}$$

where the final equality arises from assuming the distribution is independent of ϕ. Equation (3.43) becomes

$$\alpha_S = -\frac{ce^2}{2\nu} \int d\gamma d(\cos\xi) \sum_{n=1}^{\infty} \delta(y_n) \, \gamma^2 \beta D \left[\frac{1}{\gamma^2 \beta} \frac{dn_e}{d\gamma d(\cos\xi)} \right] K_S \tag{3.49}$$

and similarly for the absorption coefficients in the mode basis.

The thermal (relativistic Maxwellian) distribution function is

$$\frac{dn_e}{d\gamma d\Omega_p} \equiv \frac{dn_e}{d\gamma d\phi d(\cos\xi)} = \frac{n_e}{4\pi\Theta_e} \frac{\gamma(\gamma^2-1)^{1/2}}{K_2(1/\Theta_e)} \exp\left(-\frac{\gamma}{\Theta_e}\right) \ ; \tag{3.50}$$

$d\Omega_p$ is a differential solid angle in momentum space and K_2 is a modified Bessel function of the second kind.

A useful nonthermal distribution function is the isotropic power-law distribution

$$\frac{dn_e}{d\gamma d\Omega_p} = \frac{n_e^{\rm NT}(p-1)}{4\pi(\gamma_{\rm min}^{1-p} - \gamma_{\rm max}^{1-p})} \gamma^{-p} \qquad \text{for } \gamma_{\rm min} \le \gamma \le \gamma_{\rm max} \ , \tag{3.51}$$

where $n_e^{\rm NT}$ is the number density of nonthermal electrons,

3.4 Ultrarelativistic Limit

For clarity it is helpful to record the emission and absorption coefficients for a thermal electron distribution and for a power-law distribution of electrons in the ultrarelativistic limit. These are well known but presented here in a consistent set of units and notation so that we can check our numerical results.

The emissivity of a single ultrarelativistic electron can be reduced through a standard approximation [e.g. Ginzburg, 1970, Westfold, 1959]

$$\int d\Omega_p \eta_\nu \simeq \frac{\sqrt{3} e^3 B \sin\theta}{m_e c^2} F\left(\frac{\nu}{\nu_{\rm cr}}\right) \tag{3.52}$$

where $\nu_{\rm cr} = (3/2)\nu_c \sin\theta\gamma^2$, and the synchrotron function

$$F(x) \equiv x \int_x^\infty dt K_{5/3}(t) \ . \tag{3.53}$$

The asymptotic expansions of $F(x)$ are

$$F(x) = \left\{ \begin{array}{ll} 2^{2/3}\Gamma(2/3)x^{1/3} + O(x) & \text{for } x \ll 1, \\ \left(\frac{\pi x}{2}\right)^{1/2} \exp(-x)\left(1 + O(x^{-1})\right) & \text{for } x \gg 1 \ . \end{array} \right\} . \tag{3.54}$$

For a thermal distribution with $\Theta_e \gg 1$, so that $K_2(1/\Theta_e) \simeq 2\Theta_e^2$ and

$$\frac{dn_e}{d\gamma d\Omega_p} \simeq \frac{n_e \gamma^2}{8\pi\Theta_e^3} \exp(-\gamma/\Theta_e) \ . \tag{3.55}$$

For $\nu \ll \nu_s \equiv (2/9)\nu_c \Theta_e^2 \sin\theta$, the small-$x$ limit of equation (3.54) can be used, most of the emission comes from electrons with $\gamma \sim \Theta_e$, and the emissivity is

$$j_\nu \simeq \frac{2^{4/3}\pi}{3} \frac{n_e e^2 \nu_s}{c\Theta_e^2} X^{1/3} \tag{3.56}$$

where

$$X \equiv \frac{\nu}{\nu_s} \ . \tag{3.57}$$

For $\nu \gg \nu_s$ the large-x limit of equation (3.54) applies. The integrand is proportional to $\exp(-\gamma/\Theta_e - \nu/\nu_{\rm cr})$, where $\nu_{\rm cr} \sim \gamma^2$, so the peak emission is from electrons with $\gamma \sim (\nu\Theta_e/(\nu_c \sin\theta))^{1/3}$. Then

$$j_\nu \simeq n_e \frac{\sqrt{2}\pi e^2 \nu_s}{6\Theta_e^2 c} X \exp(-X^{1/3}) \ , \tag{3.58}$$

and the integral has been evaluated using the method of steepest descent [Petrosian, 1981].

For the isotropic power-law distribution of electrons the integration can be done explicitly without using the asymptotic expansion for $F(x)$ if $p > 1$. Most of the emission comes from electrons with $\gamma^2 \sim \nu/\nu_c$, and the emissivity is [Blumenthal & Gould, 1970]

$$j_\nu = n_e^{\rm NT} \left(\frac{e^2\nu_c}{c}\right) \frac{3^{p/2}(p-1)\sin\theta}{2(p+1)(\gamma_{\rm min}^{1-p} - \gamma_{\rm max}^{1-p})} \Gamma\left(\frac{3p-1}{12}\right) \Gamma\left(\frac{3p+19}{12}\right) \left(\frac{\nu}{\nu_c \sin\theta}\right)^{-(p-1)/2} \tag{3.59}$$

for $\gamma_{\rm min}^2 \ll \nu/\nu_c \ll \gamma_{\rm max}^2$. The absorptivity, famously, cannot be obtained from Kirchhoff's law, but can be evaluated using equation (3.43). The result is (see, e.g., Rybicki & Lightman for a discussion):

$$\alpha_\nu = n_e^{\rm NT} \left(\frac{e^2}{\nu m_e c}\right) \frac{3^{(p+1)/2}(p-1)}{4(\gamma_{\rm min}^{1-p} - \gamma_{\rm max}^{1-p})} \Gamma\left(\frac{3p+2}{12}\right) \Gamma\left(\frac{3p+22}{12}\right) \left(\frac{\nu}{\nu_c \sin\theta}\right)^{-(p+2)/2} \tag{3.60}$$

again for $\gamma_{\rm min}^2 \ll \nu/\nu_c \ll \gamma_{\rm max}^2$. Notice that this expression for the absorptivity is proportional to $n_e^{\rm NT} e^2/(\nu m_e c)$. Since $(n_e^{\rm NT} e^2/m_e)^{1/2}$ is a plasma frequency for the nonthermal electrons, the absorption coefficient has the expected dimensions of 1/length.

3.5 Numerical Calculations

The emission and absorption coefficients all require the numerical evaluation of expressions of the following form:

$$\int_1^\infty d\gamma \int_{-1}^1 d\cos\xi \sum_{n=1}^\infty \delta(y_n) I(n,\xi,\gamma) \tag{3.61}$$

where I is some function, ξ is the electron pitch angle, γ is the electron Lorentz factor, and n is the harmonic index (see, e.g., equation (3.22)), and the resonance condition is

$$y_n \equiv \frac{n\nu_c}{\gamma} - \nu(1 - \beta\cos\xi\cos\theta) = 0 \tag{3.62}$$

which involves all three independent variables γ, ξ, and n. Recall that the resonance condition arises because each electron emits only at integer multiples of its own cyclotron frequency, Doppler shifted to the plasma rest frame.

3.5.1 Previous Work

Many have evaluated the absorption and emission coefficients numerically. Early efforts include the calculation of $j_\nu(\theta)$ by Takahara & Tsuruta [1982] for n up to several hundred. Melia [1994] calculated the emissivity numerically for $\theta = \pi/2$.

The emissivity is sharply peaked at particular ν; the integrand is not well-behaved. Mahadevan, Narayan & Yi [1996] resolved the resulting numerical difficulty by replacing the δ function with a broadening function of adjustable frequency width and evaluating the full three dimensional integral. Only an observer angle-averaged emis-

sion coefficient, $\bar{j_\nu} \equiv \int_0^1 j_\nu(\theta) d(\cos\theta)$, was found. The resonance condition was also used to simplify the integral.

Marcowith & Malzac [2003] found the angle-averaged emission coefficient by two methods. The first was similar to Mahadevan, Narayan & Yi [1996] except that a different broadening function was used. Another method, "direct integration", used the resonance condition to select an observer angle.

Wolfe & Melia [2006] calculated the angle-averaged single-particle emissivity and extended the summation to the 990th harmonic to increase the accuracy of the result. The calculation was done by replacing the δ function with a broadening function, as in Mahadevan, Narayan & Yi [1996]. The single-particle emissivity was then fitted with > 1500 coefficients over the range $-1 < \log_{10}(\nu/\nu_c) < 2$ and $0.1 < \beta < 0.98$. For the thermal emissivity, they explicitly evaluated the γ integral for $\beta < 0.97$; for $\beta > 0.97$ they used an approximation from Petrosian [1981]. They restricted their calculation to $-1 < \log_{10}(\nu/\nu_c) < 2$; they did not offer an explicit control for the accuracy of the $n \leq 990$ approximation for a particular γ.

3.5.2 Numerical Procedure

We use the resonance condition (3.62) to eliminate $\cos\xi$ from (3.61). This is simpler than eliminating γ (because the resonance condition is quadratic in β), and also simpler than eliminating n (because n must take on integer values). The remaining integral has the form

$$\int_{\gamma_-}^{\gamma_+} d\gamma \sum_{n=n_-}^{\infty} \left(\frac{1}{\nu\beta|\cos\theta|} \right) I(n, \xi, \gamma) \tag{3.63}$$

and the term in parentheses, $|dy_n/d\cos\xi|^{-1}$, comes from integrating over the δ function. The range of integration is now restricted by the requirements that $|\cos\xi| < 1$ and that γ be real.

The limits on the γ integration follow from $|\cos\xi| < 1$. Write the resonance condition

$$\cos\xi = \frac{\gamma\nu - n\nu_c}{\gamma\nu\beta\cos\theta} , \tag{3.64}$$

and set $\cos\xi = \pm 1$ to find

$$\gamma_\pm = \frac{n\nu_c/\nu \pm |\cos\theta| \sqrt{(n\nu_c/\nu)^2 - \sin^2\theta}}{\sin^2\theta} . \tag{3.65}$$

Notice that γ_- reaches a minimum of 1 for $n\nu_c/\nu = 1$, so $\gamma_- \geq 1$.

The argument of the square root in equation (3.65) must be non-negative. This restricts the range of n to

$$n \;\geq\; n_- = \frac{\nu}{\nu_c}|\sin\theta| \;. \tag{3.66}$$

At n_-, $\gamma_+ = \gamma_-$.

We need to choose an order to evaluate the integrals (sums) in equation (3.63). If the sum is done first then the remaining integrand is a rapidly varying, comb-like, function of γ for θ close to $\pi/2$. If the γ integration is done first the remaining summand is a smooth function of n, and therefore more numerically tractable. We therefore do the γ integration first.

3.5.3 Upper Limit of Summation

The summation in (3.63) extends to $n = \infty$, so for numerical summation we must either map n onto a finite domain or else choose an upper limit n_+ to the sum, beyond which the integrand is negligible. We have taken the latter approach.

For the special case of a thermal electron distribution we set $n_+ = Cn_{\rm peak}$, where the integrand peaks near $n_{\rm peak}$ and $C > 1$ is a dimensionless constant. At $\nu \ll \nu_c\Theta_e^2$, the integrand peaks when $J_n(z)$ peaks, at $z/n \simeq 1$, i.e. near

$$n = n_{\rm peak} = \gamma\frac{\nu}{\nu_c}(1 - \beta^2\cos^2\theta) \;. \tag{3.67}$$

The thermal distribution is proportional to $\exp(-\gamma/\Theta_e)/K_2(1/\Theta_e)$. This peaks at $\gamma \sim 1 + \Theta_e$ for all Θ_e, so

$$n_{\rm peak} \simeq (\Theta_e + 1)(\nu/\nu_c)(1 - \beta^2\cos^2\theta) \tag{3.68}$$

is a good estimate for all Θ_e.

For $\nu \gg \nu_c\Theta_e^2$ we can use the asymptotic expression for the single electron emissivity to estimate $n_{\rm peak}$ (see §3.5). The peak is near the peak of the function $\exp[-\gamma/\Theta_e - \nu/(\gamma^2\nu_c)]$, so most of the emission comes from electrons with $\gamma = (2\Theta_e\nu/\nu_c)^{1/3}$.

Combining the low-frequency and high-frequency estimates for $n_{\rm peak}$,

$$n_+ = C\left[\Theta_e + 1 + \left(2\Theta_e\frac{\nu}{\nu_c}\right)^{1/3}\right]\frac{\nu}{\nu_c}(1 - \beta^2\cos^2\theta) \;. \tag{3.69}$$

Typically $C = 10$ gives adequate accuracy.

For a nonthermal distribution we take an adaptive approach. We sum over successive intervals $[n_-, n_- + \Delta n]$, $[n_- + \Delta n + 1, 2(n_- + \Delta n)]$, $[2(n_- + \Delta n) + 1, 4(n_- + \Delta n)]$, etc., until the fractional contribution from the last interval is smaller than a preset tolerance. This procedure yields fast convergence except for exotic electron distribution functions. Some knowledge of the distribution is required, however, to set Δn.

3.5.4 Numerical Considerations

Accurate, efficient evaluation of the Bessel function $J_n(z)$ for $n \gg 1$ is essential for our calculation. When n is small, any mathematical library gives an accurate, efficient result. As n increases, however, standard mathematical libraries slow down, become inaccurate, and fail. In our calculations the argument z and order n of the Bessel functions can be large and are typically comparable in size (one can shown that $z/n < 1$). Standard asymptotic expansions (see [Abramowitz & Stegun, 1970]) are unsatisfactory because they typically assume $z \gg n$ or vice versa. We calculate J_n using a special-purpose code based on asymptotic expansions discussed in Chishtie et al. [2005], who divide the arguments into three regimes and provide asymptotic expansions for each regime. Details of our scheme are discussed in Appendix A.2.

The summation over n is done as an explicit sum at small n and as an integral at large n. The same approach was used by Takahara & Tsuruta [1982]. Approximating the sum as an integral at large n increases both speed and, in many cases, accuracy. The breakpoint, n_I, between summation and integration is set heuristically. Typically we use $n_I = 30$ for the parameters of interest to us.

We integrate using the GNU Scientific Library's QAG integrator, which is fast, robust, and publicly available. One subtlety here is connected to the narrow extent of the γ integrand when ν is large (this narrow extent permits one to use the method of steepest descent in evaluating equation (3.58)). If the domain of integration is not set correctly then the integrator can fail to resolve the peak and the emissivity, for example, will be underestimated.

Finally, notice that equation (3.63) fails for $\theta = \pi/2$ because the δ function does not contain $\cos\xi$ and so cannot be used to eliminate the $\cos\xi$ integral. But since $j_\nu(\theta)$ is a smooth function of θ with a maximum at $\theta = \pi/2$, we simply avoid evaluating the emissivity at $\theta = \pi/2$ by extrapolating from nearby θ. The error is of the same order as a single integration because of the zero slope around the peak. The only

penalty is that the time needed to find j_ν is doubled compared to the calculation at other θ.

3.6 Verification of Calculation

3.6.1 Monoenergetic Electrons

The angle-averaged synchrotron emissivity of ultrarelativistic monoenergetic electrons is

$$\bar{j}_\nu(\nu,\gamma) \simeq n_e \frac{1}{2}\int_{-1}^{1} \frac{\sqrt{3}e^3 B\sin\theta}{4\pi m_e c^2} F\left(\frac{\nu}{\nu_{\rm cr}}\right) d(\cos\theta) \equiv n_e \bar{\eta}_\nu \ . \tag{3.70}$$

The single-particle emissivity can be approximated as [Crusius & Schlickeiser, 1986, 1988, Schlickeiser & Lerche, 2007]

$$\bar{\eta}_\nu(\nu,\gamma) \approx \frac{\pi e^2 \nu}{2\sqrt{3}c\gamma^2} CS\left[\frac{2\nu}{3\nu_c\gamma^2}\right] \ , \tag{3.71}$$

where the function $CS(x)$ is given by

$$CS(x) = \frac{x^{-2/3}}{0.869 + x^{1/3}\exp(x)} \ . \tag{3.72}$$

We compute an approximation to the emissivity of a monoenergetic distribution by using a narrow Gaussian in energy; for small enough energy width ΔE the emissivity is independent of ΔE. Figure (3.1) compares equation (3.71) with the `harmony` result and the ultrarelativistic limit equation (3.70). At high frequency, `harmony` underestimates the emissivity because the integrand becomes too narrow to be resolved numerically. Evidently equation (3.72) has a maximum error of order $\approx 20\%$.

Wolfe & Melia [2006] fit the angle-averaged single-particle emissivity and provide a code that reproduces their fitting function. In Figure (3.2) compares results of `harmony` with their code, with the same parameters as their Figure 3c. The relative error of their fitting formula, compared to our "exact" numerical calculation, is somewhat larger than the error shown in their Figure 3c, perhaps due to our better resolution of the cyclotron peaks.

3.6.2 Thermal Distribution

At large ν and Θ_e, our emissivity agrees with the ultrarelativistic limit; this is discussed in greater detail in §3.7.

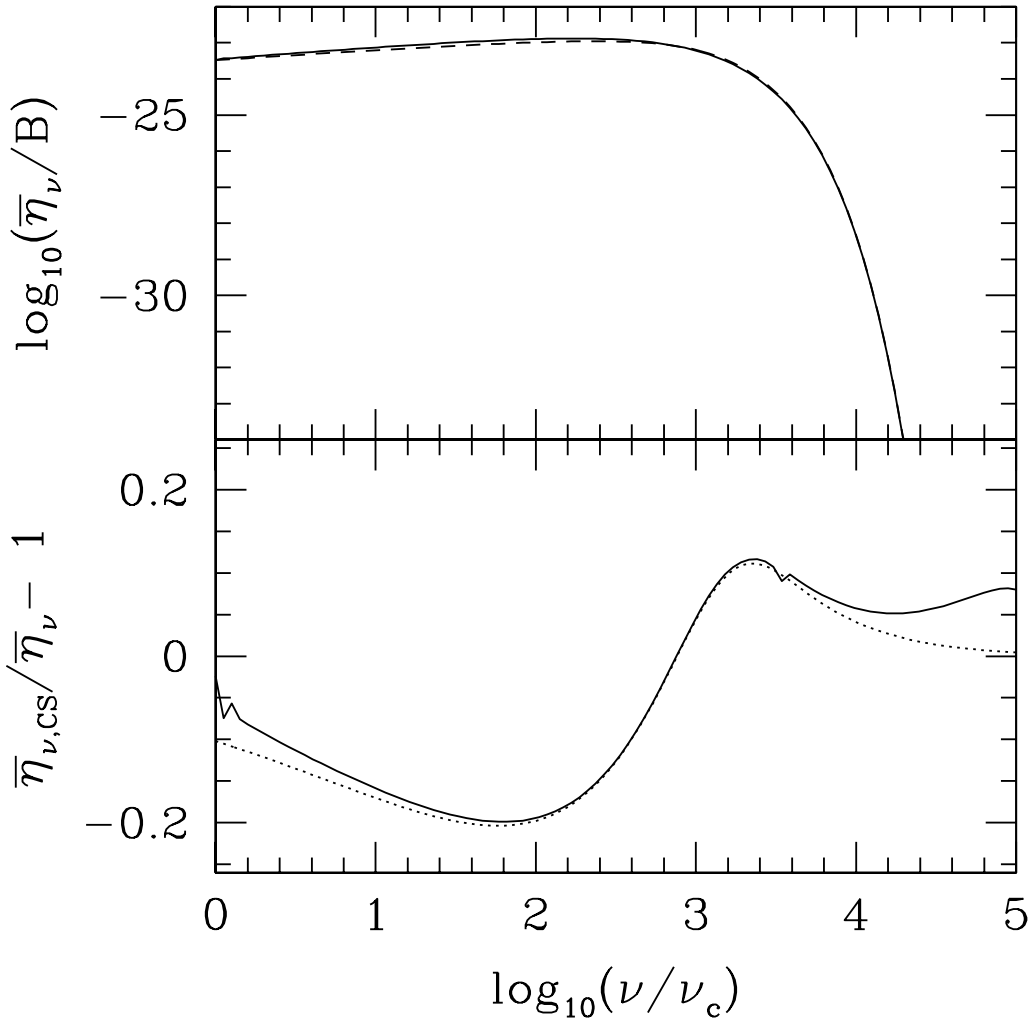

Figure 3.1 Upper panel: the angle-averaged single-particle emissivity $\bar{\eta}_\nu/B$, in cgs units, at $\beta = 0.999$. Solid line is result of `harmony`, and dashed line is calculated by using the approximate equation (3.71). Lower panel: solid line is the relative difference of equation (3.71) and result of `harmony`, dotted line is the difference between equation (3.71) and ultrarelativistic limit equation (3.70).

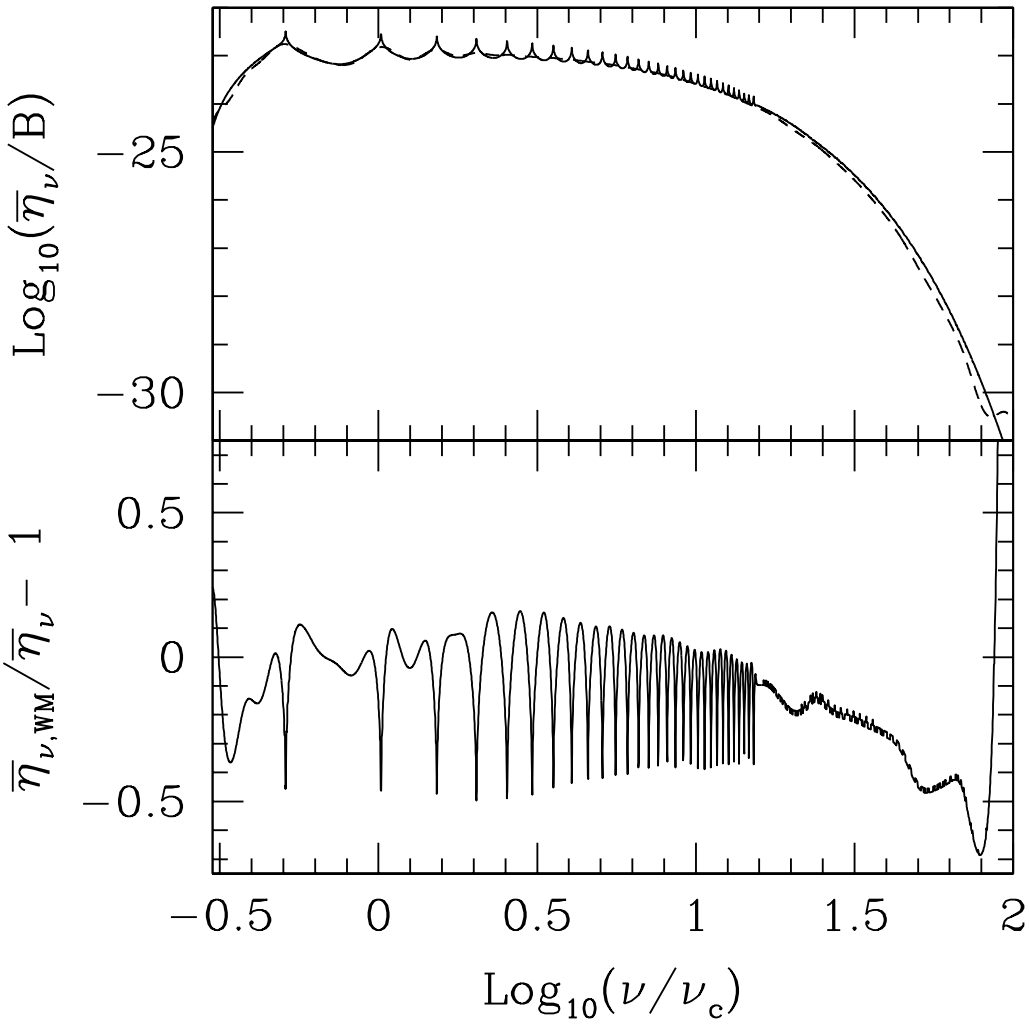

Figure 3.2 Upper panel: the angle-averaged single-particle emissivity $\bar{\eta}_\nu/B$, in cgs units, at $\beta = 0.86$. Solid line is result of `harmony`, and dashed line is result of Wolfe & Melia [2006] multiplied by a factor of π^2 (which we cannot explain). Lower panel: the relative difference of $\bar{\eta}_\nu$. Difference compared to Wolfe & Melia [2006, Fig. 3] seems to be due to better resolution of the cyclotron peaks in our calculation.

At low ν and Θ_e, where cyclotron features are prominent, we have compared our results with those in Väth & Chanmugam [1995] and Chanmugam et al. [1989] and found good agreement. Notice that although the expressions presented in Chanmugam et al. [1989] and Väth & Chanmugam [1995] allow for refractive index $\neq 1$, the deviation of the refractive index from 1 is small in our test examples, so we expect good agreement.

First we calculate the absorption coefficients in the Stokes basis and compare with Väth & Chanmugam [1995]. Figure (3.3) shows that α_Q calculated with `harmony` is within 0.2% of results of Väth & Chanmugam [1995]. α_I and α_V have similar relative differences. We then calculate the absorption coefficients in the mode basis. Figure (3.4) compares α_O from Chanmugam et al. [1989] with the results of `harmony`. Using the cold plasma approximation of T_X (equation (3.31)) in `harmony`, the relative differences of $\alpha_{O,X}$ are $\leq 0.2\%$ compared to results of Chanmugam et al. [1989].

As another check, at $\theta = \pi/2$, we eliminate the γ integration using the δ function. Since at $\theta = \pi/2$ the β dependence of the resonance condition is eliminated we are left with a single value for γ and a two-dimensional integral in $\cos\xi$ and n. This integration gives the same result as the γ-n integration.

3.6.3 Angle-averaged Thermal Emission

Mahadevan, Narayan & Yi [1996] provides a fitting formula to calculate the observer angle-averaged emissivity $\bar{j}_\nu$ for a thermal distribution. Coefficients of the fitting formula are given for seven temperatures between $7 \times 10^8\,\mathrm{K}$ to $3.2 \times 10^{10}\,\mathrm{K}$, and the fractional errors are given for each temperature. Figure (3.5) compares our calculation with the fitting formula at $3.2 \times 10^{10}\,\mathrm{K}$. We find good agreement with their formula and reproduce their maximum error.

3.6.4 Nonthermal Electron Distribution

For a power-law distribution in the ultrarelativistic limit our absorption and emission coefficients agree with equations (3.59) and (3.60). Figures (3.6) and (3.7) show the emission and absorption coefficients for $p = 3$, $\gamma_{\min} = 1$ and $\gamma_{\max} = 1000$, and $\theta = 60$ deg. For $\gamma_{\min}^2 \ll \nu/\nu_c \ll \gamma_{\max}^2$ the relative errors in equations (3.59) and (3.60) approach 10^{-3}, while the errors diverge for smaller and larger ν/ν_c.

Our code can also handle an electron distribution with pitch-angle dependence. One example is the anisotropic nonthermal emission calculated in Fleishman & Melnikov [2003]. We reproduce their Fig. 1 in our Fig. (3.8). We do not have the

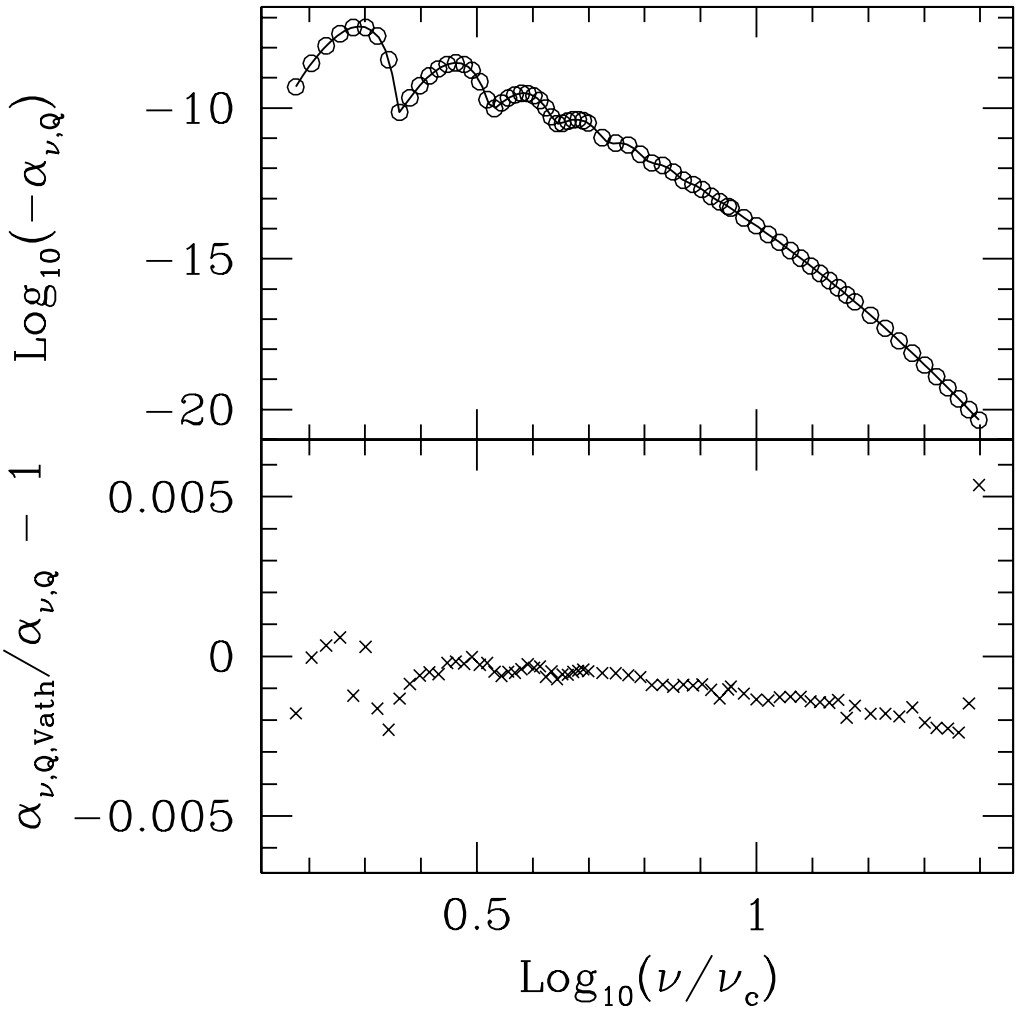

Figure 3.3 Upper panel: the absorption coefficients α_Q in cm^{-1} at $kT_e = 10.0$ keV, $\theta = 60$ deg. The solid lines are from `harmony`, whereas the circles are data from Table 4 in Väth & Chanmugam [1995]. Lower panel: relative difference of the the data from Väth & Chanmugam [1995] and `harmony`. There is a trend of deviation from the zero as ν increases. The trend is removed if `harmony` is run at $kT_e = 9.998$ keV. Similar trends are also seen in the plots of other absorption coefficients in Väth & Chanmugam [1995]. The maximum relative difference is 0.2% if the last two data points are dropped.

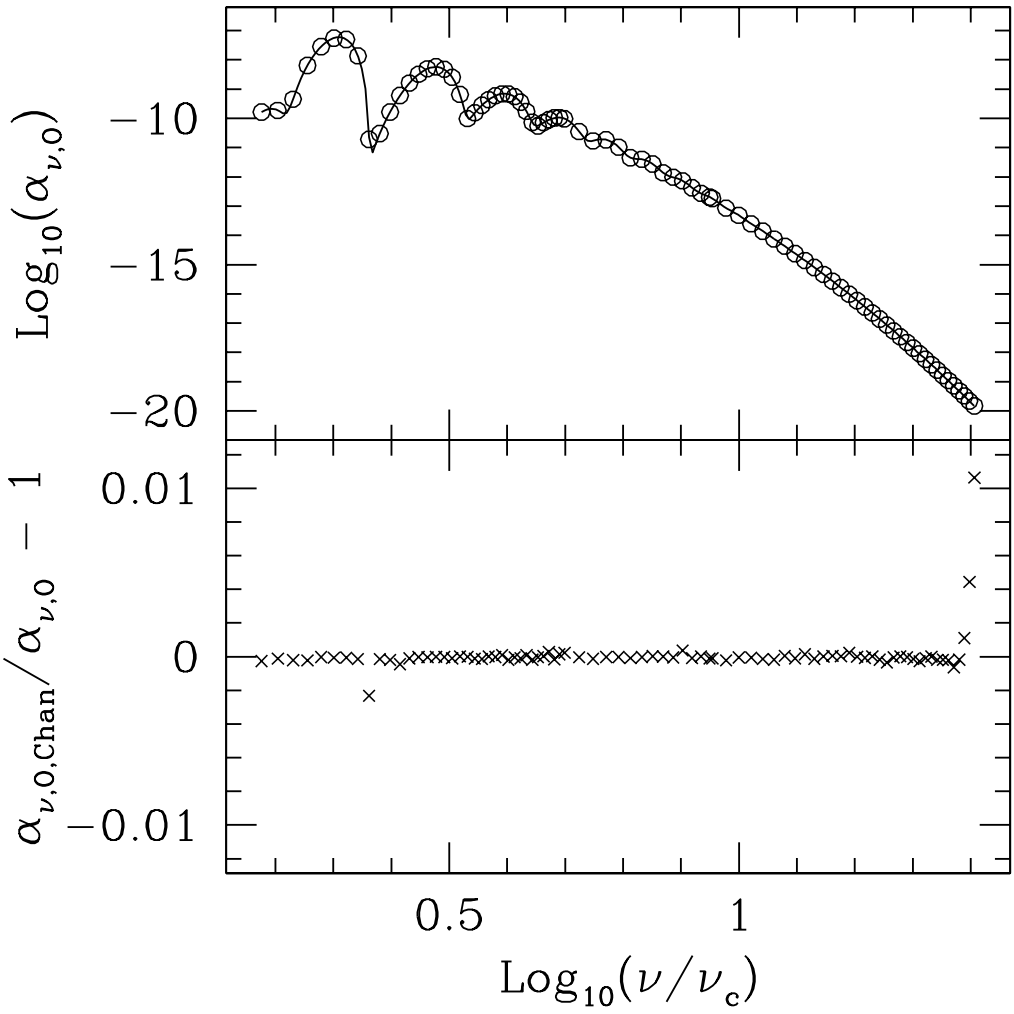

Figure 3.4 Upper panel: the absorption coefficients α_O in cm^{-1} at $kT_e = 10.0$ keV, $\theta = 60$ deg. The solid lines are from `harmony` with cold plasma T_X in equation (3.31), the circles are data from Table 6B in Chanmugam et al. [1989]. Lower panel: the crosses are relative differences of the the data from Chanmugam et al. [1989] and `harmony` with cold plasma T_X.

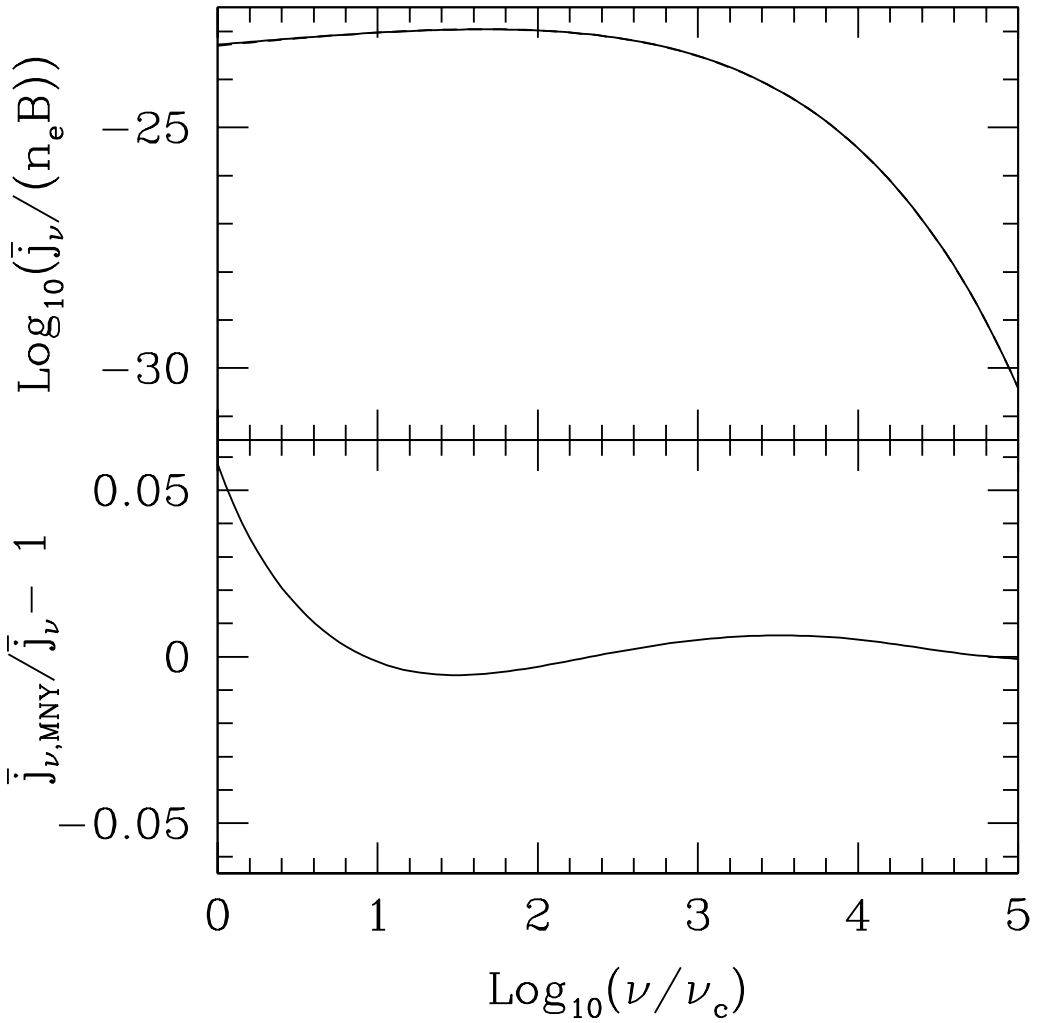

Figure 3.5 Upper panel: the angle-averaged thermal emissivity $\bar{j_\nu}/(n_e B)$ in cgs units, at $T = 3.2 \times 10^{10}\,\mathrm{K}$, for `harmony` (solid line) and fitting formula in Mahadevan, Narayan & Yi [1996] (dashed line). Lower panel: the relative difference of $\bar{j_\nu}$.

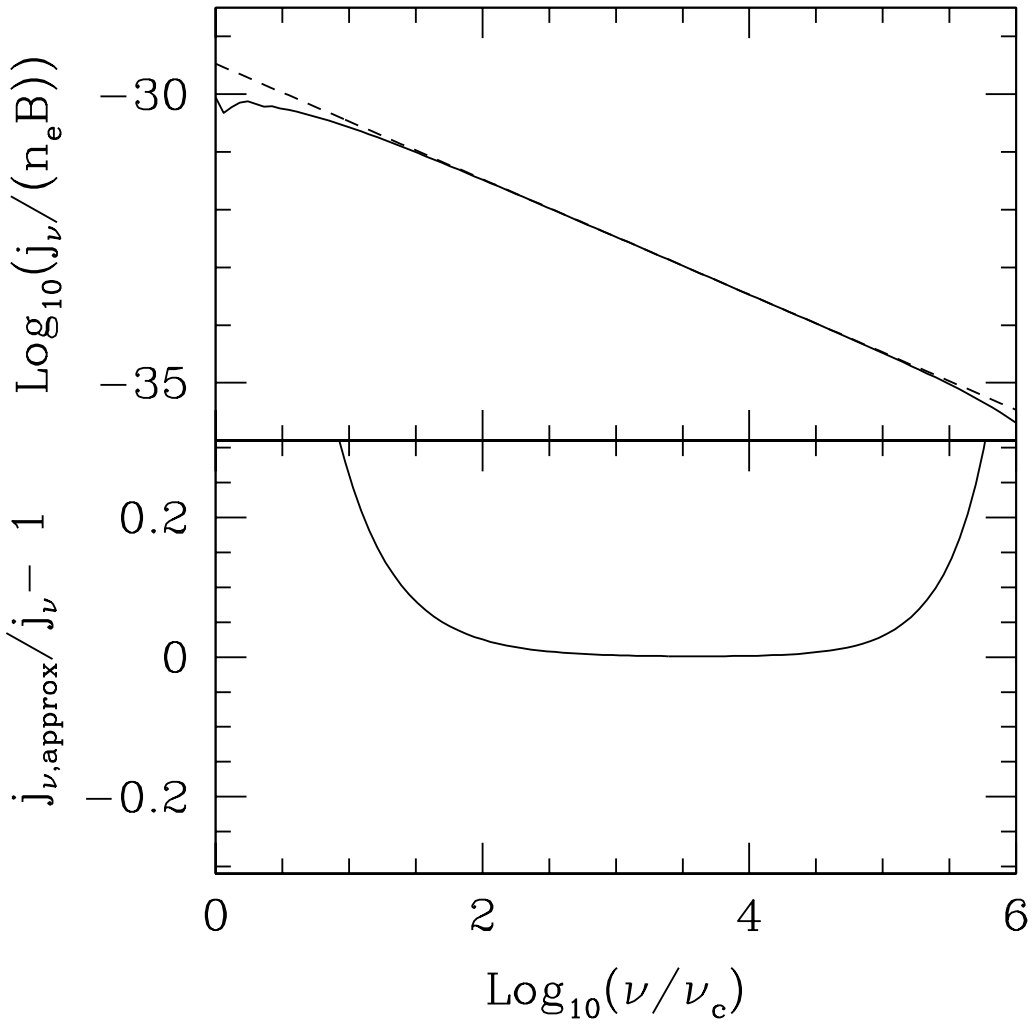

Figure 3.6 Upper panel: the emissivity $j_\nu/(n_e B)$, in cgs units, for $p = 3$, $\gamma_{\rm min} = 1$, $\gamma_{\rm max} = 1000$ and $\theta = 60$ deg. The solid line is the result of `harmony`, and dashed line is calculated by using equation (3.59). Lower panel: the relative difference of j_ν. The error is smallest for $\gamma_{\rm min}^2 \ll \nu/\nu_c \ll \gamma_{\rm max}^2$. At smaller and larger frequencies, the error diverges.

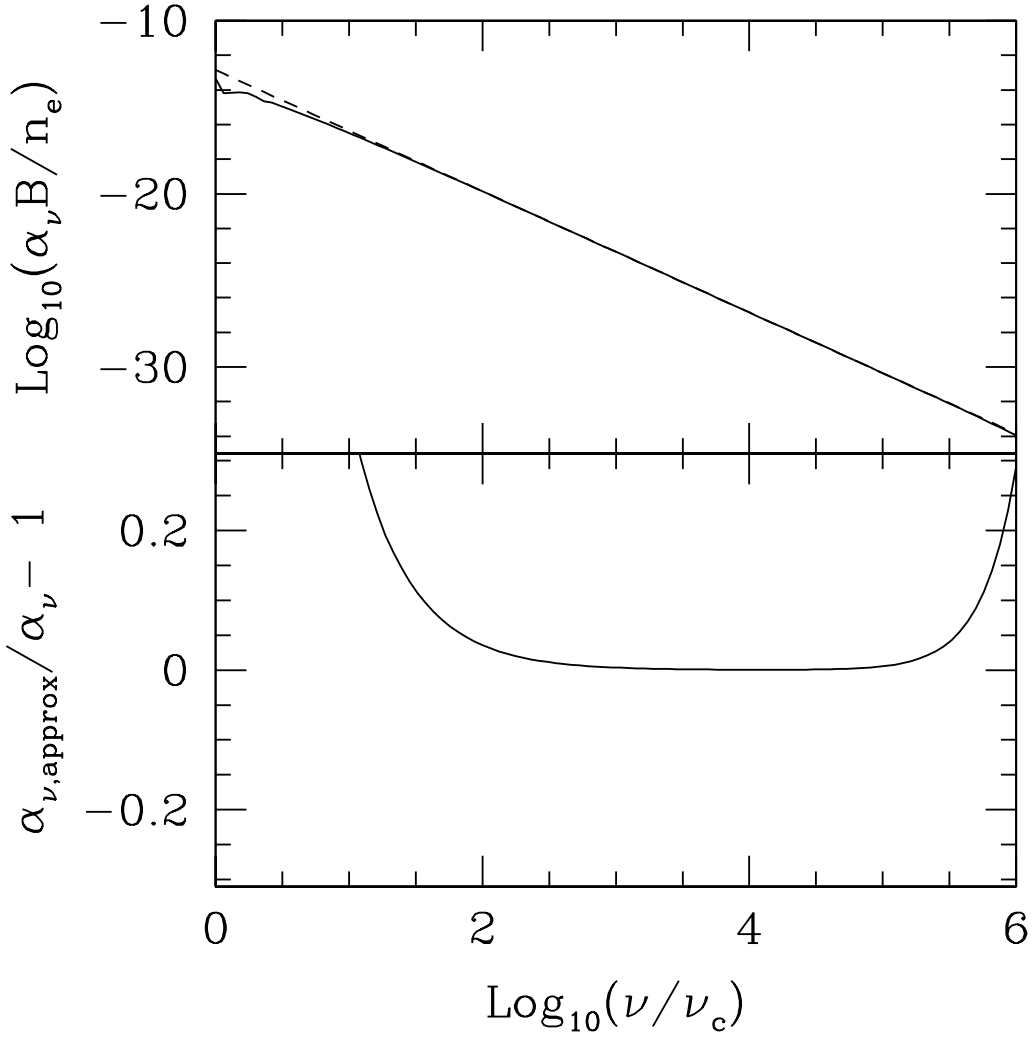

Figure 3.7 Upper panel: the absorption coefficient $\alpha_\nu B/n_e$, in cgs units, for $p = 3$, $\gamma_{\rm min} = 1$, $\gamma_{\rm max} = 1000$ and $\theta = 60$ deg. The solid line is the result of `harmony`, and dashed line is calculated by using equation (3.60). Lower panel: the relative difference of j_ν. The error is smallest for $\gamma_{\rm min}^2 \ll \nu/\nu_c \ll \gamma_{\rm max}^2$. At smaller and larger frequencies, the error diverges.

Fleishman & Melnikov data, so we cannot make a quantitative comparison, but a comparison by eye suggests that our results reproduce theirs quite well.

3.7 Approximate Equation

Motivated by the above discussion, and by the ultrarelativistic limit discussed above, we introduce the following approximate expression for the thermal MBS emissivity

$$j_\nu = n_e \frac{\sqrt{2}\pi e^2 \nu_s}{3K_2(1/\Theta_e)c} \left(X^{1/2} + 2^{11/12} X^{1/6}\right)^2 \exp\left(-X^{1/3}\right) \ . \tag{3.73}$$

Equation (3.73) combines Eq. (26) of Petrosian [1981] and Eq. (3.56). All three equations are shown in Figure (3.9), which shows that equation (3.73) is accurate over a much larger range of frequency.

Figures (3.10) and (3.11) are contour plots of the accuracy of equation (3.73) over a wide range of Θ_e and frequencies for $\theta = 30$ deg and $\theta = 80$ deg. These plots verify that our scheme accurately reproduces the high frequency limit given by equation (3.58), which coincides with equation (3.73). As a crude guide to the regime of validity of equation (3.73), we estimate that the error becomes of order unity for $\Theta_e \simeq (\nu/(\nu_c \sin\theta))^{-1/5}$.

3.8 Summary

We have described and verified an accurate, efficient scheme for evaluating magnetobremsstrahlung emission and absorption coefficients for polarized emission for an arbitrary electron distribution function. The relationship between the coefficients in the Stokes, Cartesian polarization, and mode polarization bases are given in §3.2.

For each coefficient we must evaluate a two-dimensional integral of the form (3.63). We use a publicly available numerical integration method. The integrand depends on Bessel functions of the first kind of high order n, so along the way we have developed an efficient method for evaluating high order Bessel functions. This method is described in Appendix A.2.

We have used the numerical results to evaluate the accuracy of several approximate analytic expressions that appear in the literature, and we have also verified earlier numerical work (e.g. Mahadevan, Narayan & Yi [1996], Petrosian [1981], Robinson & Melrose [1984]).

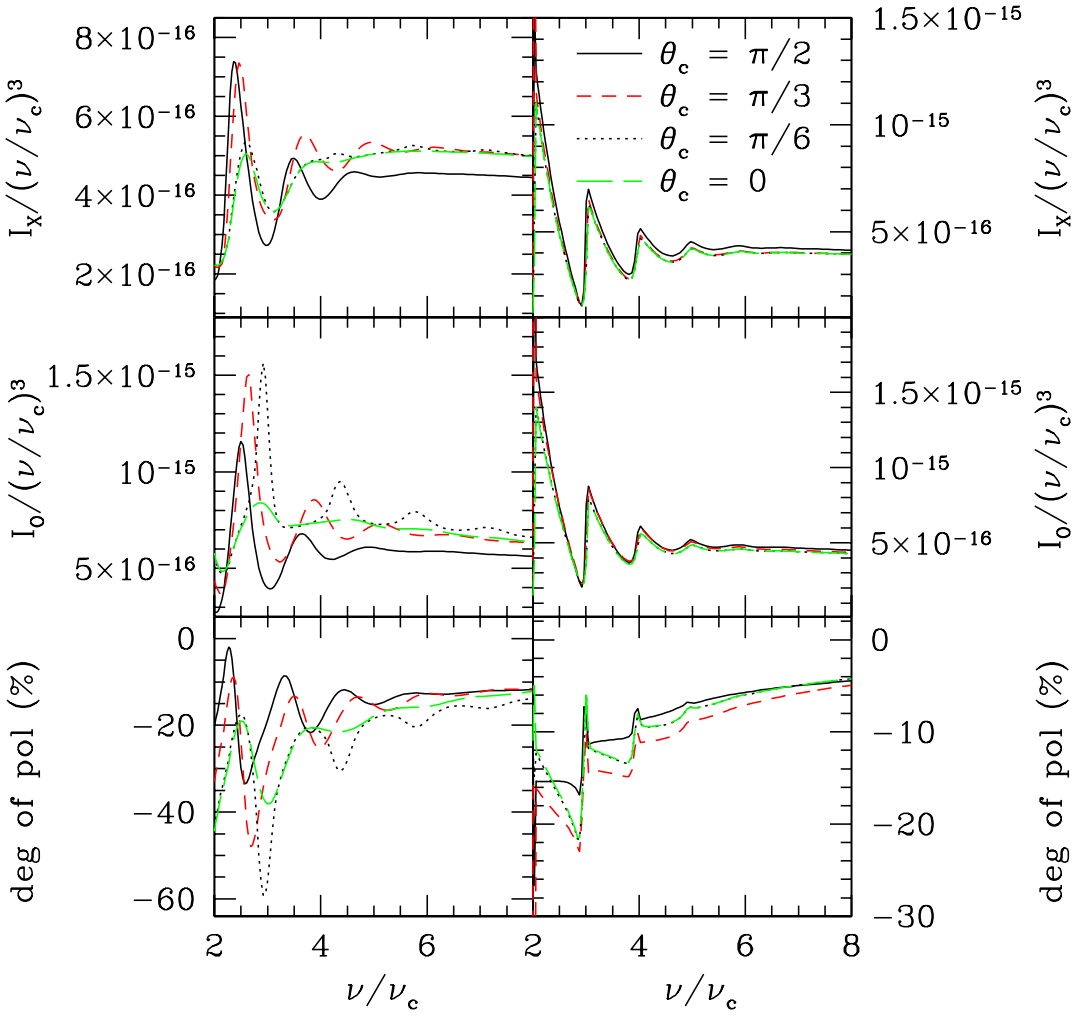

Figure 3.8 This figure is a reproduction of the Fig. 1 in Fleishman & Melnikov [2003]. $I_X/(\nu/\nu_c)^3$, $I_O(\nu/\nu_c)^3$ and degree of polarization are plotted as functions of frequency. Intensity I_A is defined as j_A/α_A, where A is O (ordinary mode) or X (extraordinary mode). Degree of polarization is defined as $(I_X - I_O)/(I_X + I_O)$. The panels on the left (right) are calculated with assumption that $\cos\theta = 0.8(0.2)$. In both cases, $\nu_p/\nu_c = 0.4$ and the exponent of the momentum power-law distribution is 5. Cold plasma approximation of T_X is used in the calculation using `harmony`.

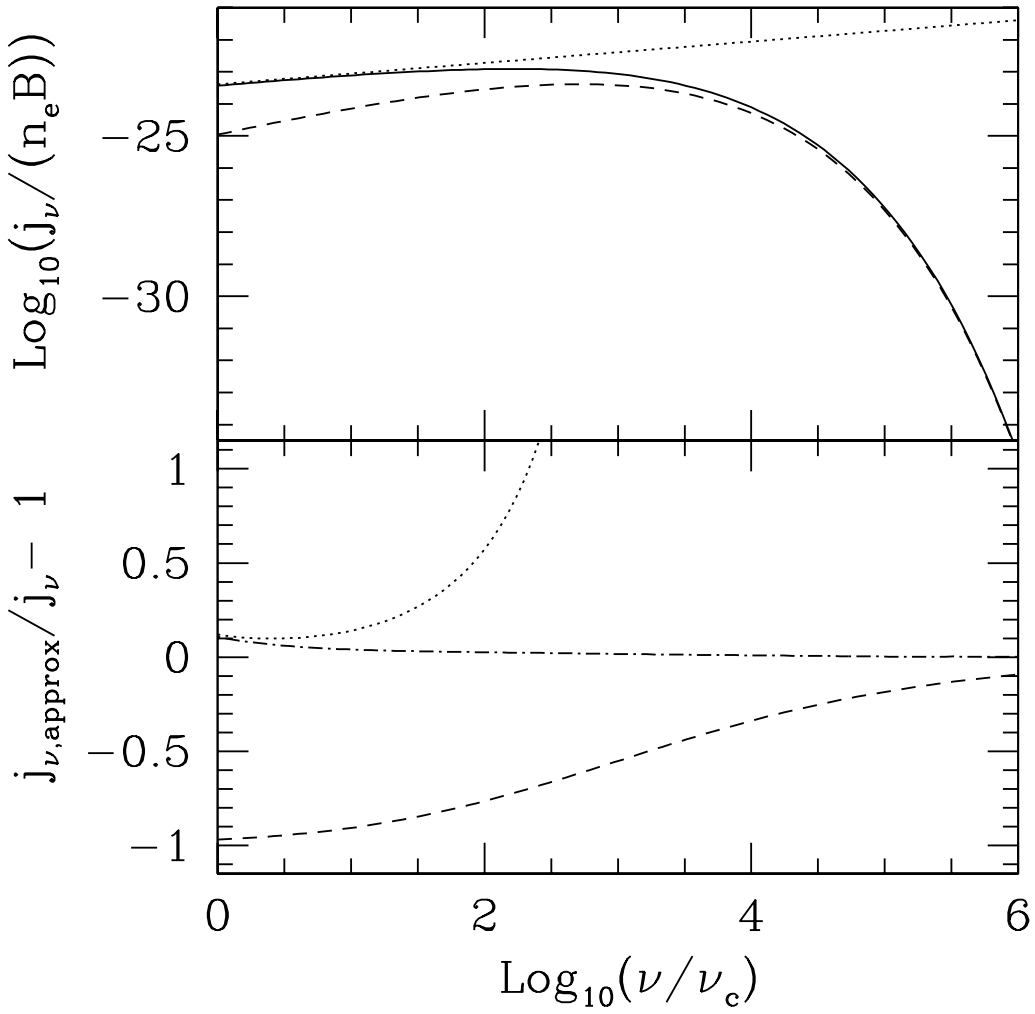

Figure 3.9 Upper panel: the emissivity $j_\nu/(n_e B)$, in cgs units, for $\Theta_e = 10, \theta = 60$ deg. The solid line is the result of `harmony`. The dashed line shows equation (26) of Petrosian [1981], the dotted line shows equation (3.56). The dotted-dashed line (which overlaps the solid line) shows the combined equation (3.73). Lower panel: the relative difference of the approximate equations.

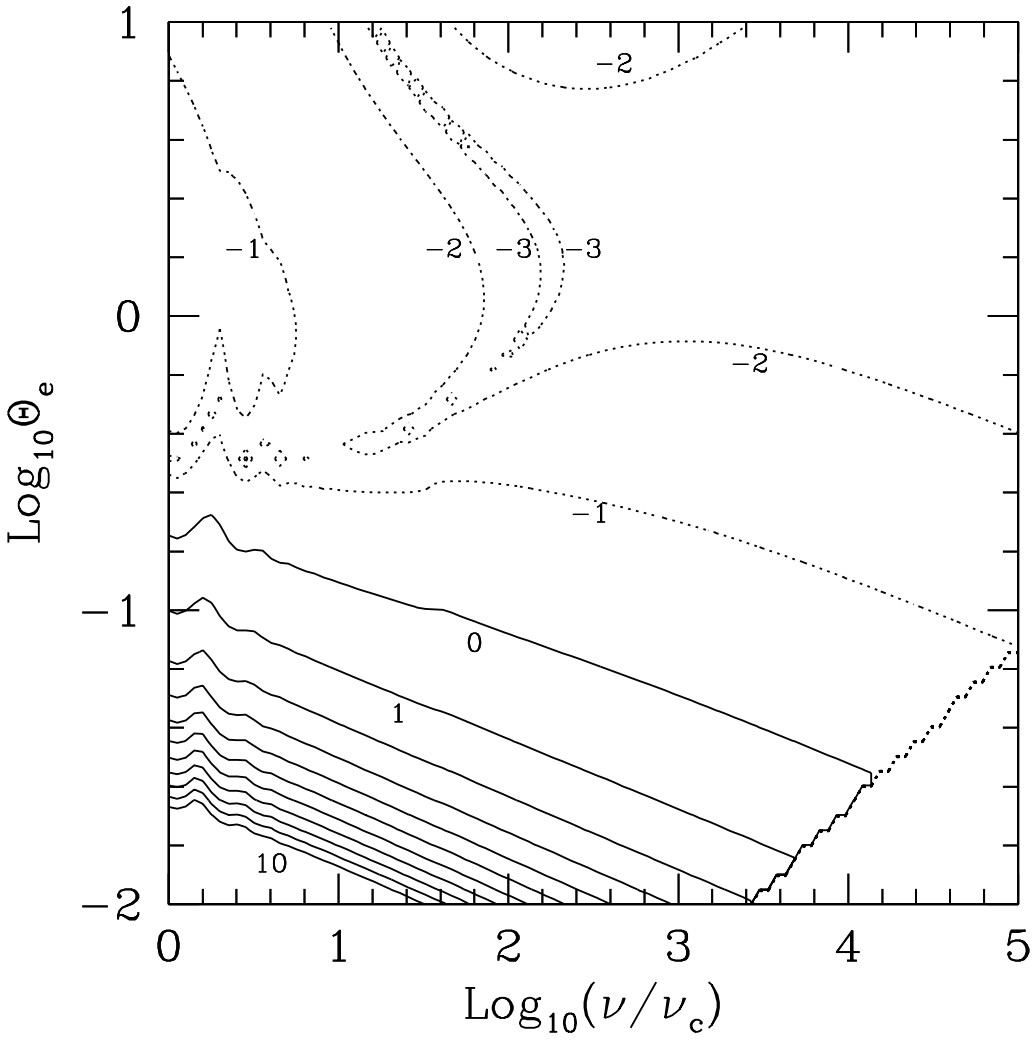

Figure 3.10 Logarithm of relative error of the approximated equation (3.73) of emissivity j_ν, at $\theta = 30$ deg. The dotted lines are contours of negative integers, and the solid lines are zero and positive integers up to 10. The lower-right corner is ignored since the emissivity is too low (cutoff $= 1 \times 10^{-250}$[cgs]).

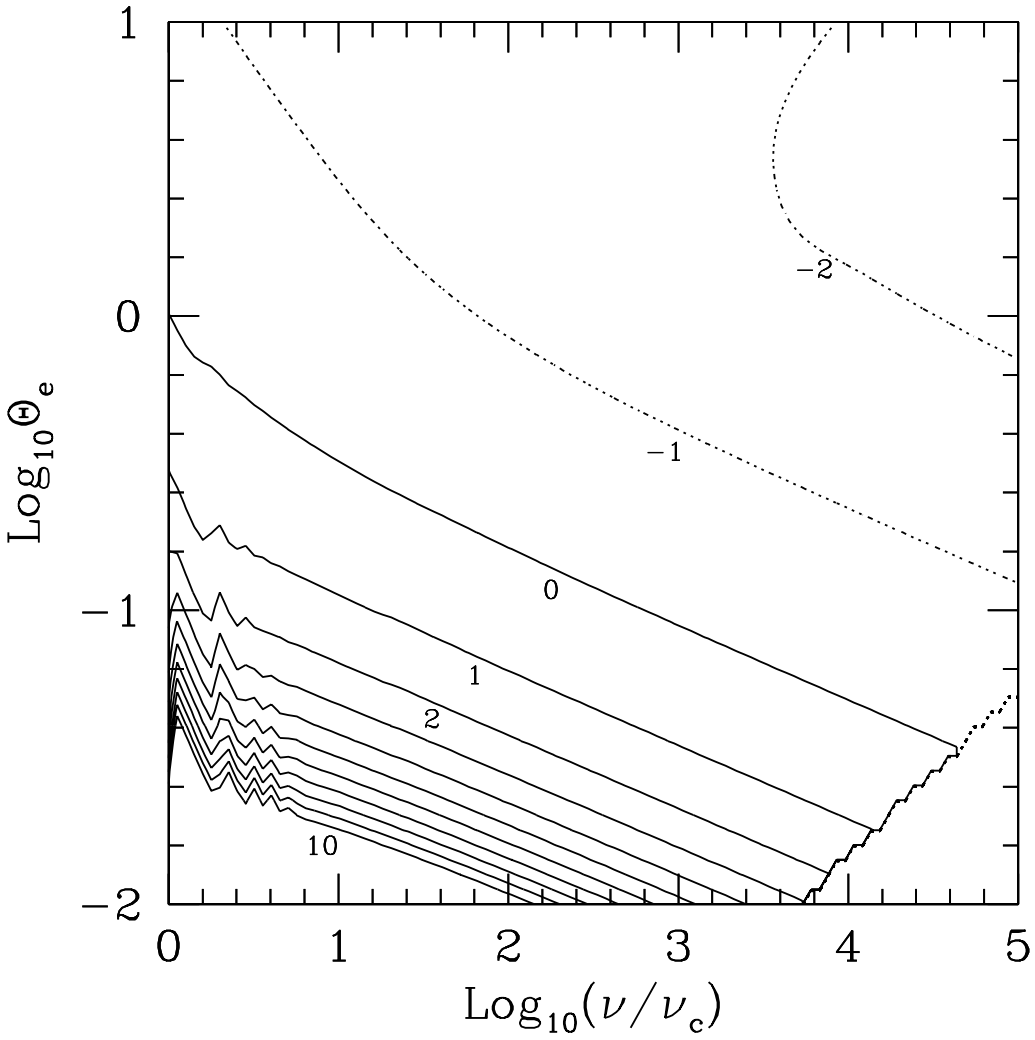

Figure 3.11 Logarithm of relative error of the approximated equation (3.73) of emissivity j_ν, at $\theta = 80$ deg. The dotted lines are contours of negative integers, and the solid lines are zero and positive integers up to 10. The lower-right corner is ignored since the emissivity is too low (cutoff $= 1 \times 10^{-250}$[cgs]).

Our code, called `harmony`, is available to the public from the web at `http://rainman.astro.illinois.edu/codelib`.

3.9 References

Abramowitz, M., & Stegun, I. A. 1970, Handbook of Mathematical Functions (New York: Wiley)

Bekefi, G. 1966, Radiation Processes in Plasmas (New York: Wiley)

Blumenthal, G. R. & Gould, R. J. 1970, Rev. of Mod. Phys., 42, 237

Brainerd, J. J. & Lambd, D. Q. 1987, ApJ, 313, 231

Broderick, A., & Blandford, R. 2004, MNRAS, 349, 994

Chanmugam, G., Barrett, P. E., Wu, K., & Courtney, M. W. 1989, ApJS, 71, 323

Chishtie, F. A., Valluri, S. R., Rao, K. M., Sikorski, D., & Williams, T. 2005, in Proceedings of the 19th Annual International Symposium on High Performance Computing Systems and Applications (HPCS 2005) (IEEE Computer Society)

Chishtie, F. A., Rao, K. M., Kotsireas, I. S., & Valluri, S. R. 2008, Inter. J. Mod. Phys. D, 17, 1197

Crusius, A., & Schlickeiser, R. 1986, A&A, 164, L16

Crusius, A., & Schlickeiser, R. 1988, A&A, 196, 327

Dulk, G. A. 1985, ARAA, 23, 169

Fleishman, G. D., & Melnikov, V. F. 2003, ApJ, 584, 1071

Galassi, M., et al. 2006 GNU Scientific Library Reference Manual (2nd ed.), `http://www.gnu.org/software/gsl/`

Ginzburg, V. L. 1970, The Propagation of Electromagnetic Waves in Plasmas (2nd ed.; Oxford: Pergamon)

Kawabata, K. 1964, PASJ, 16, 30

Leung, P. K., Gammie, C. F., & Noble, S. C. 2009, ApJ, submitted

Mahadevan, R., Narayan, R., & Yi, I. 1996, ApJ, 465, 327

Marcowith, A., & Malzac, J. 2003, A&A, 409, 9

Melia, F. 1994, ApJ, 426, 577

Melrose, D. B. 1989, Instabilities in Space and Laboratory Plasmas (Cambridge: Cambridge)

Melrose, D. B., & McPhedran, R. C. 1991, Electromagnetic Processes in Dispersive Media (Cambridge: Cambridge)

Meggitt, S. M. A., & Wickramasinghe, D. T. 1982, MNRAS, 198, 71

The NAG C Library Mark 8, Numerical Algorithms Group, `http://www.nag.co.uk/`

Noble, S. C., Leung, P. K., Gammie, C. F., & Book, L. G., 2007, Class. Quant. Grav., 24, 259

Pacholczyk, A. G. 1970, Radio Astrophysics: Nonthermal Processes in Galactic and Extragalactic Sources (San Francisco: Freeman)

Petrosian, V. 1981, ApJ, 251, 727

Petrosian, V., & McTiernan, J. M. 1983, Phys. Fluids, 26, 3028

Press, W. H., Teukolsky, S. A., Vetterling, W. T., & Flannery, B. P. 1992, Numerical Recipes in C: The Art of Scientific Computing (Cambridge: Cambridge)

Robinson, P. A., & Melrose, D. B. 1984, Aust. J. Phys., 37, 675

Rybicki, G. B., & Lightman, A. P. 1979, Radiative Processes in Astrophysics (New York: Wiley)

Schlickeiser, R., & Lerche, I. 2007, A&A, 476, 1

Stix, T. H. 1992, Waves in Plasmas (New York: AIP)

Takahara, F., & Tsuruta, S. 1982, Prog. Theor. Phys., 67, 485

Väth, H. M., & Chanmugam, G. 1995, ApJS, 98, 295

Wardzinski, G., & Zdziarski, A. 2000, MNRAS, 314, 183

Westfold, K. C. 1959, ApJ, 130, 241

Wolfe, B., & Melia, F. 2006, ApJ, 637, 313

Chapter 4

Effects of Nonthermal Electrons on Spectra of Accretion Flows onto Supermassive Black Hole

4.1 Introduction

The observations of S stars near to the Galactic center [Eisenhauer et al., 2005, Ghez et al., 2003, Schödel et al., 2002] have provided strong evidence that the Galactic center harbors a supermassive black hole of $\sim 4 \times 10^6 M_\odot$. The radio source Sgr A* at the site is generally believed to be created from accretion activity onto the black hole. Due to the subluminous nature of the source, efforts have been focused on comparing simplified models of radiatively inefficient accretion flow (RIAF) with the observation. Only recently are there numerical simulations that include more complex flow structure and additional physics. The correct model needs to account for the observed properties in the broadband spectrum.[1]

One of the observed properties is the spectral index in νL_ν during near infrared (NIR) flaring event. Weak NIR flares appear to have negative spectral slope [Ghez et al., 2005, Krabbe et al., 2006], which is predicted by calculations of quiescent state with only thermal electrons (RIAF models: Narayan, Yi & Mahadevan [1995], Özel, Psaltis & Narayan [2000]; computer simulations: Dexter et al. [2010], Mościbrodzka, et al. [2009]). However, Hornstein et al. [2007] suggest that the spectral slope of spectral energy distribution (SED) is 0.4 ± 0.2 for strong NIR flares (between 3.8 and 1.6 μm), which is difficult to explain by thermal synchrotron emission or Compton scattering [Dodds-Eden et al., 2009]. It is always possible to construct a jet model with suitable temperature and density to account for the positive spectral slope at NIR, but no self-consistent computer simulation has produced such a feature.

If the simulated disk model is to believed, one then has to modify the emission mechanism to explain the positive spectral slope in NIR flares. One possible way of achieving this is by considering inverse Compton scattering of thermal synchrotron photons at sub-millimeter (sub-mm) bump [Ohsuga, Kato & Mineshige, 2005]. Nev-

[1]This work will be submitted to ApJ [Leung et al., 2010]. Reproduction for this dissertation is authorized by the copyright holder.

ertheless, inverse Compton models with only thermal distribution require inner-region density which is several orders of magnitude higher than the inferred value of Sgr A* [Dodds-Eden et al., 2009]. Another possibility is model with self-Compton scattering of the NIR flaring photons, but this requires unrealistically strong magnetic field strength in the accretion flow [Dodds-Eden et al., 2009]. For Sgr A*, bremsstrahlung does not produce enough emission to explain the NIR flares. Then, a remaining possibility is model with nonthermal synchrotron emission, which we will consider in this chapter.

It is natural to produce a positive spectral slope in the NIR bands by adding nonthermal electrons, which are likely to exist in flaring events because electrons may not have enough time to thermalize. In fact, transient events such as shocks and reconnection are known to produce power-law electrons, both according to theory and observation. Notice that the sub-mm peak of Sgr A* can be explained very well with only thermal synchrotron emission from inner regions [2] of the accretion flow [e.g. Mościbrodzka, et al., 2009, Narayan, Yi & Mahadevan, 1995, Özel, Psaltis & Narayan, 2000]. However, the quiescent fluxes are only constrained at the low-frequency side of the sub-mm peak. This allows the freedom of adding power-law component to the distribution that only contributes to emission at $\nu > 10^{12}$ Hz.

In this chapter, we discuss spectra of accretion disk simulations with both thermal and power-law electrons, with application to Sgr A*. In §2 we briefly describe the accretion disk simulation. In §3 we review the commonly used electron distribution functions, and discuss details of implementing them in the calculation. In §4 we give expressions for the emissivity and absorptivity for the distribution functions. We also discuss the region of validity of the expressions. With the models of electron distribution, and the equations of emission and absorption coefficient, the next ingredient is a recipe for radiative transfer, which will be described in §5. In §6 we test our code and demonstrate that our implementation is correct. In §7 we discuss the main result and compare our calculation with previous works. In §8 we give a short summary.

4.2 Accretion disk simulation

We assume a geometrically thick, optically thin, collisionless accreting flow onto a spinning supermassive black hole with mass M. The spin of the black hole is parametrized by $a_* = Jc/(GM^2)$, where J is the spin angular momentum. In disk

[2] Up to around tens of Schwarzschild radii, depending on the details of the disk model.

simulation, we assume that both ions and electrons have thermal distributions [3]. The ion-to-electron temperature ratio T_i/T_e is kept constant in the disk. $\Gamma-$law equation of state is used, with $\Gamma = 13/9$.

Numerical simulations are performed using the 2D version of the general relativistic magnetohydrodynamic (GRMHD) code HARM [Gammie, McKinnney, & Tóth, 2003]. The code solves the GRMHD equations using a conservative shock-capturing scheme. The $\nabla \cdot \vec{B} = 0$ condition is maintained by constrained transport. We assume axisymmetry in the simulation, therefore axis of the black hole is aligned with that of the accretion disk. The simulation is started with a torus defined in Fishbone & Moncrief [1976], with a weak poloidal concentric magnetic field. The inner boundary of the torus is at $6GM/c^2$, and density is maximum at $12GM/c^2$.

We use modified Kerr-Schild coordinates in the simulation. The inner boundary is set to $0.98(1+\sqrt{1-a_*^2})$, which means the code follows the flow until it passes the event horizon. The outer boundary is set to 40 $GM/c^2 = 1.8$ AU. Outflow boundary conditions are used at both boundaries. Polar boundary conditions are used at the two poles in θ. The resolution of the simulation is 256×256, with denser grids near to the black hole and on the plane of accreting flow. The simulation ends at $2000GM/c^3 \simeq 12$ hr.

There are 3 parameters in our disk model, namely black hole spin a_*, ion-to-electron ratio T_i/T_e, and observation orientation angle i. Mościbrodzka, et al. [2009] perform a parameter survey and conclude that the best-bet model has $a_* = 0.94$ and $T_i/T_e = 3$, and is observed at $i = 80°$ (edge on).

4.3 Electron distribution

Two of the commonly-used electron distribution functions are thermal and power-law distributions. In this section, we review the relative equations and define the parameters in the calculation.

4.3.1 Thermal distribution

The relativistic thermal distribution is

$$\frac{dn_e}{d\gamma} \equiv n_{\rm th}(\gamma) = \frac{N_{\rm th}\gamma^2\beta\exp(-\gamma/\Theta_e)}{\Theta_e K_2(1/\Theta_e)} \ , \tag{4.1}$$

[3] It may seem to contradict with our inclusion of nonthermal component in the radiative transfer calculation. However, we limit the energy fraction of power-law component at low level $< 1\%$, therefore the error introduced by this discrepancy is small.

where the dimensionless electron temperature is defined as

$$\Theta_e \equiv \frac{k_{\rm B} T_e}{m_e c^2} \ , \tag{4.2}$$

$N_{\rm th}$ is the thermal electron number density, γ is the electron Lorentz factor, β is the electron speed in units of light speed, and K_2 is the modified Bessel function of the second kind.

The thermal energy density is [Özel, Psaltis & Narayan [2000, Eq. (5)]; Chandrasekhar [1957, Ch. X, Eq. (235)]]

$$u_{\rm th} = a(\Theta_e) N_{\rm th} m_e c^2 \Theta_e \ , \tag{4.3}$$

where

$$a(\Theta_e) \equiv \frac{1}{\Theta_e} \left[\frac{3K_3(1/\Theta_e) + K_1(1/\Theta_e)}{4K_2(1/\Theta_e)} - 1 \right] \ . \tag{4.4}$$

Two simplified expressions for $a(\Theta_e)$ are [Gammie & Popham, 1998]

$$a(\Theta_e) = \frac{6 + 15\Theta_e}{4 + 5\Theta_e} \qquad (\text{max. rel. err.} < 2\%) \tag{4.5}$$

and

$$a(\Theta_e) = \frac{12 + 45\Theta_e + 45\Theta_e^2}{8 + 20\Theta_e + 15\Theta_e^2} \qquad (\text{max. rel. err.} < 7 \times 10^{-4}) \ . \tag{4.6}$$

4.3.2 Power-law distribution

There is a lot of freedom in defining a nonthermal distribution. To reduce the number of parameters, we only consider two cases, namely, a power-law distribution with a single power-law index (simple power-law), and the power-law distribution with a cooling break ("broken" power-law). Both distributions are assumed isotropic. We define η as the ratio of the energy in the nonthermal population to the energy in the thermal population:

$$u_{\rm pl} = \eta u_{\rm th} \ , \tag{4.7}$$

where $u_{\rm pl}$ is the power-law energy density, and $u_{\rm th}$ is defined in equation (4.4).

Simple power-law distribution

The simple power-law distribution is

$$n_{\rm pl}(\gamma) = C_{\rm pl,s} \gamma^{-p} \qquad \text{for } \gamma_{\rm min} \le \gamma \le \gamma_{\rm max} \ , \tag{4.8}$$

where the normalization constant is

$$C_{\rm pl,s} = N_{\rm pl} \frac{p-1}{\gamma_{\rm min}^{1-p} - \gamma_{\rm max}^{1-p}} \ , \tag{4.9}$$

$N_{\rm pl}$ is the power-law electron number density and p is the power-law index. Özel, Psaltis & Narayan [2000] consider the special case [4] that $\gamma_{\rm min} = 1$ and $\gamma_{\rm max} = \infty$, so the normalization constant becomes $C_{\rm pl,s} = N_{\rm pl}(p-1)$, consistent with equation (4) in Özel, Psaltis & Narayan [2000].

The power-law energy density is

$$\begin{aligned} u_{\rm pl} &= \int_{\gamma_{\rm min}}^{\gamma_{\rm max}} d\gamma \, n_{\rm pl}(\gamma) \, \gamma m_e c^2 \\ &= \int_{\gamma_{\rm min}}^{\gamma_{\rm max}} d\gamma \, C_{\rm pl,s} \gamma^{-p} \, \gamma m_e c^2 \\ &= C_{\rm pl,s} \, m_e c^2 \, \frac{\gamma_{\rm min}^{2-p} - \gamma_{\rm max}^{2-p}}{p-2} \qquad (4.10) \\ &= N_{\rm pl} \, m_e c^2 \, \frac{p-1}{p-2} \, \frac{\gamma_{\rm min}^{2-p} - \gamma_{\rm max}^{2-p}}{\gamma_{\rm min}^{1-p} - \gamma_{\rm max}^{1-p}} \ . \qquad (4.11) \end{aligned}$$

By equations (4.3), (4.7) and (4.11), the number density of the simple power-law distribution is

$$N_{\rm pl} = N_{\rm th} \eta \, a(\Theta_e) \Theta_e \, \frac{p-2}{p-1} \, \frac{\gamma_{\rm min}^{1-p} - \gamma_{\rm max}^{1-p}}{\gamma_{\rm min}^{2-p} - \gamma_{\rm max}^{2-p}} \ . \tag{4.12}$$

In the case that $\gamma_{\rm min} = 1$, $\gamma_{\rm max} = \infty$ and $p > 2$, equation (4.12) is $N_{\rm pl} = N_{\rm th} \eta \, a(\Theta_e) \Theta_e$ $(p-2)/(p-1)$, which has an extra factor of $1/(p-1)$ compared to equation (8) in Özel, Psaltis & Narayan [2000]. The seeming discrepancy is due to a difference in the definition of $u_{\rm pl}$. We choose to define $u_{\rm pl}$ as the total energy density in order to simply the equation, whereas Özel, Psaltis & Narayan [2000] exclude the rest mass energy from the equation

Broken power-law distribution

With particle injection and synchrotron cooling, the evolution of the distribution function is governed by the Boltzmann equation [Kardashev, 1962]

$$\frac{\partial n(\gamma, t)}{\partial t} + \frac{\partial}{\partial \gamma} \left[\frac{d\gamma}{dt} \, n(\gamma, t) \right] = Q(\gamma, t) - S(\gamma, t) \ , \tag{4.13}$$

[4] In Özel, Psaltis & Narayan [2000], §3.2, they impose a maximum Lorentz factor $\gamma_{\rm max} \sim 10^3$ for $p < 3$ and when $\eta > 0.05\%$.

where $d\gamma/dt \propto \gamma^2$ for synchrotron emission, $Q(\gamma, t)$ is the electron energy injection rate which is proportional to the injected electron distribution, and $S(\gamma, t) \equiv (\vec{v} \cdot \nabla)n$ is the sink term. Assume that the injection distribution $\propto \gamma^{-p}$, and the cooling distribution $\propto \gamma^{-p_c}$. The cooling power-law index is found by assuming an equilibrium between the injection and cooling, which leads to

$$\begin{aligned} & \frac{\partial}{\partial\gamma}(\gamma^2\gamma^{-p_c}) \propto \gamma^{-p} \\ \Longrightarrow \quad & \gamma^2\gamma^{-p_c} \propto \gamma^{-p+1} + \text{constant} \\ \Longrightarrow \quad & \gamma^{-p_c} \propto \gamma^{-p-1} - \gamma_{\rm max}^{-p+1}\gamma^{-2} \,, \end{aligned} \tag{4.14}$$

where the constant is fixed by the fact that the cooling distribution goes to 0 at $\gamma = \gamma_{\rm max}$. For $p > 1$, first term on the RHS dominates and $p_c = p + 1$; for $p < 1$, second term dominates and $p_c = 2$. The latter situation is unlikely in the system that we are interested in, therefore we focus on the $p > 1$ case.

On the other hand, if cooling is balanced by the sink, advection dominates and the electrons are not cooled. That means the power-law index remains p. To calculate the "cooling break" Lorentz factor $\gamma_{\rm c}$ which separates the original distribution and the cooling distribution, one needs an expression for the sink term. A simplest expression is $S = n/t_{\rm acc}$, where $t_{\rm acc}$ is the accreting time scale. Then by assuming that n is a slow-changing function of time, the equilibrium between the sink and cooling leads to

$$\frac{\partial}{\partial\gamma}\left[\frac{d\gamma}{dt}\, n(\gamma)\right] = \frac{n(\gamma)}{t_{\rm acc}} \tag{4.15}$$

$$\Longrightarrow \quad t_{\rm cool} \equiv \frac{1}{\gamma}\frac{d\gamma}{dt} = \frac{3}{4}\frac{8\pi m_e c}{\sigma_{\rm T}\gamma_{\rm c}\beta^2 B^2} = t_{\rm acc} \equiv \frac{R}{|v_r|} \,, \tag{4.16}$$

where $\sigma_{\rm T}$ is the Thomson cross section, B is the magnetic field strength, R is the radius from the central object, and v_r is the radial accreting velocity. $\gamma_{\rm c}$ can be calculated from equation (4.16) once details of the accretion flow are specified (either by a RIAF model, or computer simulation),

With all these information, we are ready to define the broken power-law distribution as

$$n_{\rm pl}(\gamma) = \begin{cases} C_{\rm pl,b}\gamma^{-p} & \text{for } \gamma_{\rm min} \le \gamma \le \gamma_{\rm c} \\ C_{\rm pl,b}\gamma_{\rm c}\gamma^{-p-1} & \text{for } \gamma_{\rm c} \le \gamma \le \gamma_{\rm max}, \end{cases} \tag{4.17}$$

where $\gamma_{\rm min}$, $\gamma_{\rm max}$ and $\gamma_{\rm c}$ are the minimum, maximum and "cooling break" Lorentz

factors respectively, and the normalization constants are

$$C_{\rm pl,b} = N_{\rm pl}\left(\gamma_{\rm min}^{1-p} - \frac{1}{p}\gamma_{\rm c}^{1-p} - \frac{p-1}{p}\gamma_{\rm c}\gamma_{\rm max}^{-p}\right)^{-1}(p-1). \tag{4.18}$$

The power-law number density is fixed by the equation $u_{\rm pl} = \eta u_{\rm th}$, where the power-law energy density is

$$\begin{aligned} u_{\rm pl} &= \int_{\gamma_{\rm min}}^{\gamma_{\rm max}} d\gamma\, n_{\rm pl}(\gamma)\,(\gamma-1)m_e c^2 \\ &= C_{\rm pl,b} m_e c^2 \left[\frac{\gamma_{\rm min}^{2-p} - \gamma_{\rm c}^{2-p}}{p-2} + \gamma_{\rm c}\frac{\gamma_{\rm c}^{1-p} - \gamma_{\rm max}^{1-p}}{p-1}\right]. \end{aligned} \tag{4.19}$$

Therefore, the power-law number density is

$$\begin{aligned} N_{\rm pl} &= N_{\rm th}\eta a(\Theta_e)\Theta_e \frac{1}{p-1}\left(\gamma_{\rm min}^{1-p} - \frac{1}{p}\gamma_{\rm c}^{1-p} - \frac{p-1}{p}\gamma_{\rm c}\gamma_{\rm max}^{-p}\right) \\ &\quad \times \left[\frac{\gamma_{\rm min}^{2-p} - \gamma_{\rm c}^{2-p}}{p-2} + \gamma_{\rm c}\frac{\gamma_{\rm c}^{1-p} - \gamma_{\rm max}^{1-p}}{p-1}\right]^{-1}, \end{aligned} \tag{4.20}$$

which reduces to equation (4.12) if $\gamma_{\rm c} = \gamma_{\rm max}$.

Parameters in the power-law distributions

The power-law distribution is known to have many different breaks that correspond to different physics [Kardashev, 1962], and each segment of the distribution has a different power-law index. Besides, in more realistic situation, the power-law parameters likely vary in space. There is also time variation due to turbulence and shocks in the disk. There are also other possibilities (e.g. injection, anisotropy) which further complicate the situation. We therefore limit our discussion to two minimal power-law distribution models.

Here we summarize the parameters of the two distributions. For simple power-law, the parameters are power-law energy fraction η, index p, minimum gamma factor $\gamma_{\rm min}$, maximum gamma factor $\gamma_{\rm max}$. For broken power-law, in addition to the previous four parameters, there is also a gamma factor at cooling break $\gamma_{\rm c}$.

Power-law number density is set by using η in our calculation. We also choose to fix the total energy in all electrons according to the disk model, instead of fixing the thermal electron number density, as in Özel, Psaltis & Narayan [2000].

Joining thermal and power-law distributions

There are two scenarios about the sources of the power-law electrons. First case is that the power-law electrons are independent from the thermal electrons. Then both $\gamma_{\rm min}$ and $\gamma_{\rm max}$ are free parameters of the model, and normalization constant (and thus $N_{\rm pl}$) is fixed by $u_{\rm pl} = \eta u_{\rm th}$. Second case is that the power-law electrons are accelerated from the thermal electrons. Then one needs a recipe to join the thermal and power-law distributions. In this section we discuss the details of the second scenario.

The simplest way of fixing the parameters is to assume that the power-law distribution starts at the thermal distribution. Then $\gamma_{\rm min}$ and the normalization constant are found by solving $u_{\rm pl} = \eta u_{\rm th}$ and $n_{\rm th}(\gamma_{\rm min}) = n_{\rm pl}(\gamma_{\rm min})$ simultaneously, and $\gamma_{\rm max}$ is treated as a free parameter. Generally a root finder is needed to solve the equations. Figure (4.1) shows an example of joining a broken power-law with a thermal distribution, with $\gamma_{\rm min}$ found by using GSL root finder [Galassi et al., 2006].

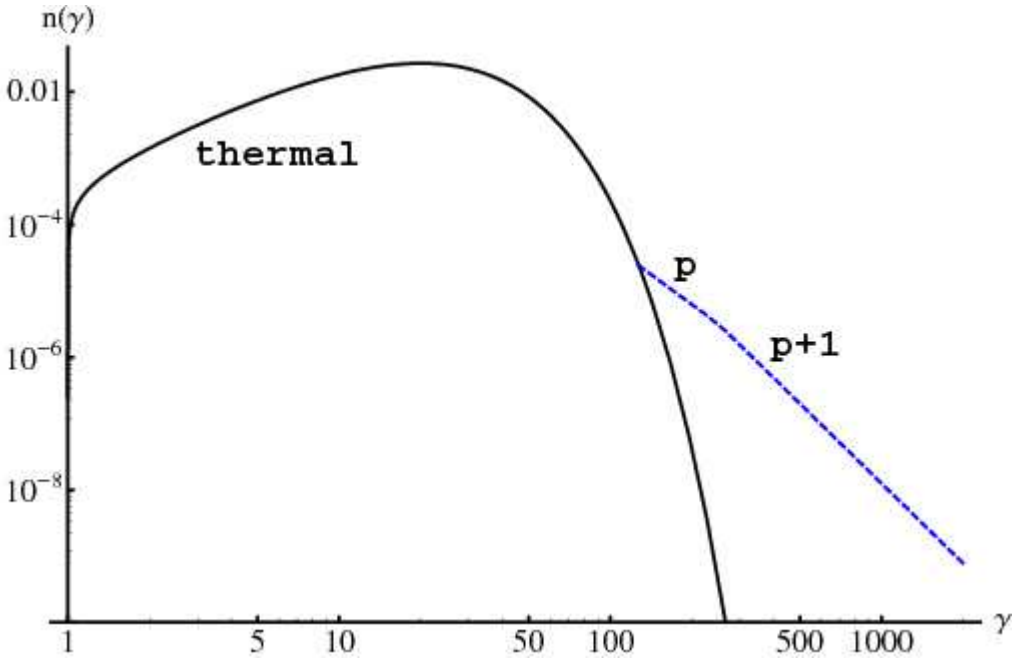

Figure 4.1 Example of joining a broken power-law distribution (dashed line) with a thermal distribution (solid line). The model has $\Theta_e = 10$, $p = 3$, $\eta = 0.01$, $\gamma_{\rm c} = 250$, $\gamma_{\rm max} = \infty$.

If one simply defines total electron density $n_e = n_{\rm th} + n_{\rm pl}$, as in Yuan, Quataert & Narayan [2003], there would be a second peak at $\gamma = \gamma_{\rm min}$ (or $\gamma_{\rm max}$ if $p < 2$) in the distribution function. This could lead to instability in the plasma [5]. In our calcula-

[5] "Bump-on-tail" instability [see, e.g, Stix, 1992, p. 455].

tion, the power-law energy fraction is kept to a low value, so the joined distribution that we use is not very different from the smooth-out distribution. That allows us to simplify the calculation a lot. If one wants to avoid the instability, one can define the nonthermal component as

$$n_{\rm nth}(\gamma) = n_{\rm pl}(\gamma) - n_{\rm th}(\gamma) \ . \tag{4.21}$$

However, with such a definition, the normalization and thus the nonthermal electron number density $N_{\rm nth}$ do not have analytic forms. Also this choice will not make much difference to the spectrum.

To find a closed form for $N_{\rm pl}$, one can replace equation (4.1) by the ultrarelativistic thermal distribution

$$n_{\rm th}^{\rm (ultra)}(\gamma) = \frac{N_{\rm th}\gamma^2 \exp[(1-\gamma)/\Theta_e]}{\Theta_e(1+2\Theta_e+2\Theta_e^2)} \ . \tag{4.22}$$

The nonthermal distribution

$$n_{\rm nth}(\gamma) = n_{\rm pl}(\gamma) - n_{\rm th}^{\rm (ultra)}(\gamma) \tag{4.23}$$

can be integrated analytically to find the normalization constant [Chan et al., 2008]. The problem with this approach is that there is no analytic form for the nonthermal emissivity and coefficient of absorption, and thus it lowers computational efficiency. Also it is not a good approximation to use ultrarelativistic thermal distribution for the temperature range that we are interested in. Therefore we do not pursue this approach.

4.4 Emission and absorption coefficients

We have discussed the details of the electron distribution function. The next step is to define the emission and absorption mechanisms. Bremsstrahlung is very weak compared to the synchrotron radiation from the accreting flow onto Sgr A* [Yuan, Quataert & Narayan, 2003], especially in the innermost region of the disk. Therefore we focus on synchrotron emission and absorption coefficients in this section.

Emission and absorption coefficients can be calculated by integrating the single-electron coefficient over the distribution function. Therefore the coefficients for thermal distribution are different from those for power-law distribution. Unlike previous calculations [Özel, Psaltis & Narayan, 2000, Yuan, Quataert & Narayan, 2003], we

do not use angle-averaged coefficients. The "observer angle" θ, which is the angle between the line of sight and magnetic field line, is kept as an independent variable in the emissivity j_ν (which has units of $dE/dtdVd\nu d\Omega$) and the absorption coefficient α_ν (which has units of 1/length).

4.4.1 Relativistic thermal distribution

The exact formulae for emission and absorption coefficients involve multi-dimensional integrations [Leung, Gammie & Noble, 2009], which are too computationally expensive for calculating the spectrum. Therefore we use analytical formulae which provide good approximation for the fluid variables of interest. Unlike previous calculations of emission from accretion flow onto supermassive black hole, in which ultrarelativistic approximation of thermal synchrotron emissivity is used [Chan et al., 2008, Özel, Psaltis & Narayan, 2000, Yuan, Quataert & Narayan, 2003], we use an approximation which is valid for a larger range of electron temperature. The emissivity is [Leung, Gammie & Noble, 2009]

$$j_\nu = n_e \frac{\sqrt{2}\pi e^2 \nu_s}{3K_2(1/\Theta_e)c} \left(X^{1/2} + 2^{11/12} X^{1/6}\right)^2 \exp\left(-X^{1/3}\right) \ , \tag{4.24}$$

where $\nu_s \equiv (2/9)\nu_c \Theta_e^2 \sin\theta$, $\nu_c \equiv eB/(2\pi m_e c)$ is the electron cyclotron frequency, and $X \equiv \nu/\nu_s$. The absorptivity is then provided by the Kirchhoff's Law

$$\alpha_\nu = B_\nu / j_\nu, \tag{4.25}$$

where B_ν is the Planck function.

At low frequency, equation (4.24) deviates from the exact value, as shown in Leung, Gammie & Noble [2009]. That leads to over-estimation of emission at low-frequency end of the spectrum. We find that we can simply set j_ν and α_ν to zero in order to correct this problem.

4.4.2 Power-law distribution

The synchrotron emission is [Blumenthal & Gould, 1970, Eqs. (4.57) and (4.58)]

$$\begin{aligned}\frac{dW}{d\nu dt} &= \frac{\sqrt{3}ke^3B}{4\pi m_e c^2}\int d\Omega_\theta N(\theta)\sin\theta\int_{\gamma_1}^{\gamma_2}d\gamma\gamma^{-p}\frac{\nu}{\nu_{\rm crit}}\int_{\nu/\nu_{\rm crit}}^{\infty}d\xi K_{5/3}(\xi) \qquad (4.26)\\ &\approx \frac{\sqrt{3}ke^3B}{4\pi m_e c^2}\left(\frac{2\pi m_e c\nu}{3eB}\right)^{-(p-1)/2}(p+1)^{-1}\Gamma\left(\frac{3p-1}{12}\right)\Gamma\left(\frac{3p+19}{12}\right)\\ &\quad\times\int d\Omega_\theta(\sin\theta)^{(p+1)/2}N(\theta)\ , \qquad (4.27)\end{aligned}$$

where k is a constant in the distribution function, the critical frequency $\nu_{\rm crit} = 3eB\gamma^2/(4\pi m_e c)$, θ is the angle between velocity $\vec{v}$ of electron and magnetic field $\vec{B}$, $N(\theta)$ is the θ-dependent part in the distribution function, $K_{5/3}$ is the modified Bessel function of the second kind, Γ is the gamma function. The assumption from the first to second line is that $\nu_{\rm crit}(\gamma=\gamma_1) \ll \nu \ll \nu_{\rm crit}(\gamma=\gamma_2)$. Then the limits on the γ integration can be replaced by 0 and infinity.

$N(\theta)$ is defined in the power-law distribution function

$$N(\gamma,\theta,\vec{r},t) = k\gamma^{-p}N(\theta)/(4\pi) \qquad \text{for } \gamma_1<\gamma<\gamma_2\ , \qquad (4.28)$$

where $\vec{r}$ are the position vector, t is time, k is normalization constant with no time dependence. When there is no θ-dependence, the distribution is $N(\gamma,\vec{r},t) = k\gamma^{-p}$.

For isotropic distribution, $N(\theta) = 1$. The emissivity becomes [Blumenthal & Gould, 1970, Eq. (4.59)]

$$\frac{dW}{d\nu dt} = \frac{4\pi ke^3B^{(p+1)/2}}{m_e c^2}\left(\frac{3e}{4\pi m_e c}\right)^{(p-1)/2}a(p)\nu^{-(p-1)/2}\ , \qquad (4.29)$$

where

$$a(p) = \frac{2^{(p-1)/2}\sqrt{3}}{8\sqrt{\pi}}\frac{\Gamma[(3p-1)/12]\Gamma[(3p+19)/12]\Gamma[(p+5)/4]}{\Gamma[(p+7)/4]}\ . \qquad (4.30)$$

For arbitrary $\gamma_{\rm min}$ and $\gamma_{\rm max}$, the emissivity is

$$j_\nu = n_{\rm pl}\left(\frac{e^2\nu_c}{c}\right)\frac{3^{p/2}(p-1)\sin\theta}{2(p+1)(\gamma_{\rm min}^{1-p}-\gamma_{\rm max}^{1-p})}\Gamma\left(\frac{3p-1}{12}\right)\Gamma\left(\frac{3p+19}{12}\right)\left(\frac{\nu}{\nu_c\sin\theta}\right)^{-(p-1)/2}. \qquad (4.31)$$

Similarly, the absorption coefficient is given by an integral which can be approximated

by

$$\alpha_\nu = n_{\rm pl}\left(\frac{e^2}{\nu m_e c}\right)\frac{3^{(p+1)/2}(p-1)}{4(\gamma_{\rm min}^{1-p}-\gamma_{\rm max}^{1-p})}\Gamma\left(\frac{3p+2}{12}\right)\Gamma\left(\frac{3p+22}{12}\right)\left(\frac{\nu}{\nu_c\sin\theta}\right)^{-(p+2)/2}. \tag{4.32}$$

respectively. These two formulae are valid for $\gamma_{\rm min}^2 \ll \nu/\nu_c \ll \gamma_{\rm max}^2$. Figure (4.2) shows an example of the two formulae, and the exact calculation done by using the `harmony` code [Leung, Gammie & Noble, 2009]. We find that it is a good approximation to use the expression for $\gamma_{\rm min}^2 < \nu/\nu_c < \gamma_{\rm max}^2$.

4.5 Radiative transfer

Radiative transfer (RT) is done by a modified version of `grmonty` [Dolence et al., 2009], which is a relativistic, Monte Carlo, unpolarized RT code. The code includes physics of thermal synchrotron emission and absorption, and Compton scattering. A single-time slice of accretion flow simulation data is used to perform the Monte Carlo RT calculation, which is equal to assuming that the light crossing time is comparable to the dynamical time.

4.5.1 Adding emission of power-law electrons

The total electron number density $N_{\rm tot}$ is the sum of the thermal number density $N_{\rm th}$ and the power-law number density $N_{\rm pl}$. $N_{\rm tot}$ is set to be the number density in the disk model, which is from HARM simulation in our case. Özel, Psaltis & Narayan [2000] and Yuan, Quataert & Narayan [2003], on the other hand, treated the electrons in their RIAF models as thermal. Power-law electrons were added on top on the disk model in their calculation.

$N_{\rm pl}$ is needed for the power-law emissivity. For the simple power-law distribution, $N_{\rm pl}$ is given by equation (4.12). For the broken power-law distribution, there are two cases. If $p > 2$, $\gamma_{\rm min}$ is found by solving $u_{\rm pl} = \eta u_{\rm th}$ and $n_{\rm th}(\gamma_{\rm min}) = n_{\rm pl}(\gamma_{\rm min})$, and then equation (4.18) gives the value of $C_{\rm pl,b}$, which is related to $N_{\rm pl}$ via equation (4.18).

Because emissivity is additive, the new total value is

$$j_{\nu,\rm new} = j_{\nu,\rm th} + j_{\nu,\rm pl} \equiv j_{\nu,\rm old} + j_{\nu,\rm pl}\ . \tag{4.33}$$

Similarly, the new total absorption coefficient is the sum of the thermal and power-law coefficients. This is a consequence of linearity of responses medium to an electromag-

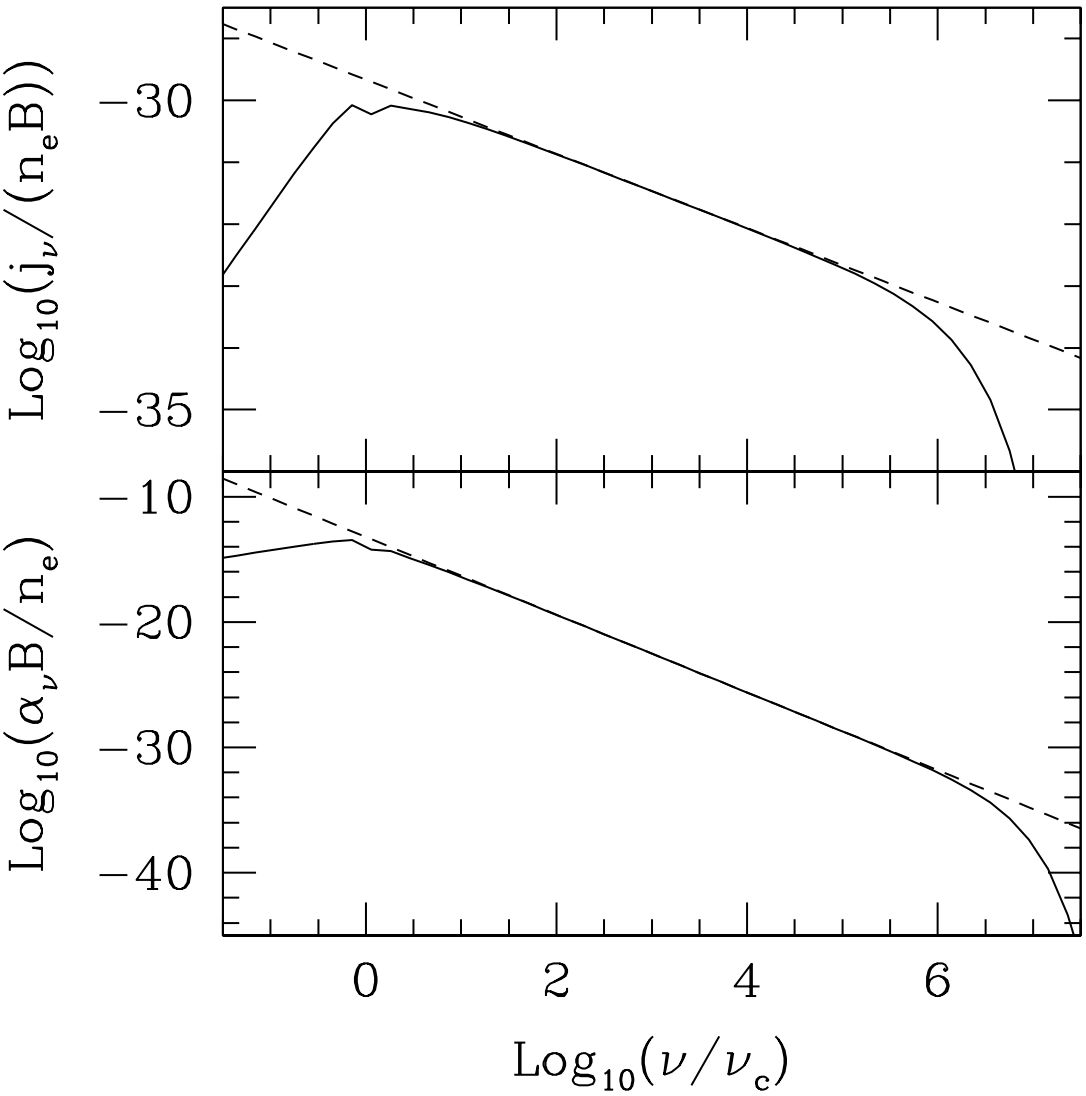

Figure 4.2 Upper panel: the emissivity in cgs units, for $p = 2.2$, $\gamma_{\rm min} = 1$, $\gamma_{\rm max} = 10^3$, and angle $\theta = 60$ deg. The dashed line is the approximate formula in equation (4.31), and the solid line is the exact calculation done by using the `harmony` code [Leung, Gammie & Noble, 2009]. The approximate equation is accurate for $1 \equiv \gamma_{\rm min}^2 < \nu/\nu_c < \gamma_{\rm max}^2 \equiv 10^6$. Lower panel: the absorptivity in cgs units, for the same parameters. The dashed line is calculated by using equation (4.32), and the solid line is result of `harmony`.

netic wave.

4.5.2 Compton scattering cross section of power-law electrons

The power-law electrons can also Compton scatter photons. We are usually interested in situations where $\tau_{\rm cs} \ll 1$ and $\eta \ll 1$, so the Thomson depth of the power-law electrons $\propto \tau_{\rm cs}\eta \ll 1$ and they are negligible. For completeness, however, we describe an implementation of Compton scattering by power-law electrons.

The effective Compton total cross section can be found by averaging the total Klein-Nishina cross section using a probability density function (PDF) in β [Canfield, Howard & Liang, 1987]. In case of thermal distribution, $n_{\rm th}(\beta)/N_{\rm th}$ is the PDF for selecting the value of β at a given Θ_e. Following Canfield, Howard & Liang [1987, Eq. (4)], but in terms of γ, the effective Compton hot cross section (in units of Thomson cross section) can be written as [Canfield, Howard & Liang, 1987, Eq. (4)]

$$\sigma(a,\Theta_e) = \int_1^\infty d\gamma \int_{-1}^1 d\mu \frac{1-\beta\mu}{2}\frac{n_{\rm th}(\gamma)}{N_{\rm th}}\sigma_{\rm KN}(a_0) \ , \tag{4.34}$$

where μ is the cosine of angle between photon and electron trajectories, $a = h\nu/(m_e c^2)$ is the initial photon energy (in units of electron rest mass energy), and $a_0 = \gamma(1-\beta\mu)a$ is the Doppler-shifted photon frequency in the frame of the electron, and $\sigma_{\rm KN}(\nu_0)$ is the total Klein-Nishina cross section.

Now consider more than one species of electrons. Assume species i has distribution function n_i and number density N_i, and the total number density is $N_{\rm tot} = \sum_i N_i$. Like absorption coefficient, the scattering opacity is additive. Therefore

$$\alpha_{\rm scatt} = \sum_i \left[N_i \sigma_i(a,\Theta_e)\right] \equiv \sum_i \left[N_i \int_1^\infty d\gamma \int_{-1}^1 d\mu \frac{1-\beta\mu}{2}\frac{n_i(\gamma)}{N_{\rm tot}}\sigma_{\rm KN}(a_0)\right] \ . \tag{4.35}$$

The last line defines the effective hot cross section σ_i for species i.

To minimize the changes in `grmonty`, we further rewrite the opacity as

$$\alpha_{\rm scatt} = N_{\rm tot}\bar{\sigma} \ , \tag{4.36}$$

where the average cross section is

$$\begin{aligned} \bar{\sigma} &\equiv \sum_i \left[\frac{N_i}{N_{\rm tot}} \int_1^\infty d\gamma \int_{-1}^1 d\mu \frac{1-\beta\mu}{2}\frac{n_i(\gamma)}{N_{\rm tot}}\sigma_{\rm KN}(a_0)\right] \\ &= \int_1^\infty d\gamma \int_{-1}^1 d\mu \frac{1-\beta\mu}{2} \sum_i \left[\left(\frac{N_i}{N_{\rm tot}}\right)^2 \frac{n_i(\gamma)}{N_i}\right] \sigma_{\rm KN}(a_0) \ . \end{aligned} \tag{4.37}$$

4.5.3 Compton scattering sampling

In Monte Carlo simulation, the electron distribution is sampled in order to find out the details about the scattered electron. For the energy of the electron, one can sample γ, β or E by rewriting the electron distribution in terms of the corresponding variable. We follow Dolence et al. [2009] to sample the distribution using β. Notice that β and μ are sampled separately, as described by Dolence et al. [2009, §5.2]. The β sampling scheme follows the procedure of Canfield, Howard & Liang [1987, p. 572]. The scheme is only correct for thermal distribution, so an additional sampling scheme for power-law distribution is added.

Sampling scheme for power-law distribution: inversion

The PDF is the normalized distribution function $N_{\rm pl}^{-1} n_{\rm pl}$. The cumulative distribution function (CDF)

$$\mathrm{CDF}(\beta) \equiv \int_0^\beta \mathrm{PDF}(\beta_1) d\beta_1 = \int_1^{\gamma(\beta)} \mathrm{PDF}(\gamma_1) d\gamma_1 \tag{4.38}$$

can be used to sample β. If $\mathrm{CDF}(\beta)$ can be inverted, then the value of β is given by $\mathrm{CDF}^{-1}(x)$, where $x \in [0, 1)$ is a uniform random number.

For the simple power-law distribution equation (4.8), the PDF are

$$\mathrm{PDF}_{\rm pl,s}(\beta)\, d\beta = \begin{cases} \dfrac{C_{\rm pl,s}}{N_{\rm pl}} \gamma^{3-p} \beta \, d\beta = \dfrac{p-1}{\gamma_{\rm min}^{1-p} - \gamma_{\rm max}^{1-p}} \gamma^{3-p} \beta \, d\beta & \text{for } \gamma_{\rm min} \le \gamma \le \gamma_{\rm max} \\ 0 & \text{otherwise .} \end{cases} \tag{4.39}$$

The CDF is

$$\mathrm{CDF}_{\rm pl,s}(\beta) = \begin{cases} 0 & \text{for } \gamma < \gamma_{\rm min} \\ \dfrac{\gamma_{\rm min}^{1-p} - \gamma^{1-p}}{\gamma_{\rm min}^{1-p} - \gamma_{\rm max}^{1-p}} & \text{for } \gamma_{\rm min} \le \gamma \le \gamma_{\rm max} \\ 1 & \text{for } \gamma > \gamma_{\rm max} \end{cases} \tag{4.40}$$

and the inverse is

$$\mathrm{CDF}_{\rm pl,s}^{-1}(x) = \sqrt{1 - \frac{1}{\tilde{\gamma}^2}}\,, \quad \tilde{\gamma} = \left[(1-x)\gamma_{\rm min}^{1-p} + x\gamma_{\rm max}^{1-p}\right]^{1/(1-p)} \,. \tag{4.41}$$

For the broken power-law distribution equation (4.17) with $p > 1$, the PDF is

$$\mathrm{PDF}_{\mathrm{pl,b}}(\beta)\, d\beta = \begin{cases} \dfrac{C_{\mathrm{pl,b}}}{N_{\mathrm{pl}}}\gamma^{3-p}\beta\, d\beta & \text{for } \gamma_{\min} \le \gamma \le \gamma_{\mathrm{c}} \\ \dfrac{C_{\mathrm{pl,b}}}{N_{\mathrm{pl}}}\gamma_{\mathrm{c}}\gamma^{2-p}\beta\, d\beta & \text{for } \gamma_{\mathrm{c}} \le \gamma \le \gamma_{\max} \\ 0 & \text{otherwise}\ , \end{cases} \tag{4.42}$$

where $C_{\mathrm{pl,b}}$ is given by equation (4.18). The CDF is

$$\mathrm{CDF}_{\mathrm{pl,b}}(\beta) = \begin{cases} 0 & \text{for } \gamma < \gamma_{\min} \\ \dfrac{C_{\mathrm{pl,b}}}{(p-1)N_{\mathrm{pl}}}\left(\gamma_{\min}^{1-p} - \gamma^{1-p}\right) & \text{for } \gamma_{\min} \le \gamma \le \gamma_{\mathrm{c}} \\ \dfrac{C_{\mathrm{pl,b}}}{(p-1)N_{\mathrm{pl}}}\left(\gamma_{\min}^{1-p} - \gamma_{\mathrm{c}}^{1-p}\right) + \dfrac{C_{\mathrm{pl,b}}}{pN_{\mathrm{pl}}}\gamma_{\mathrm{c}}\left(\gamma_{\mathrm{c}}^{-p} - \gamma^{-p}\right) & \text{for } \gamma_{\mathrm{c}} \le \gamma \le \gamma_{\max} \\ 1 & \text{for } \gamma > \gamma_{\max}\ . \end{cases} \tag{4.43}$$

The inverse is

$$\mathrm{CDF}^{-1}_{\mathrm{pl,b}}(x) = \sqrt{1 - \frac{1}{\tilde{\gamma}^2}}\ ,$$

$$\tilde{\gamma} = \begin{cases} \left[\gamma_{\min}^{1-p} - \dfrac{x(p-1)N_{\mathrm{pl}}}{C_{\mathrm{pl,b}}}\right]^{1/(1-p)} & \text{for } x \le \mathrm{CDF}_{\mathrm{pl,b}}(\beta_{\mathrm{c}}) \\ \left\{\gamma_{\mathrm{c}}^{-p} - \left[\dfrac{N_{\mathrm{pl}}(p-1)}{C_{\mathrm{pl,b}}}x - \gamma_{\min}^{1-p} + \gamma_{\mathrm{c}}^{1-p}\right]\dfrac{p}{(p-1)\gamma_{\mathrm{c}}}\right\}^{-1/p} & \text{for } x > \mathrm{CDF}_{\mathrm{pl,b}}(\beta_{\mathrm{c}})\ . \end{cases} \tag{4.44}$$

Sampling scheme for power-law distribution: rejection

In general, one can choose β by rejection method. The simplest envelope function is the maximum of PDF(β). Choose two uniform random numbers $x_1, x_2 \in [0, 1)$. If $x_1 < \mathrm{PDF}(x_2)$, accept x_2 as β; otherwise, choose two new random numbers and repeat the process.

In practice, we find that we can ignore the effect of power-law electron in Compton scattering due to two reasons. First, we only add a small amount (less than 1% in terms of energy) of power-law electron to the calculation, so the effect of power-law electron is very small. Second, introduction of power-law electrons lead to increasing in high-energy photons which have negligible cross section, because Klein-Nishina cross section $\propto \ln\epsilon/\epsilon$.

4.5.4 Sampling Klein-Nishina cross section

The addition of power-law distribution leads to more photons at high energy. Because Klein-Nishina cross section is very small when photon energy is high, the sampling becomes very inefficient compared to calculation with only thermal distribution. Here we explain how to make the calculation more efficient.

Klein-Nishina formula

The Klein-Nishina formula is [Heitler, 1954, Eq. (22.39)]

$$\frac{d\sigma_{\rm KN}}{d\Omega} = \frac{r_0^2}{2}\frac{a_{\rm s}^2}{a^2}\left(\frac{a}{a_{\rm s}} + \frac{a_{\rm s}}{a} - \sin^2\theta\right) \ , \tag{4.45}$$

where Ω is the solid angle, r_0 is the classical electron radius, $a = h\nu/(m_e c^2)$ is the initial photon energy (in units of electron rest mass energy), $a_{\rm s}$ is the scattered photon energy, and θ is the scattering angle. By conservation of momentum and energy, the scattering energy can be expressed as [Heitler, 1954, Eq. (22.4)]

$$a_{\rm s} = \frac{a}{1 + a(1-\cos\theta)} \equiv \frac{a}{1 + a(1-\mu)} \ , \tag{4.46}$$

which ranges from $a_{\rm s,min} \equiv a/(1+2a)$ at $\theta = \pi$ (backward scattering), to $a_{\rm s,max} \equiv a$ at $\theta = 0$ (no scattering). Eliminating θ in equation (4.45) by using equation (4.46), one has

$$\frac{d\sigma_{\rm KN}}{d\Omega} = \frac{r_0^2}{2}\frac{a_{\rm s}^2}{a^2}\left[\frac{a}{a_{\rm s}} + \frac{a_{\rm s}}{a} + \left(1 + \frac{1}{a} - \frac{1}{a_{\rm s}}\right)^2 - 1\right] \ . \tag{4.47}$$

The differential Klein-Nishina cross section can be written as

$$\begin{aligned}
\frac{d\sigma_{\rm KN}}{da_{\rm s}} &= \left(\int_0^{2\pi} d\phi\right) \cdot \frac{d\sigma_{\rm KN}}{d\mu d\phi} \cdot \frac{d\mu}{da_{\rm s}} \\
&= 2\pi \cdot \frac{d\sigma_{\rm KN}}{d\Omega} \cdot \frac{1}{a_{\rm s}^2} \\
&= \pi r_0^2 \frac{1}{a^2}\left[\frac{a}{a_{\rm s}} + \frac{a_{\rm s}}{a} + \left(1 + \frac{1}{a} - \frac{1}{a_{\rm s}}\right)^2 - 1\right] \\
&= \sigma_{\rm T}\frac{3}{8a^2}\left[\frac{a}{a_{\rm s}} + \frac{a_{\rm s}}{a} + \left(1 + \frac{1}{a} - \frac{1}{a_{\rm s}}\right)^2 - 1\right] \ ,
\end{aligned} \tag{4.48}$$

where $\sigma_{\rm T} = (8\pi/3)r_0^2$ is the Thomson cross section. Canfield, Howard & Liang [1987, Eq. (2)] misses a factor of a^2 compared to equation (4.48). In fact, the missing factor

a^2 can be obtained by comparing their equations (2) and (3).

The total Klein-Nishina is

$$\begin{aligned}\sigma_{\rm KN} &= \int_{a/(1+2a)}^{a} da_{\rm s} \frac{d\sigma_{\rm KN}}{da_{\rm s}} \\ &= \sigma_{\rm T} \frac{3}{4a^2}\left[2 + \frac{a^2+a^3}{(1+2a)^2} + \frac{a^2-2a-2}{2a}\ln(1+2a)\right] ,\end{aligned} \tag{4.49}$$

which is the same as Rybicki & Lightman [1979, Eq. (7.5)], Heitler [1954, Eq. (22.45)] and Canfield, Howard & Liang [1987, Eq. (3)].

4.5.5 Sampling differential Klein-Nishina cross section

To find the frequency and direction of the scattered photon in the electron frame, one has to sample the differential Klein-Nishina cross section [Canfield, Howard & Liang, 1987, §A.IV, step 4]. As we can see in this section, when the initial photon energy is high, the sampling efficiency of rejection using a simple capping function is very low. This is not a problem if only thermal electrons are considered, because the tail in the distribution drops off so fast that not many electrons can emit high-energy photon. Test-runs with HARM data show that even the up-scattered photon would not cause much trouble.

The situation is different for the relatively flat power-law distribution. Even a small amount of power-law electrons can raise the high-frequency end of the spectrum, especially when power-law index p is small. The lack of efficiency can be a problem. Therefore here we consider a more efficient sampling method.

The function for sampling is

$$f_{\rm KN}(a, a_{\rm s}) = \frac{8}{3\sigma_{\rm T}} \frac{d\sigma_{\rm KN}}{da_{\rm s}} = \frac{1}{a^2}\left[\frac{a}{a_{\rm s}} + \frac{a_{\rm s}}{a} + \left(1 + \frac{1}{a} - \frac{1}{a_{\rm s}}\right)^2 - 1\right] . \tag{4.50}$$

Recall that $a_{\rm s,min} \le a_{\rm s} \le a_{\rm s,max}$ with $a_{\rm s,min} \equiv a/(1+2a)$ and $a_{\rm s,max} \equiv a$.

The envelope function can be a power-law function

$$f_{\rm p}(a, a_{\rm s}) = c(a)\, a_{\rm s}^{p(a)} , \quad p(a) = 1 - \frac{\ln(1+2a+2a^2)}{\ln(1+2a)} , \quad c(a) = 2a^{-p(a)-2} \tag{4.51}$$

and a linear function

$$f_{\rm lin}(a, a_{\rm s}) = m(a)\, a_{\rm s} + b(a) , \quad m(a) = -\frac{2}{a^2} , \quad b(a) = \frac{2(1+a)}{a^2} . \tag{4.52}$$

Both $f_{\rm p}$ and $f_{\rm lin}$ join the two end points of $f_{\rm KN}$. A third choice is a "flat" function

$$f_{\rm flat}(a, a_{\rm s}) = f_{\rm KN}(a, a_{\rm s,min}) = \frac{2 + 4a + 4a^2}{a^2 + 2a^3} \tag{4.53}$$

which equals the maximum value of $f_{\rm KN}$.

Figure (4.3) shows the envelope functions for different values of a. When a is small, the three functions are similar. As a increases, $f_{\rm p}$ follows the $f_{\rm KN}$ much more closely compared to the other two functions, and thus the efficiency of rejection method using $f_{\rm KN}$ is a lot higher. Considering the fact that $f_{\rm p}$ is more computationally expensive to calculate, a sensible rejection method is to use $f_{\rm p}$ only when $a > 10$. Otherwise, $f_{\rm flat}$ is used.

To do rejection using $f_{\rm p}$, we need the integrated function

$$F_{\rm p}(a, a_{\rm s}) = \int_{a_{\rm s,min}}^{a_{\rm s}} f_{\rm p}(a, x)dx = \frac{c(a)}{p(a)+1}\left(a_{\rm s}^{p(a)+1} - a_{\rm s,min}^{p(a)+1}\right) \tag{4.54}$$

and the inverse

$$F_{\rm p}^{-1}(a, x) = \left(\frac{p(a)+1}{c(a)}x + a_{\rm s,min}^{p+1}\right)^{1/[p(a)+1]} . \tag{4.55}$$

The rejection procedure is

(1) Choose a uniform random number $x_1 \in [0, F_{\rm p}(a, a_{\rm s,max}))$. Calculate $a_{\rm s,1} = F_{\rm p}^{-1}(a, x_1)$.

(2) Choose a uniform random number $x_2 \in [0, f_{\rm p}(a, a_{\rm s,1}))$.

(3) If $x_2 < f_{\rm KN}(a, a_{\rm s,1})$, accept $a_{\rm s,1}$ as $a_{\rm s}$; otherwise go back to step (1).

4.6 Code test

The `grmonty` code with only thermal distribution has been tested rigorously [Dolence et al., 2009]. Therefore we decide to first test our modification against the original code. As the power-law energy fraction decreases, the spectrum is expected to converge to the spectrum with only thermal distribution. Figure (4.4) shows an example for $\eta = 1 \times 10^{-10}$. We have tested the code for different power-law parameters. All of them show the same result (within statistical error).

The power-law emissivity equation (4.31) is proportional to $\nu^{-(p-1)/2}$. Therefore when the power-law synchrotron radiation is the dominant emission mechanism at a particle frequency, we expect the slope in the SED, or a νL_ν spectrum, to be $-(p-1)/2 + 1 = (3-p)/2$. Figure (4.5) shows that the code produces a spectrum

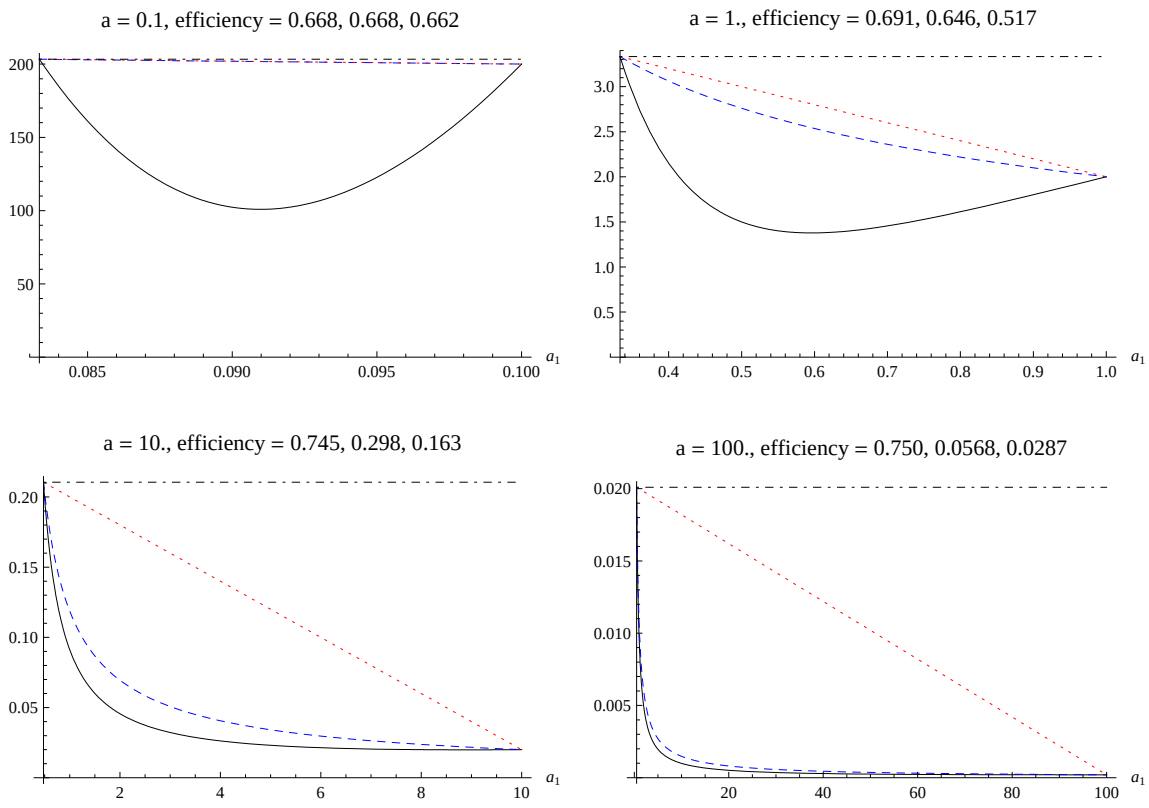

Figure 4.3 Envelop functions for sampling differential Klein-Nishina for different values of a. Solid line is $f_{\rm KN}(a, a_{\rm s})$. The efficiencies are for rejection method using $f_{\rm p}$ (blue dashed line), $f_{\rm lin}$ (red dotted line) and $f_{\rm flat}$ (black dotted-dashed line) respectively.

with correct slope for $p = 2.5$ and 3. For $p = 3.5$ and 4, the power-law synchrotron contribution is "buried" among the thermal synchrotron and Compton scattering contribution. Because we keep the total energy in all electron distributions, the addition of power-law species lowers the thermal electron number density. The effect is clear for $p = 4$, at which most of the power-law electrons have low energy and thus do not contribute to emission in mm and infrared (IR) bands, therefore the SED of $p = 4$ case is lower than the SED with only thermal electrons.

To further test our calculation, we compare Figure (4.5) with a similar calculation in Özel, Psaltis & Narayan [2000]. Özel, Psaltis & Narayan [2000] calculate the spectra up to IR frequency because there is no Compton scattering in their model. We use the same energy fraction η and power-law indices p. The two figures show that the slopes and the normalization (compared to the sub-mm bump) are similar in both calculations. Even though there are resemblance in the two plots comparison, notice that we do not rescale the curves in Figure (4.5) because exact comparison between

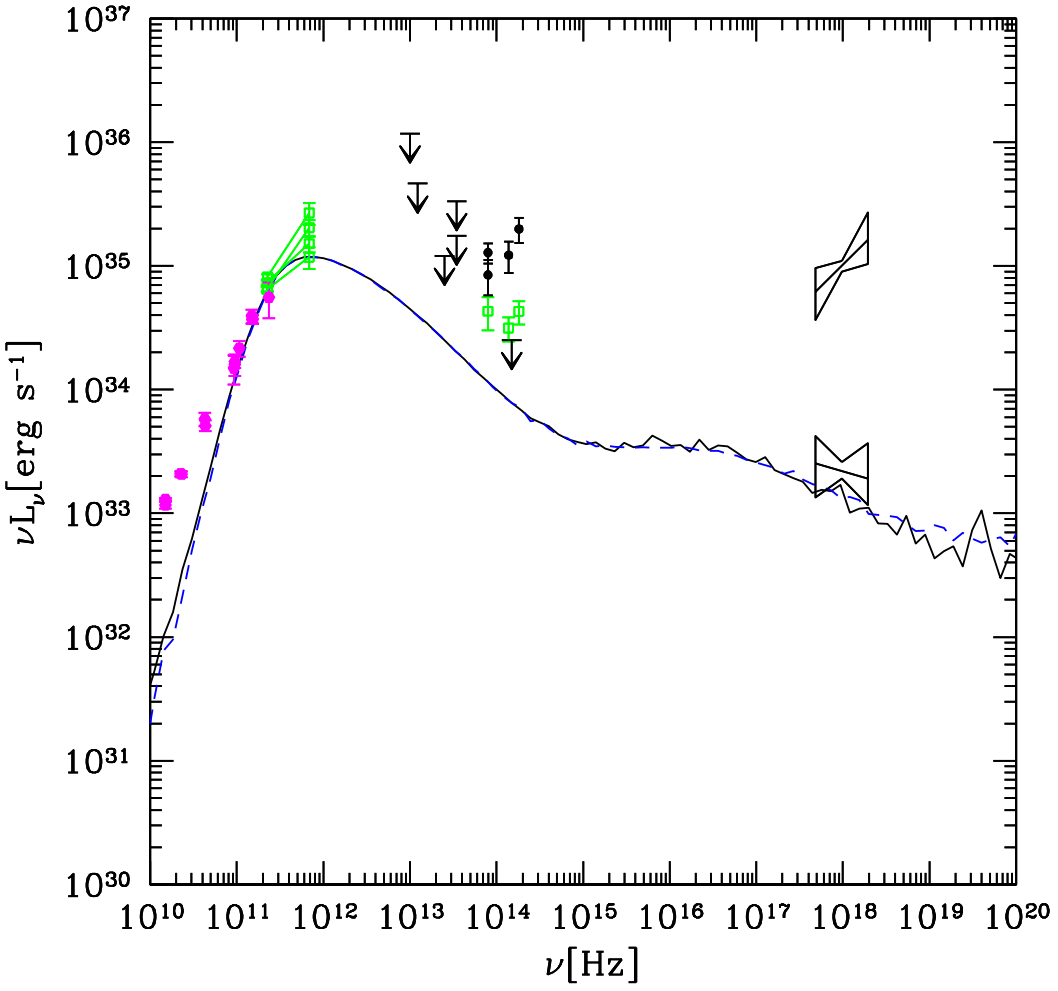

Figure 4.4 Spectra of a single slice of accretion disk data, adjusted to fit the flux of Sgr A* at 1.3 mm. Disk parameters are $a_* = 0.94$, $T_i/T_e = 3$, and orientation $i = 85°$. Solid line is calculation with only thermal electron. Dashed line is calculation with power-law energy fraction $\eta = 1 \times 10^{10}$, $\gamma_{\rm min} = 1$, $\gamma_{\rm max} = 1000$, $p = 2.2$.

Figure (4.5) and Figure 3b of Özel, Psaltis & Narayan [2000] is not meaningful due to the numerous differences in the two calculations. We leave the discussion of the differences to section 4.7.

We test the implementation of broken power-law in Figure (4.6), we increase $\gamma_{\rm c}$ gradually to make sure that spectrum would converge to that of a simple power-law. We are also able to verify the expected decrease of the spectral slope of a broken power-law after the cooling break. This is also confirmed by the calculation by Yuan, Quataert & Narayan [2003].

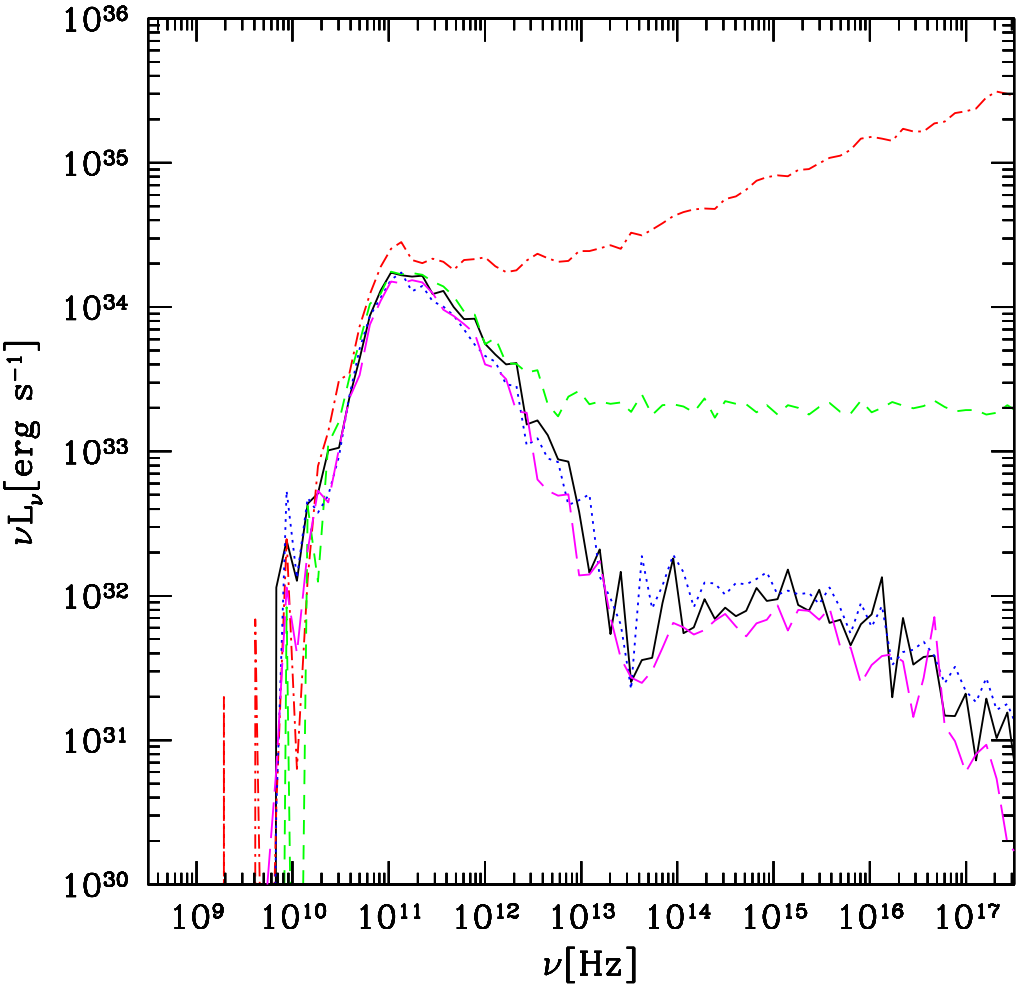

Figure 4.5 Synchrotron spectra for thermal distribution (solid line), and models with both thermal and power-law distributions. The dotted-dashed line, dashed line, dotted line and long dashed line refer to model with $p = 2.5$, 3, 3.5 and 4 respectively. Other parameters in the power-law distribution are $\eta = 0.01$, $\gamma_{\rm min} = 1$, $\gamma_{\rm max} = \infty$. Disk parameters are $a_* = 0.94$, $T_i/T_e = 3$, orientation $i = 85°$. All the models are calculated assuming the same accretion rate. A single time-slice of accretion simulation is used in the calculation.

4.7 Results

4.7.1 Agreement with flaring data

The calculation of SED is very expensive. To get good signal-to-noise in the SED, a lot of photons are used in the Monte Carlo radiative transfer. One needs to repeat the calculation for each time slice of accretion disk model. Many time slices are needed

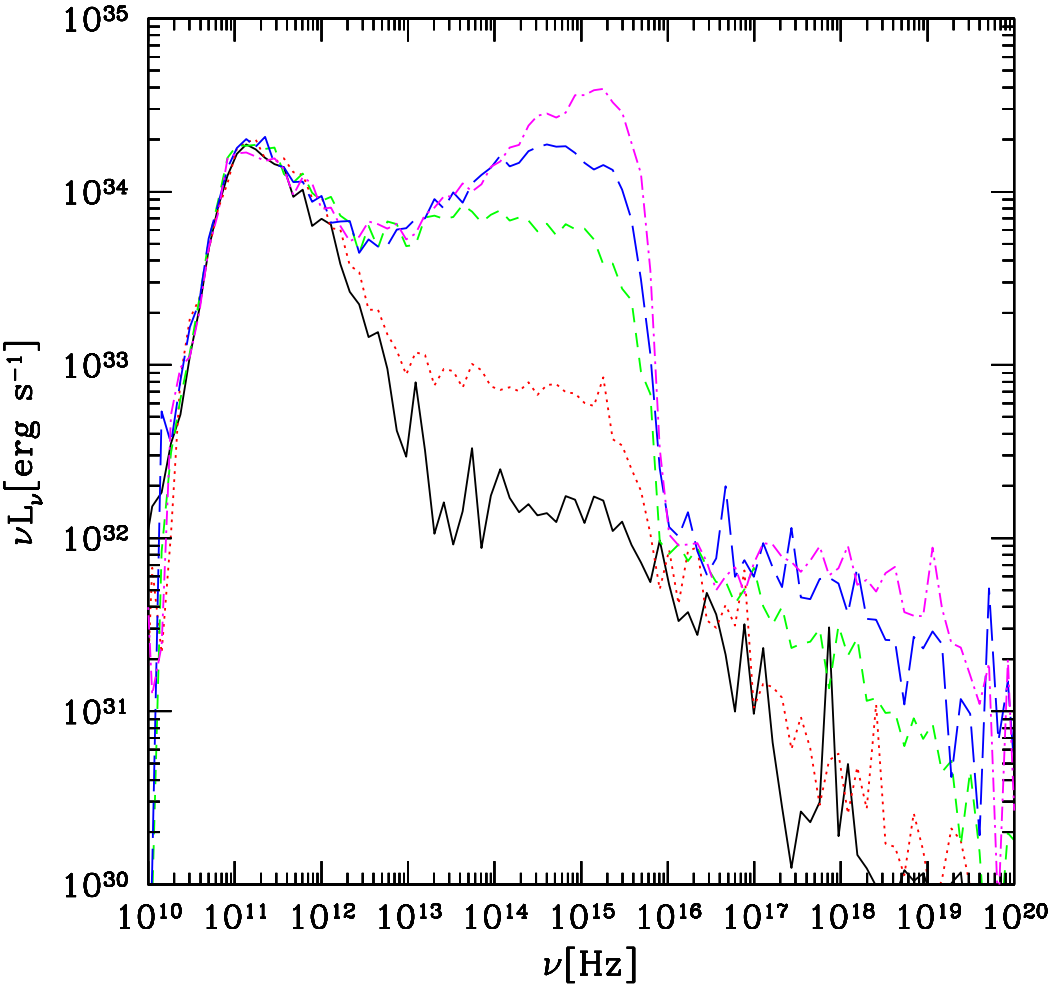

Figure 4.6 Convergence of broken power-law spectrum to simple power-law spectrum. $\gamma_{\rm min} = 1$, $\gamma_{\rm max} = 10000$ in all calculations. At 10^{15} Hz, the four lines from the bottom to the top are broken power-law calculation with $\gamma_{\rm c} = 10, 100, 1000, 3000$. The top line is simple power-law distribution.

to get an average spectrum. Besides, the spectrum changes non-linearly with the change of mass accretion rate. Therefore, one has to redo the calculation in order to match the spectrum to the observational constraints. In our previous parameter survey with only thermal electrons [Mościbrodzka, et al., 2009], it takes a long time to do the calculation even though only three model parameters are considered (black hole spin, orientation angle, and ion-to-electron temperature ratio).

The parameter space in the calculation is vastly increased after the implementation of power-law electron. Even though we limit our calculation to only simple and broken power-law distributions, and require both distribution to be isotropic, the number of

parameters is still too large for a complete survey. The problem is also not well constrained if one allows any kind of power-law distribution, especially because there are no observational data between IR and X-ray frequencies. The large number of parameters mean that there are many degeneracies among them.

Our way of tackling this problem is twofold. First we add power-law electrons to the best-bet model in Mościbrodzka, et al. [2009], to check whether it is possible to satisfy observational constraint of spectral slope of NIR flares, without violating other observational constraints. Second, to justify why we do not do a fitting or a parameter survey, we demonstrate that it is possible to turn the parameters to satisfy all the observations. The degeneracies in the parameters prevent us to make meaningful statement about the exact power-law models. However, it is clear that some kinds of power-law distribution are needed to satisfy the current data, especially because all other possible emission mechanisms are ruled out, as discussed in section 4.1.

Mościbrodzka, et al. [2009] calculates the spectrum of Sgr A* by averaging the spectra of 200 time slices of accretion disk simulation. By performing a survey with three parameters, the best-bet accretion disk model is found to have ion-to-electron temperature ratio $T_i/T_e = 3$, black hole spin $a_* = 0.94$, and disk orientation angle $i = 85°$ (nearly edge-on). Besides, the best-bet model satisfies the image size constraint set by VLBI at radio frequencies. We therefore add a use small fraction of power-law electrons ($\eta < 0.01$) so that the radio emission essentially does not change after we have matched the flux at 1.3 mm. The images of our models are therefore the same as the thermal models. However, it is possible that certain models with large power-law energy fraction could also satisfy the image size constraint, though it is not our goal to find a new best-bet model.

A power-law distribution with index p produce spectrum with spectral slope $(3 - p)/2$. The spectrum will be shallower at frequency near to $\gamma_{\rm c}$ (for broken power-law) or $\gamma_{\rm max}$ (for both simple and broken power-law). Therefore, in order to produce a spectral slope of 0.4 ± 0.2 between 3.8 and 1.6 μm (7.9×10^{15} to 1.9×10^{16} Hz), the spectral index is at most 2.6. Figure (4.7) shows an example of how we can predict the correct slope at NIR, which is not possible when there are only thermal electrons in the model.

Notice that the X-ray emission Figure (4.7) is higher than the lower "bow tie". Unlike Mościbrodzka, et al. [2009], here we use the flaring emission (instead of the quiescent emission) as the upper limit at X-rays, because the NIR spectral index observations that motivate our calculation are flaring events. One may try to fit the X-ray flares (upper bow tie), as in Yuan, Quataert & Narayan [2003] and Dodds-Eden

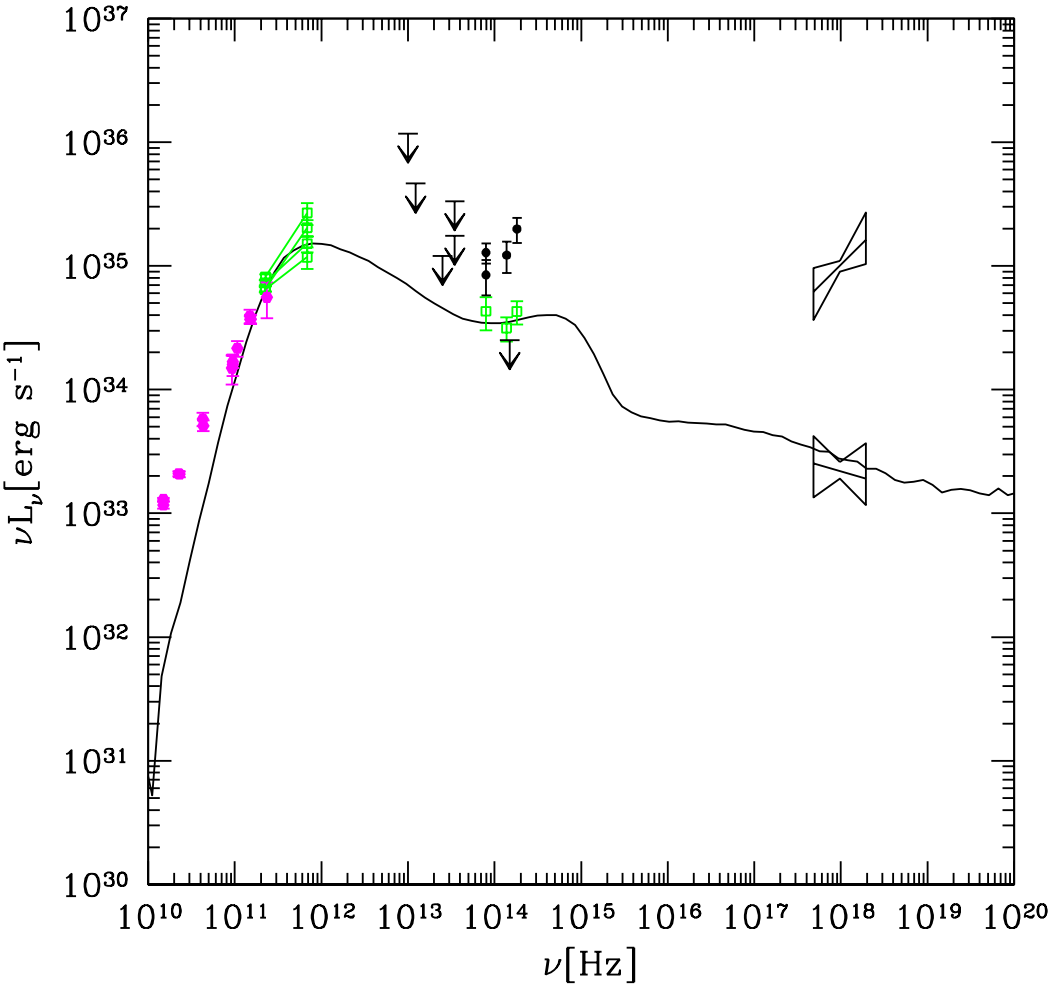

Figure 4.7 Adding 0.03% of power-law to the best-bet model in [Mościbrodzka, et al., 2009]. Power-law index $p = 2.1$, orientation angle is 85°. Quiescent data from the left to the right are from An et al. [2005], Falcke et al. [1998], Marrone et al. [2006] at radio bands, Genzel et al. [2003] at NIR and Baganoff et al. [2003] at X-rays. Upper limits at NIR are from Hornstein et al. [2007], Melia & Falcke [2001], Schödel et al. [2007]. Flaring data are from from Dodds-Eden et al. [2009], Genzel et al. [2003] at NIR, and Baganoff et al. [2001] at X-ray.

et al. [2009]. However, it is not clear whether the X-ray flares are produced directly by synchrotron emission, thus there is a freedom of how to use the observational data at X-rays. We choose not fitting the X-ray flaring data also because the large freedom of power-law models do not allow us to constrain the parameters in any meaningful way. While it is reasonable to predict the power-law spectrum over a small range of frequencies at NIR, it is overstretching to use the model to predict the spectrum all

the way up to X-ray.

Another reason of discouraging us to fit the X-ray flaring data with power-law synchrotron emission is the cooling time of high-energy electrons which can produce X-rays is of order seconds to tens of seconds. The observed X-ray flares, on the other hand, last for tens of minutes. There has to be an injection mechanism that continues to pump energy into the power-law electrons in order to produce X-ray flares directly by synchrotron emission. That further complicates the power-law models and introduces even more parameters.

Figures (4.8) to (4.10) are examples of how different set of power-law parameters can all produce spectrum that satisfies all the observational constraint. We are able to produce the correct spectrum for a wide range of parameters. For example, there is freedom in choosing $\gamma_{\rm max}$. An increase in $\gamma_{\rm max}$ moves the peak at IR towards ultraviolet, without essential no change in the spectral slope at NIR and the overall normalization. Besides simple power-law, broken power-law calculations can also produce satisfied models for $p < 1.6$. It is therefore not possible to constrain the parameters in the system.

There are several attempts in the literature to model the spectrum of Sgr A* by including power-law synchrotron emission. In this section we discuss the improvements and differences of our calculation, compared to the previous ones. We also discuss the conclusion that we can draw from our calculation.

4.7.2 Comparison with Özel, Psaltis & Narayan [2000]

We mention in section 4.6 that our calculation resemble the result of Özel, Psaltis & Narayan [2000]. However, there are a lot of differences in the calculation and the underlying assumption. Özel, Psaltis & Narayan [2000] use an ADAF disk model whereas we use data from an MHD accretion disk simulation. Their disk model extends to a very large radius, at which the emission contributes to the right of the sub-mm bump. On the other hand, our disk model only extends to 20 Schwarzschild radii. Therefore we have less emission at radio wavelength and the slope below $\sim 10^{11}$ Hz in our calculation is not correct.

Özel, Psaltis & Narayan [2000] use pitch-angle-averaged emissivity and absorptivity. Since we have detailed information about direction of magnetic field in the simulation, we choose to keep the angle dependence in the synchrotron emission. Another improvement that we have made is to include Compton scattering in the radiative transfer. We can calculate the spectrum from radio wave to X-ray, while

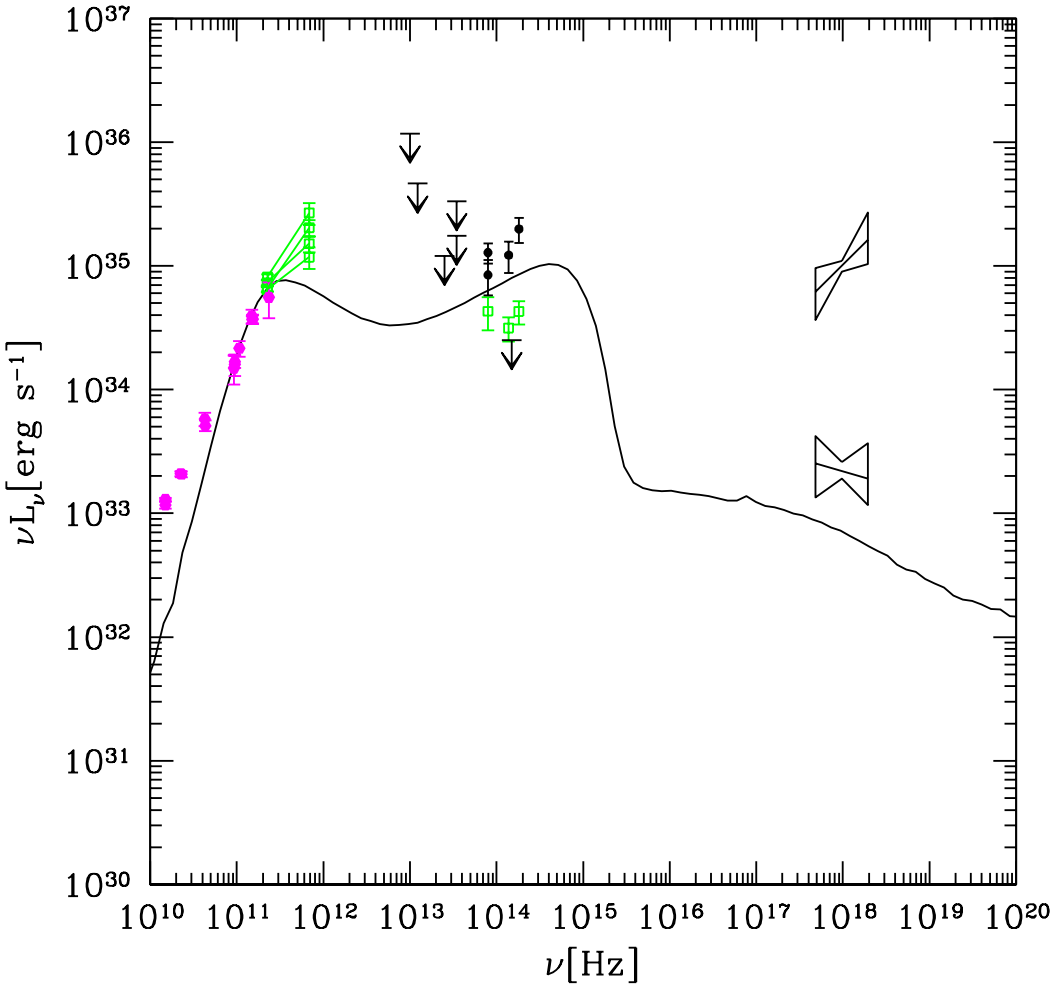

Figure 4.8 Spectrum of power-law model, with $p = 2.2$, $\eta = 0.1\%$, $\gamma_{\rm min} = 1$, $\gamma_{\rm max} = 4000$. Disk model is $T_i/T_e = 3$ and $a_* = 0.94$, observed at $i = 45°$. Sources of data are cited in caption of Figure (4.7).

Özel, Psaltis & Narayan [2000] had to limit their calculation to the region around the sub-mm bump due to the lack of Compton scattering.

There are further differences in the assumption about the electron distribution. As mentioned before, when we add power-law electrons, we decrease the thermal number density so that the total energy is fixed. Özel, Psaltis & Narayan [2000] instead keep the thermal number density fixed. Besides, while their distribution is equivalent to the simple power-law distribution in our calculation, they limit their calculation to a smaller range of frequency, such that their spectra do not show the peak that corresponds to $\gamma_{\rm max}$. The final major difference is that their spectra are

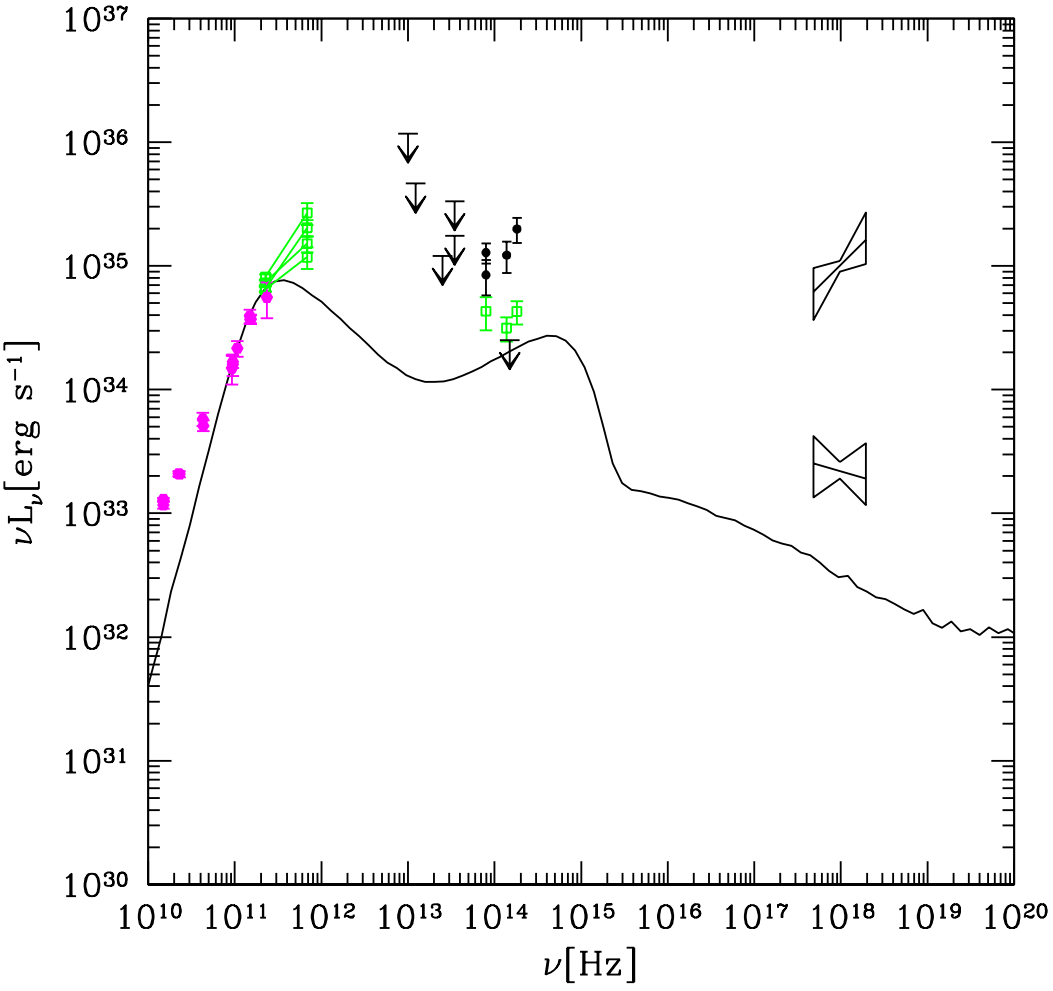

Figure 4.9 Spectrum of power-law model, with $p = 2.1$, $\eta = 0.03\%$, $\gamma_{\rm min} = 1$, $\gamma_{\rm max} = 4000$. Disk model is $T_i/T_e = 3$ and $a_* = 0.94$, observed at $i = 45°$. Sources of data are cited in caption of Figure (4.7).

averaged over orientation angle whereas orientation is a parameter in our model. They also do not change the thermal electron number density when they add power-law electron, whereas we lower the thermal electron number density to keep the total energy constant.

Despite the vastly different assumptions and details, our spectra show similar features compared to those in Özel, Psaltis & Narayan [2000]. Location of the sub-mm peak in their simulation is the same as ours. Both calculations obtain the correct slopes of the power-law tails. The normalization of the power-law contribution to the spectrum, relative to the thermal bump, is also similar in both calculations.

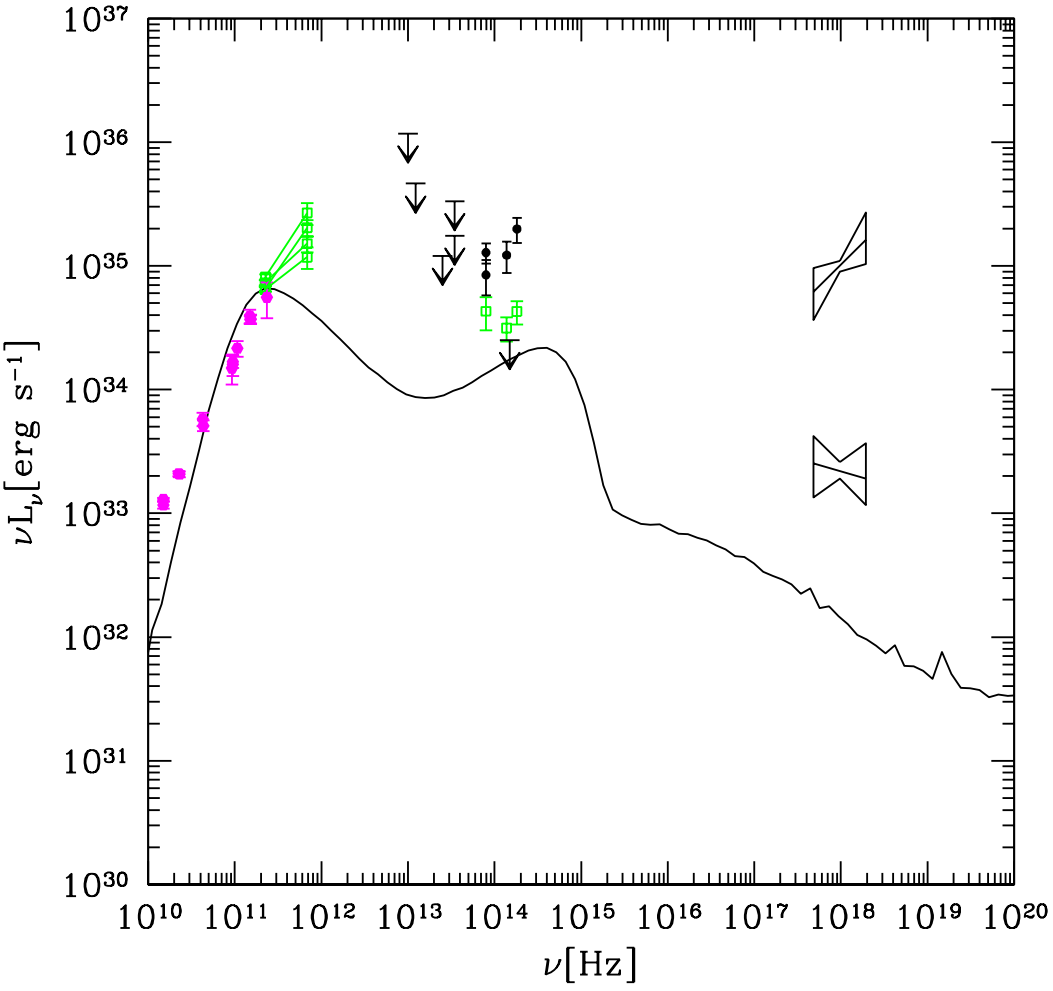

Figure 4.10 Spectrum of power-law model, with $p = 2.01$, $\eta = 1\%$, $\gamma_{\rm min} = 1$, $\gamma_{\rm max} = 4000$. Disk model is $T_i/T_e = 3$ and $a_* = 0.94$, observed at $i = 45°$. Sources of data are cited in caption of Figure (4.7).

4.7.3 Comparison with Yuan, Quataert & Narayan [2003]

Yuan, Quataert & Narayan [2003] also assume an ADAF disk model. However, they have an extra parameter compared to Özel, Psaltis & Narayan [2000], so that the density profile can deviate from that of a spherical Bondi flow. They use non-angle-averaged emissivity (but angle-averaged absorptivity), a simple model of Compton scattering, and also a broken power-law distribution that starts from the thermal distribution. Because Yuan, Quataert & Narayan [2003] have a smooth disk model that provides synchrotron cooling rate and matter accretion rate as a function of radius r, they are able to make $\gamma_{\rm c} = \gamma_{\rm c}(r)$. We decide to use a fixed cooling break,

estimated using the accretion rate near to innermost stable circular orbit (ISCO), due to the large fluctuation of fluid variables in our simulated disk model. It is justified by the fact that most emission originates from regions near to the ISCO [Beckwith, Hawley & Krolik, 2008].

Besides the way that the cooling break is calculated, the difference in in the disk model also prevent a direct comparison between our calculation and that in Yuan, Quataert & Narayan [2003]. Due to variation between the fluid variables among time slices of our accretion disk simulation, the cooling break varies for at most two orders of magnitude. Yuan, Quataert & Narayan [2003], on the other hand, have a steady disk model. However, we still find the same change of slope in the power-law tails compared to Yuan, Quataert & Narayan [2003, Figure 4].

Yuan, Quataert & Narayan [2003] also fit the flaring X-ray data with power-law synchrotron emission. As we have discussed above, we choose not to do such a fitting.

4.8 Conclusion

We have performed a relativistic RT calculation with GRMHD accretion flow simulation. By adding a small power-law component to the mostly thermal distribution, we are able to create spectra that produce a positive spectral slope for NIR flares, as reported by Hornstein et al. [2007] and Dodds-Eden et al. [2009].

Due to our small change in electron distribution in the best-bet accretion flow model of Mościbrodzka, et al. [2009], the modified best-bet model still agrees with all the observational constraints. However, we make no claim that the old best-bet model provide the best fit if flaring data are taken into account. In fact, we argue that it is not possible to further constrain the problem, both due to the large number of parameters in the power-law models, and the degeneracy among the parameters.

4.9 References

An, T., et al. 2005, ApJ, 634, L49

Baganoff, F. K., et al. 2001, Nature, 413, 45

Baganoff, F. K., et al. 2003, ApJ, 591, 891

Beckwith, K., Hawley, J. F., & Krolik, J. H. 2008, MNRAS, 390, 21

Blumenthal, G. R., & Gould, R. J. 1970, Rev. Mod. Phys., 42, 237

Canfield, E., Howard, W. M., & Liang, E. P. 1987, ApJ, 323, 565

Chandrasekhar, S. 1957, An Introduction to the Study of Stellar Structure (New York: Dover)

Chan, C.-K., Liu, S., Fryer, C. L., Psaltis, D., Özel, F., Rockefeller, G., Melia, F. 2009, ApJ, 701, 521

Dexter, J., et al. 2010, ApJ, 717, 1092

Dodds-Eden, K., et al. 2009, ApJ, 698, 676

Dolence, J. C., Gammie, C. F., Mościbrodzka, M., & Leung, P. K. 2009, ApJS, 184, 387

Eisenhauer, F., et al. 2005, ApJ, 628, 246

Falcke, H., et al. 1998, ApJ, 499, 731

Fishbone, L. G., & Moncrief, V. 1976, ApJ, 207, 962

Galassi, M., et al. 2006 GNU Scientific Library Reference Manual (2nd ed.), `http://www.gnu.org/software/gsl/`

Gammie, C. F., & Popham, R. 1998, ApJ, 498, 313

Gammie, C. F., McKinney, J. C., & Tóth, G. 2003, ApJ, 589, 444

Genzel, R., et al. 2003, Nature, 425, 934

Ghez, A. M., et al. 2003, ApJ, 586, L127

Ghez, A. M., et al. 2005, ApJ, 635, 1087

Heitler, W. 1954, The Quantum Theory of Radiation (3rd ed.; London: Oxford)

Hornstein, S. D., et al. 2007, ApJ, 667, 900

Kardashev, N. S. 1962, Sov. Astron., 6, 317

Krabbe, A., et al. 2006, J. Phys. Conf. Ser., 54, 406

Leung, P. K., Gammie, C. F., & Noble, S. C. 2009, ApJ, submitted

Leung, P. K., et al. 2010, in preparation

Marrone, D. P., et al. 2006, J. Phys. Conf. Ser., 54, 354

Melia, F., & Falcke, H. 2001, ARA&A, 39, 309

Mościbrodzka, M., Gammie, C. F., Dolence, J. C., Shiokawa, H., & Leung, P. K. 2009, ApJ, 706, 497

Mościbrodzka, M., et al. 2010, in preparation

Narayan, R., Yi, I., & Mahadevan, R. 1995, Nature, 374, 623

Ohsuga, K., Kato, Y., & Mineshige, S. 2005, ApJ, 627, 782

Özel, F., Psaltis, D., & Narayan, R. 2000, ApJ, 541, 234

Pozdnyakov, L. A., Sobol', I. M., & Syunyaev, R. A. 1983, ASPRv, 2, 189

Rybicki, G. B., & Lightman, A. P. 1979, Radiative Processes in Astrophysics (New York: John Wiley & Sons)

Schödel, R., et al. 2002, Nature, 419, 694

Schödel, R. et al. 2007, A&A, 462, L1

Stix, T. H. 1992, Waves in Plasmas (New York: AIP)

Yuan, F., Quataert, E., & Narayan, R. 2003, ApJ, 598, 301

Chapter 5

A Formalism for Covariant Polarized Radiative Transport by Ray Tracing

5.1 Introduction

Polarization data is now available at many wavelengths for Sgr A*, the radio, millimeter, infrared, and X-ray source at the galactic center. Polarization characteristics have already provided interesting constraints on models that site the source in a hot plasma surrounding a $4 \times 10^6 M_\odot$ black hole [Aitken et al., 2000, Marrone et al., 2006, 2007], and may provide more constraints with the aid of appropriate models. We set out to model the polarization of Sgr A*, and in the process have developed the argument below that describes a procedure for solving the polarized radiative transfer equation in a curved spacetime. There are many other possible applications of this work, however, including neutron star atmospheres, pulsar magnetospheres, other galactic nuclei, and even cosmological problems.[1]

Work on covariant unpolarized radiative transport began with Lindquist [1966], although there were earlier studies of the Boltzmann equation in covariant form. Later work by Anderson & Spiegel [1972], and then by Thorne [1981], extended this to a formalism in which the angular (momentum space) structure of the radiation field is described by a moment formalism, again for unpolarized radiation.

Work by Connors, Piran & Stark [1980] transported *polarized* radiation from its origin on the surface of a thin disk near a black hole through vacuum to an observer at large radius by parallel transporting the polarization vector along a geodesic (more recent works by, e.g., Schnittman & Krolik [2009], Dovčiak et al. [2008] and Li et al. [2005], use a similar procedure, although Schnittman & Krolik [2009] include Compton scattering).

The first clear description of fully relativistic polarized radiative transport that we are aware of is by Bildhauer [1989a,b], who wrote down a transport equation for a vector potential polarization tensor (we will use the same procedure); Bildhauer

[1]This work will be submitted to ApJ [Gammie & Leung, 2010]. Reproduction for this dissertation is authorized by the copyright holder.

[1989a,b]'s work built on earlier work by Dautcourt & Rose [1978]. Later polarized transport equations were written down in a cosmological context by Kosowsky [1994, 1996], Challinor [2000], and Weinberg [2008, Appendix]. More recently, Broderick & Blandford [2004, hereafter BB04] have developed an elegant formalism for treating transport along a ray, and this has been applied by, e.g., Broderick, Loeb & Narayan [2009] and Huang et al. [2009] to models of Sgr A*.

If a covariant polarized transport formalism exists, why are we revisiting the issue? Most earlier work describes the polarized radiation field in terms of dependent variables, like the invariant Stokes parameters $Q/\nu^3, U/\nu^3, V/\nu^3$, which are frame dependent. The way these variables change along a geodesic depends on how the chosen frame changes along the geodesic. In many applications this is unobjectionable; there is a natural choice of frames (e.g., in cosmology) that varies slowly along the geodesic. In accretion flow problems, however, the natural (plasma) frame fluctuates rapidly along the geodesic because of turbulence in the underlying flow. The Stokes parameters can then fluctuate, even if there is no interaction between the plasma and the radiation field. This seems unsatisfactory. The procedure we describe below is manifestly frame independent and avoids this issue.

A second motivation is that the widely used BB04 formalism is written down from physical arguments but not derived. It was not clear (to us) that all relativistic effects were properly included in BB04's treatment. Here we derive BB04's equations starting from the firm ground of Maxwell's equations and the Liouville-Vlasov equation.

A third motivation is that the use of preferred observers seems inelegant. It ought to be possible to define a tensor quantity to represent the polarized radiation field and then write the basic equations in a coordinate and frame independent way at the outset. One manifestly covariant description of a polarized radiation field is

$$Q_{\alpha\beta\gamma\delta} = \langle F_{\alpha\beta} F^*_{\gamma\delta} \rangle, \tag{5.1}$$

where $F_{\alpha\beta}$ is the electromagnetic field tensor and * denotes complex conjugate. This unwieldy fourth-rank polarization tensor has 21 real (not complex) degrees of freedom, most of which are redundant due to the radiative character of the electromagnetic field. A simpler but still covariant description of the radiation field is

$$N_{\alpha\beta} = \langle A_\alpha A^*_\beta \rangle, \tag{5.2}$$

where A_μ is the four-vector potential, with $F_{\alpha\beta} = \partial_\alpha A_\beta - \partial_\beta A_\alpha$. This is the fundamental description of the radiation field used by Bildhauer [1989a,b]. Some of the

components of $N_{\alpha\beta}$ have a natural interpretation as a photon phase space density and obey a simple equation along photon trajectories. Other components represent extra (gauge) degrees of freedom that can be clearly identified and that are eliminated when a final physical measurement is made by projecting $N_{\alpha\beta}$ onto an appropriate tetrad basis.

A final motivation is pedagogical: we want to make the transition from familiar territory—Maxwell's equations—to a covariant polarized transfer equation with a minimum of technical overhead.

We adopt the standard notation of Misner, Thorne & Wheeler [1973, hereafter MTW] including a signature for the metric of $\{-,+,+,+\}$. We set $c = 1$ except where specifically noted otherwise. It may help to recall that, if x^μ is a set of coordinate and k_μ is a wave four-vector then the following are coordinate invariant: $d^3k/(\sqrt{-g}k^t)$ (here g is the determinant of $g_{\mu\nu}$); $d^3x\sqrt{-g}k^t$; d^3xd^3k (phase space volume). Here $d^3k = dk_1dk_2dk_3$ and $d^3x = dx^1dx^2dx^3$, where $1, 2, 3$ are spacelike coordinates.

Our paper is organized as follows. In §2 we review the properties of WKB solutions for electromagnetic wavetrains in a vacuum spacetime. In §3 we give an explicit expression for an orthonormal tetrad frame and define a polarization tensor for wavetrains. In §4 we discuss WKB solutions for a WKB wavetrain in a dilute test (nonself-gravitating) plasma. In §5 we make the transition to an ensemble of wave packets (photons) from a wavetrain and write a Boltzmann equation for the polarization tensor $N^{\mu\nu}$ that accounts for absorption and emission. In §6 we describe how to connect $N^{\mu\nu}$ to Stokes parameters. In §7 we explain how our emission and absorption tensors relate to more familiar emissivities and absorptivities, and relate it to expressions in Leung, Gammie & Noble [2009] and Shcherbakov [2008]. In §8 we explicitly demonstrate that the resulting evolution of the invariant Stokes parameters (Stokes parameters/ν^3) are gauge invariant. In §9 we write the polarization equation in a tetrad basis and define a set of rotation coefficients. In §10 we explicitly demonstrate that our equation is consistent with the formalism given by BB04. In §11 we describe strategies for integrating the Boltzmann equation along a ray. In §12 we give a brief summary.

5.2 WKB wavetrain review

Consider a single electromagnetic wavetrain given by

$$A_\mu(x^\nu) = a_\mu(x^\nu)\exp(ik_\alpha x^\alpha) \tag{5.3}$$

where a_μ is an amplitude and $k_\alpha = \partial_\alpha \theta$ (θ is the phase) is, as usual in WKB, the wavevector.[2] The Lorenz gauge condition $\nabla_\mu A^\mu = 0$ implies to leading order in WKB that

$$k_\mu a^\mu = 0. \tag{5.4}$$

The Lorenz gauge does *not* fix A^μ uniquely, since we can always send $A^\mu \to A^\mu + \phi(x^\nu)k^\mu$.

Maxwell's equations in the Lorenz gauge imply (MTW, Eq. (22.19d))

$$\nabla^\alpha \nabla_\alpha A^\mu + R^\mu_\alpha A^\alpha = 4\pi J^\mu. \tag{5.5}$$

where J^μ is the current (see Jackson [1975, p. 551] for covariant form in Gaussian units) and $R^{\mu\nu}$ is the Ricci tensor. If the plasma is diffuse (a "test plasma") then the stress-energy tensor $T^{\mu\nu} \approx 0$ and Einstein's equations give $R^{\mu\nu} \approx 0$. Suppose for now that $J^\mu = 0$; then

$$\nabla^\alpha \nabla_\alpha A^\mu = 0. \tag{5.6}$$

In the WKB approximation this yields at lowest order (MTW §22.5)

$$k^\mu k_\mu = 0 \tag{5.7}$$

or, in nonrelativistic language, $\omega^2 = c^2 k^2$. Rewriting Eq. (5.7) as $\nabla^\mu \theta \nabla_\mu \theta$ yields after taking the gradient and interchanging indices

$$k^\mu \nabla_\mu k^\nu = 0. \tag{5.8}$$

To next order in WKB one obtains an evolution equation for the vector Fourier amplitudes:

$$k^\mu \nabla_\mu a^\nu + \frac{1}{2} a^\nu \nabla_\mu k^\mu = 0. \tag{5.9}$$

The amplitude evolution equation can be decomposed into an equation for the scalar amplitude $a = (a_\mu a^\mu)^{1/2}$ and for the polarization unit vector $f_\mu = a_\mu / a$:

$$k^\mu \nabla_\mu a + \frac{1}{2} a \nabla_\mu k^\mu = 0. \tag{5.10}$$

and

$$k^\mu \nabla_\mu f^\nu = 0. \tag{5.11}$$

[2]The sign convention for k_μ is opposite that in Melrose [2008, 2009]; we use signature $-+++$ for the metric instead of Melrose's $+---$.

The scalar amplitude equation can be rewritten

$$\nabla_\mu(k^\mu a^2) = 0 \tag{5.12}$$

i.e. as a conservation equation for a^2.

How are physical measurements made from a^μ? First, the electromagnetic field tensor is

$$F_{\mu\nu} = \partial_\mu A_\nu - \partial_\nu A_\mu \tag{5.13}$$

which to lowest order in WKB is [3]

$$F_{\mu\nu} = i(k_\mu a_\nu - k_\nu a_\mu). \tag{5.14}$$

This can be decomposed into an E and B field in a particular frame u^μ. The electric field four-vector is

$$E^\mu \equiv u_\nu F^{\mu\nu} = i(k^\mu(a_\nu u^\nu) - a^\mu(k_\nu u^\nu)), \tag{5.15}$$

This definition is consistent with the Lorentz force $du^\alpha/d\tau = (q/m)u_\beta F^{\alpha\beta}$. The magnetic field four-vector is

$$B^\mu = u_\nu \, {}^*F^{\nu\mu} \tag{5.16}$$

where

$${}^*F^{\mu\nu} = \frac{1}{2}\epsilon^{\mu\nu\kappa\lambda}F_{\kappa\lambda} \tag{5.17}$$

and

$$\epsilon^{\mu\nu\kappa\lambda} = -\frac{1}{\sqrt{-g}}[\mu\nu\kappa\lambda], \tag{5.18}$$

and $[\mu\nu\kappa\lambda]$ is the permutation symbol (1 for even permutations of 0123, -1 for odd permutations, zero otherwise). E^μ and B^μ reduce to the usual E and B fields in an orthonormal tetrad that is at rest in the u^μ frame. They are both orthogonal to

$$K^\mu = (g^\mu_\nu + u^\mu u_\nu)k^\nu = k^\mu + u^\mu(u_\nu k^\nu) \tag{5.19}$$

which is the spatial part of k^μ.

The stress-energy tensor for a wavetrain is (MTW):

$$T^{\mu\nu}_{WT} = \frac{1}{8\pi}a^2 k^\mu k^\nu \tag{5.20}$$

[3] Again, the sign is opposite Melrose [2008, 2009].

from which we see that in a particular coordinate frame the energy density

$$T^{tt} = \frac{1}{\sqrt{-g}}\frac{dE}{d^3x} = \frac{1}{8\pi}k^t k^t a^2 \tag{5.21}$$

and, since photon number $dE = \hbar k^t dN$ the photon number density is

$$\frac{1}{\sqrt{-g}}\frac{dN}{d^3x} = \frac{1}{8\pi\hbar}k^t a^2 \tag{5.22}$$

(again MTW p. 580), which implies that the invariant photon number density is

$$\frac{1}{\sqrt{-g}k^t}\frac{dN}{d^3x} = \frac{a^2}{8\pi\hbar}, \tag{5.23}$$

since $\sqrt{-g}k^t d^3x$ is invariant.

5.3 Polarization Tensors

We first erect a tetrad frame—which we will refer to as the plasma basis—to simplify the discussion of polarization tensors.

5.3.1 Plasma tetrad

It is natural to erect a tetrad that moves with the plasma, $e^\alpha_{(t)} = u^\alpha$ and has one basis vector $e^\alpha_{(K)}$ parallel to K^α. The other basis vectors are then fixed up to a rotation. For radiative transfer in a magnetized plasma it is natural to use the magnetic field four-vector b^μ to uniquely specify the orientation of the remaining basis vectors (BB04), but any trial spacelike four-vector b^μ not aligned with K^α will do.

Gram-Schmidt orthogonalization yields the following explicit expressions for the spatial basis vectors:

$$e^\alpha_{(K)} = \frac{K^\alpha}{\sqrt{K^\mu K_\mu}} = -\left(\frac{k^\alpha}{k_\mu u^\mu} + u^\alpha\right) \tag{5.24}$$

$$e^\alpha_{(\parallel)} = \frac{b^\alpha + \frac{k_\nu b^\nu}{k_\mu u^\mu}e^\alpha_{(K)}}{(b^2 - ((k_\lambda b^\lambda)/(k_\kappa u^\kappa))^2)^{1/2}} \tag{5.25}$$

$$e^\alpha_{(\perp)} = \epsilon^{\alpha\beta\gamma\delta}e^{(t)}_\delta e^{(K)}_\gamma e^{(\parallel)}_\beta = \frac{\epsilon^{\alpha\beta\gamma\delta}u_\delta k_\gamma b_\beta}{(b^2(k_\kappa u^\kappa)^2 - (k_\lambda b^\lambda)^2)^{1/2}} \tag{5.26}$$

Notice that $e^\alpha_{(t)}a_\alpha = a_\beta u^\beta$ and $e^\alpha_{(K)}a_\alpha = -a_\beta u^\beta$. It is straightforward to confirm that

$e^{\alpha}_{(a)} e^{(b)}_{\alpha} = \delta^{(b)}_{(a)}$. This basis is identical to that given in BB04.

5.3.2 Polarization tensors

The usual electric polarization tensor is

$$P^{\mu\nu} = E^{\mu} E^{*\nu}, \tag{5.27}$$

but this does not obey a simple transport equation (see, e.g., the discussion of Portsmouth & Bertschinger 2004). Let us calculate $P^{(a)(b)}$, the polarization tensor in the plasma basis. Since

$$e^{\alpha}_{(t)} E_{\alpha} = 0, \tag{5.28}$$

which follows from Eq. (5.15), or directly from the antisymmetry of $F^{\mu\nu}$,

$$e^{\alpha}_{(K)} E_{\alpha} = 0, \tag{5.29}$$

which follows from Eq. (5.15) and the Lorenz gauge condition;

$$e^{\alpha}_{(\parallel)} E_{\alpha} = i \left(k_{\beta} u^{\beta}\right) e^{\alpha}_{(\parallel)} a_{\alpha} \tag{5.30}$$

which follows from $e^{\alpha}_{(K)} E_{\alpha} = 0$; and

$$e^{\alpha}_{(\perp)} E_{\alpha} = i \left(k_{\beta} u^{\beta}\right) e^{\alpha}_{(\perp)} a_{\alpha}. \tag{5.31}$$

Therefore the only nonzero components of the electric field are perpendicular to K^{μ} and u^{μ}.

We now introduce the notation (A) (capitalized roman index in parentheses) for a tetrad component normal to both u^{μ} and k^{μ}, here either $(\perp)$ or $(\parallel)$. Then

$$P^{(A)(B)} = e^{(A)}_{\mu} e^{(B)}_{\nu} P^{\mu\nu} = (k_{\beta} u^{\beta})^2 e^{(A)}_{\mu} e^{(B)}_{\nu} a^{\mu} a^{*\nu}. \tag{5.32}$$

This motivates the definition of the polarization tensor

$$N^{\mu\nu} = \langle a^{\mu} a^{*\nu} \rangle. \tag{5.33}$$

which is independent of the frame u^{μ}. From §2 it is apparent that N^{μ}_{μ} is proportional to the photon phase space density for a wavetrain. If a^{μ} is expressed in gauss-cm, then the photon number density is $N^{\mu}_{\mu}/(8\pi\hbar c)$.

$N^{\mu\nu}$ is gauge dependent; sending $a^\mu \to a^\mu + \phi k^\mu$ doesn't change any measurements. This final gauge freedom can be eliminated by setting $u^\mu a_\mu = 0$ at any point along the ray and then parallel transporting a_μ.

5.4 Wavetrain in a plasma

Now consider the wave equation for a wavetrain in a plasma. The wave equation in the presence of a test-plasma (one that does not contribute to the gravitational field, so that $R_{\mu\nu} = 0$) is (MTW)

$$\nabla_\mu \nabla^\mu A^\alpha = 4\pi(J^\alpha_{\rm ind} + J^\alpha_{\rm ext}), \tag{5.34}$$

where $J^\alpha_{\rm ind}$ and $J^\alpha_{\rm ext}$ are the "induced" and "extraneous" 4-currents (corresponding to absorption and generalized Faraday rotation, and emission respectively). The linear response tensor Π is

$$J^\alpha_{\rm ind} \equiv \Pi^\alpha_\beta A^\beta. \tag{5.35}$$

The response tensor is gauge independent since $E^\mu = i(k^\mu u^\nu - (k_\beta u^\beta) g^{\mu\nu})a_\nu$, and the induced current is uniquely related to the electric field.

The wave equation, at lowest order in WKB and without the extraneous 4-current, is now

$$-2ik^\beta \nabla_\beta a^\alpha - i a^\alpha \nabla_\beta k^\beta = 4\pi \Pi^\alpha_\beta a^\beta \tag{5.36}$$

or (multiplying by i)

$$2k^\beta \nabla_\beta a^\alpha + a^\alpha \nabla_\beta k^\beta = 4\pi i \Pi^\alpha_\beta a^\beta. \tag{5.37}$$

or

$$k^\beta \nabla_\beta a^\alpha = -\frac{1}{2} a^\alpha \nabla_\beta k^\beta + 2\pi i \Pi^\alpha_\beta a^\beta. \tag{5.38}$$

Now expand $\nabla_\mu(k^\mu a^\alpha a^{*\beta})$

$$\nabla_\mu(k^\mu a^\alpha a^{*\beta}) = a^{*\beta} k^\mu \nabla_\mu a^\alpha + a^\alpha k^\mu \nabla_\mu a^{*\beta} + a^\alpha a^{*\beta} \nabla_\mu k^\mu \tag{5.39}$$

and evaluate it using the wave equation:

$$\nabla_\mu(k^\mu a^\alpha a^{*\beta}) = 2\pi i \left(a^{*\beta} \Pi^\alpha_\mu a^\mu - a^\alpha \Pi^{*\beta}_\mu a^{*\mu} \right) \tag{5.40}$$

which we rewrite as

$$\nabla_\mu(k^\mu a^\alpha a^{*\beta}) = H^{\alpha\beta\kappa\lambda} a_\kappa a^*_\lambda \tag{5.41}$$

with

$$H^{\alpha\beta\kappa\lambda} \equiv 2\pi i \left(g^{\beta\lambda}\Pi^{\alpha\kappa} - g^{\alpha\kappa}\Pi^{*\beta\lambda} \right). \tag{5.42}$$

Contracting over α and β,

$$\nabla_\mu (k^\mu a^2) = 2\pi i (\Pi^{\lambda\kappa} - \Pi^{*\kappa\lambda}) a_\kappa a^*_\lambda. \tag{5.43}$$

Since a^2 is proportional to the photon number density, this shows that absorption is encoded in the anti-hermitian part of Π.

5.5 Ensemble of waves: a_k^2

We now want to make the transition from WKB wave trains, which are approximately a δ function in momentum space, to a transport equation for a distribution of photons in momentum space.

Consider a small, invariant spatial volume $\Delta V = \Delta^3 x \sqrt{-g} k^t$ and a small, invariant momentum space volume $\Delta V_k = \Delta^3 k / (\sqrt{-g} k^t)$. Populate the phase space volume $\Delta V \Delta V_k$ with an ensemble of wave packets labeled by i, and model each packet as a wave train with definite amplitude a_i.

Define the photon distribution function

$$f \equiv \frac{dN}{d^3x d^3k} \approx \frac{1}{\Delta V_k} \sum_i \frac{1}{\sqrt{-g} k^t} \frac{dN_i}{d^3x} \tag{5.44}$$

This is invariant since $d^3k/(\sqrt{-g}k^t)$ is invariant (here $d^3k = dk_1 dk_2 dk_3$, i.e. indices are down). The distribution function is recovered in the limit $\Delta V_k \to 0$.

The photon number density is quadratic in A_μ. Recall that

$$A_\mu = \sum_j a_{j\mu} e^{i k_{j\nu} x^\nu} \tag{5.45}$$

so

$$A_\mu A^*_\nu = \sum_{ij} a_{i\mu} a^*_{j\nu} e^{i(k_{i\nu} - k_{j\nu}) x^\nu}. \tag{5.46}$$

If the phases of the wave packets are uncorrelated (the radiation is incoherent) the cross terms vanish and

$$\langle A_\mu A^*_\nu \rangle = \sum_i \langle a_{i\mu} a^*_{i\nu} \rangle \tag{5.47}$$

where the $\langle\rangle$ is a suitable average (Bildhauer [1989a] makes this step carefully using

Wigner transforms). From now on we drop the explicit $\langle\rangle$.

The wavetrain analysis implies that

$$\frac{1}{\Delta V_k}\sum_i \frac{1}{\sqrt{-g}k^t}\frac{dN_i}{d^3x} = \frac{1}{\Delta V_k}\sum_i \frac{a_i^2}{8\pi\hbar c}. \tag{5.48}$$

This motivates the definition of power spectrum

$$a_k^2 \equiv \frac{1}{\Delta V_k}\sum_i a_i^2. \tag{5.49}$$

Then

$$f = \frac{a_k^2}{8\pi\hbar}, \tag{5.50}$$

and so (reinserting the correct powers of c)

$$I_\nu = \frac{h^4\nu^3}{c^2}f = \frac{h^4\nu^3}{c^2}\frac{a_k^2}{8\pi\hbar c} = \frac{\epsilon^3}{c^3}\frac{a_k^2}{4} \tag{5.51}$$

where $\epsilon = h\nu$ is the individual photon energy. One of the factors of 2 here comes from averaging over a wavelength.

Now invoke the Liouville-Vlasov equation, which for photons *in vacuo* implies

$$\frac{df}{d\lambda} = 0 \quad \Rightarrow \quad \frac{d(I_\nu/\nu^3)}{d\lambda} = 0, \tag{5.52}$$

or

$$\frac{da_k^2}{d\lambda} = k^\mu\nabla_\mu\, a_k^2 = 0 \tag{5.53}$$

and demand consistency with Maxwell's equations. Recasting in terms of the wave amplitudes

$$k^\mu\nabla_\mu\left(\frac{1}{\Delta V_k}\sum_i a_i^2\right) = 0, \tag{5.54}$$

and expanding,

$$\sum_i\left(\frac{1}{\Delta V_k}(k^\mu\nabla_\mu)a_i^2 - \frac{a_i^2}{\Delta V_k^2}(k^\mu\nabla_\mu)\Delta V_k\right) = 0. \tag{5.55}$$

Applying the wave equation to this gives

$$-a_k^2\left(\nabla_\mu k^\mu + k^\mu\nabla_\mu \ln\Delta V_k\right) = 0 \tag{5.56}$$

The first term in parentheses is the fractional rate of change of the invariant three-volume $\Delta V = \Delta^3 x \sqrt{-g} k^t$ occupied by a group of photons in the wave (exercise 22.1 of MTW), i.e. it is $d \ln \Delta V / d\lambda = (k^\mu \nabla_\mu) \ln \Delta V$. Then

$$k^\mu \nabla_\mu \ln \Delta V + k^\mu \nabla_\mu \ln \Delta V_k \propto \frac{d}{d\lambda}(\Delta V \Delta V_k) = 0, \tag{5.57}$$

that is, along a photon trajectory the phase space volume $\Delta V \Delta V_k$ occupied by the group of photons is constant.

Maxwell and Liouville permitted us to evaluate $d\Delta V_k / d\lambda$, which in turn implies

$$(k^\alpha \nabla_\alpha) \langle a_{k\mu} a^*_{k\nu} \rangle = 0 \tag{5.58}$$

in vacuum. Define the (Hermitian) polarization tensor

$$N^{\mu\nu} = \langle a^\mu_k a^{*\nu}_k \rangle, \tag{5.59}$$

where from now on we will drop the explicit k subscript. Then

$$(k^\alpha \nabla_\alpha) N^{\mu\nu} = 0 \tag{5.60}$$

in vacuum. This result is identical at lowest order to Bildhauer [1989a]'s, although for Bildhauer [1989a] the independent variables are x^μ, k_μ rather than λ.

The classical wave equation in a plasma can then be used to write a polarized transport equation with absorption and Faraday rotation:

$$k^\alpha \nabla_\alpha N^{\mu\nu} = H^{\mu\nu\kappa\lambda} N_{\kappa\lambda}. \tag{5.61}$$

If we add back the source terms the Boltzmann equation becomes

$$k^\alpha \nabla_\alpha N^{\mu\nu} = J^{\mu\nu} + H^{\mu\nu\kappa\lambda} N_{\kappa\lambda}, \tag{5.62}$$

Eq. (5.62) is a covariant polarized radiative transfer equation. Scattering may likewise be accounted for by adding a scattering tensor to the right hand side.

5.6 Stokes from $N^{\mu\nu}$

How does $N^{\mu\nu}$ related to Stokes I, Q, U, V? We know that $I_\nu = \epsilon^3 a_k^2/(4c^3)$. Then in the plasma basis the four components of $N^{(A)(B)}$ are

$$N^{(A)(B)} = e_\mu^{(A)} e_\nu^{(B)} N^{\mu\nu} = \frac{2c^3}{\epsilon^3} \begin{pmatrix} I+Q & U+iV \\ U-iV & I-Q \end{pmatrix}. \tag{5.63}$$

Thus $I \propto N^{(\perp)(\perp)} + N^{(\parallel)(\parallel)}$, $Q \propto N^{(\parallel)(\parallel)} - N^{(\perp)(\perp)}$, $U \propto N^{(\perp)(\parallel)} + N^{(\parallel)(\perp)}$, and $V \propto -i(N^{(\perp)(\parallel)} - N^{(\parallel)(\perp)})$.

What scalars can be formed from $N^{\mu\nu} = N^{*\nu\mu}$? If we separate N into symmetric (real) and antisymmetric (imaginary) parts, the trace of the symmetric part is proportional to I, the term by term square is proportional to $(I^2 + Q^2 + U^2)$, the trace of the antisymmetric part is zero (of course!), and the term by term square of the antisymmetric part is proportional to V^2. There are no other scalars. No invariant procedure can allow us to separately determine Q and U or the sign of V, as these are manifestly coordinate-dependent quantities.

5.7 Emission and absorption

5.7.1 Response tensor

The response tensor $\Pi^{\alpha\beta}$ can be constructed from the response 3-tensor by identifying the corresponding terms in the tensor and using the charge-continuity and gauge-invariance conditions [Melrose, 2008, §1.5.8]. Another way to proceed is to decompose the response tensor into the hermitian (h) and antihermitian (a) parts, such that

$$\Pi^{\alpha\beta} = \Pi_{\rm h}^{\alpha\beta} + \Pi_{\rm a}^{\alpha\beta} \tag{5.64}$$

where

$$\Pi_{\rm h}^{\alpha\beta} = \frac{1}{2}(\Pi^{\alpha\beta} + \Pi^{*\beta\alpha}) \ , \quad \Pi_{\rm a}^{\alpha\beta} = \frac{1}{2}(\Pi^{\alpha\beta} - \Pi^{*\beta\alpha}). \tag{5.65}$$

The hermitian part conserves total energy in the wave whereas the antihermitian part causes dissipation. It is then natural to rewrite Eq. (5.42) as

$$H^{\alpha\beta\kappa\lambda} = A^{\alpha\beta\kappa\lambda} + R^{\alpha\beta\kappa\lambda} \tag{5.66}$$

where the absorption part

$$A^{\alpha\beta\kappa\lambda} \equiv 2\pi i(g^{\beta\lambda}\Pi_{\rm a}^{\alpha\kappa} - g^{\alpha\kappa}\Pi_{\rm a}^{\lambda\beta}) \equiv \frac{1}{2}(g^{\beta\lambda}A^{\alpha\kappa} - g^{\alpha\kappa}A^{\lambda\beta}) \tag{5.67}$$

contains the dissipative terms, and the generalized Faraday rotation part

$$R^{\alpha\beta\kappa\lambda} \equiv 2\pi i(g^{\beta\lambda}\Pi_{\rm h}^{\alpha\kappa} + g^{\alpha\kappa}\Pi_{\rm h}^{\lambda\beta}) \equiv \frac{1}{2}(g^{\beta\lambda}R^{\alpha\kappa} + g^{\alpha\kappa}R^{\lambda\beta}) \tag{5.68}$$

contains the non-dissipative terms. Due to the symmetry properties, $A^{\alpha\beta\kappa\lambda}$ has 4 degrees of freedom while $R^{\alpha\beta\kappa\lambda}$ has 3 degrees of freedom.

In flat space, one can write the radiative transfer equation as

$$\frac{d}{ds}I_S = J_S - \mathbf{M}_{ST}I_T, \tag{5.69}$$

where $I_S = \{I, Q, U, V\}$ contains the Stokes parameters, $J_S = \{j_I, j_Q, j_U, j_V\}$ contains the emission coefficients, which have units of $dE/dtdVd\nu d\Omega$, and the Mueller Matrix $\mathbf{M}_{ST}$ is

$$\mathbf{M}_{ST} \equiv \begin{pmatrix} \alpha_I & \alpha_Q & \alpha_U & \alpha_V \\ \alpha_Q & \alpha_I & r_V & -r_U \\ \alpha_U & -r_V & \alpha_I & r_Q \\ \alpha_V & r_U & -r_Q & \alpha_I \end{pmatrix}. \tag{5.70}$$

The parameters α_i are the absorption coefficients and r_Q, r_U and r_V are the Faraday mixing coefficients. By comparing the terms in Eqs. (5.69) and (5.62) in a tetrad basis $e^\mu_{(t)}$, $e^\mu_{(\parallel)}$, $e^\mu_{(\perp)}$ and $e^\mu_{(K)}$, one can write

$$A^{(a)(b)} \equiv \epsilon \begin{pmatrix} 0 & 0 & 0 & 0 \\ 0 & \alpha_I + \alpha_Q & \alpha_U + i\alpha_V & 0 \\ 0 & \alpha_U - i\alpha_V & \alpha_I - \alpha_Q & 0 \\ 0 & 0 & 0 & 0 \end{pmatrix} \tag{5.71}$$

and

$$R^{(a)(b)} \equiv -i\epsilon \begin{pmatrix} 0 & 0 & 0 & 0 \\ 0 & r_Q & r_U + ir_V & 0 \\ 0 & r_U - ir_V & -r_Q & 0 \\ 0 & 0 & 0 & 0 \end{pmatrix}. \tag{5.72}$$

Expressions for magnetobremsstrahlung absorption coefficients can be found in Eq. (48) Leung, Gammie & Noble [2009], and formulae for the Faraday mixing coefficients in

Eq. (33) [4] of Shcherbakov [2008].

5.7.2 Emissivity tensor

The emissivity tensor can be written in Stokes basis as

$$J^{(i)(j)} \equiv \frac{2c^3}{\epsilon^2} \begin{pmatrix} 0 & 0 & 0 & 0 \\ 0 & j_I + j_Q & j_U + ij_V & 0 \\ 0 & j_U - ij_V & j_I - j_Q & 0 \\ 0 & 0 & 0 & 0 \end{pmatrix}, \tag{5.73}$$

Expressions for the magnetobremsstrahlung emissivities are given by Eq. (28) of Leung, Gammie & Noble [2009].

5.8 Gauge Invariance

Here we show by explicit calculation that the gauge freedom ϕ does not affect $N^{(A)(B)}$ where as before $(A), (B)$ are the components of N projected into the space perpendicular to the observer four-velocity u^μ and wavevector k^μ. $N^{(A)(B)}$ are quantities that can be measured. Along the way we explicitly identify and count the degrees of freedom in $N^{\mu\nu}$. We also show that inconsistent definition of the gauge freedom ϕ from frame to frame do not affect the measured Stokes parameters.

First construct an explicit expression for the $N^{(a)(b)}$. Consider a Cartesian tetrad attached to an observer with velocity v^μ. The tetrad components are $e_{(K)}$ and $e_{(t)}$ are defined just as for the plasma frame; the other two components $e_{(x)}$ and $e_{(y)}$ are only defined up to a rotation. Let $a^{(a)} = \{\phi K, a_x, a_y, \phi K\}$ and $k^{(a)} = K\{1, 0, 0, 1\}$, consistent with the Lorenz gauge condition $k^\mu a_\mu = 0$. In this frame

$$N^{\mu\nu} = \begin{Bmatrix} K^2\langle\phi\phi^*\rangle & K\langle\phi a_x^*\rangle & K\langle\phi a_y^*\rangle & K^2\langle\phi\phi^*\rangle \\ K\langle a_x\phi^*\rangle & \langle a_x a_x^*\rangle & \langle a_x a_y^*\rangle & K\langle a_x\phi^*\rangle \\ K\langle a_y\phi^*\rangle & \langle a_y a_x^*\rangle & \langle a_y a_y^*\rangle & K\langle a_y\phi^*\rangle \\ K^2\langle\phi\phi^*\rangle & K\langle\phi a_x^*\rangle & K\langle\phi a_y^*\rangle & K^2\langle\phi\phi^*\rangle \end{Bmatrix}, \tag{5.74}$$

where the average is over many wave packets in an infinitesimal volume of phase space. Since the wave packets can have different ϕ, the correlations involving ϕ are nontrivial, so, e.g., $\langle\phi\phi^*\rangle\langle a_x a_y^*\rangle$ need not equal $\langle\phi a_y^*\rangle\langle a_x\phi^*\rangle$, just as $\langle a_y a_x^*\rangle\langle a_x a_y^*\rangle$ need

[4] Note the sign difference in Eq. (32) of Shcherbakov [2008] compared to our equations.

not equal $\langle a_x a_x^* \rangle \langle a_y a_y^* \rangle$ and I^2 need not equal $Q^2 + U^2 + V^2$.

$N^{\mu\nu}$ is Hermitian and so has 16 real degrees of freedom. Four of these are the Stokes parameters, contained in $N^{(A)(B)}$. There are four additional degrees of freedom in $\langle \phi a_x^* \rangle$ and $\langle \phi a_y^* \rangle$. The remaining eight degrees of freedom are eliminated by the four complex conditions $k_\mu N^{\mu\nu} = 0$.

How does $N^{(A)(B)}$ transform to another tetrad? Consider a second tetrad attached to an observer with four-velocity u^μ; the basis vectors are $\bar{e}^\mu_{(t)}$ $\bar{e}^\mu_{(x)}$ $\bar{e}^\mu_{(y)}$, and $\bar{e}^\mu_{(K)}$. Recall that $\bar{e}^\mu_{(t)} = u^\mu$ and $\bar{e}^\mu_{(K)} = -[k^\mu/(k_\alpha u^\alpha) + u^\mu]$. Writing out the transformation explicitly,

$$\bar{N}_{(A)(B)} = \bar{e}^\mu_{(A)} \bar{e}^\nu_{(B)} e^{(c)}_\mu e^{(d)}_\nu N_{(c)(d)}. \tag{5.75}$$

Expanding,

$$\bar{e}^\mu_{(A)} e^{(c)}_\mu N_{(c)(d)} = \bar{e}^\mu_{(A)} \left(e^{(t)}_\mu N_{(t)(d)} + e^{(K)}_\mu N_{(K)(d)} + e^{(x)}_\mu N_{(x)(d)} + e^{(y)}_\mu N_{(y)(d)} \right) \tag{5.76}$$

$$= \bar{e}^\mu_{(A)} \left(-v_\mu N_{(t)(d)} - (\frac{k_\mu}{k_\alpha v^\alpha} + v_\mu) N_{(K)(d)} + e^{(x)}_\mu N_{(x)(d)} + e^{(y)}_\mu N_{(y)(d)} \right); \tag{5.77}$$

since $\bar{e}^\mu_{(A)} k_\mu = 0$,

$$= \bar{e}^\mu_{(A)} \left(-v_\mu (N_{(t)(d)} + N_{(K)(d)}) + e^{(x)}_\mu N_{(x)(d)} + e^{(y)}_\mu N_{(y)(d)} \right). \tag{5.78}$$

Expanding again,

$$= \bar{e}^\mu_{(A)} \left(-v_\mu (e^\alpha_{(t)} e^\beta_{(d)} N_{\alpha\beta} + e^\alpha_{(K)} e^\beta_{(d)} N_{\alpha\beta}) + e^{(x)}_\mu N_{(x)(d)} + e^{(y)}_\mu N_{(y)(d)} \right). \tag{5.79}$$

$$= \bar{e}^\mu_{(A)} \left(-v_\mu (e^\alpha_{(t)} + e^\alpha_{(K)}) e^\beta_{(d)} N_{\alpha\beta} + e^{(x)}_\mu N_{(x)(d)} + e^{(y)}_\mu N_{(y)(d)} \right). \tag{5.80}$$

but

$$(e^\alpha_{(t)} + e^\alpha_{(K)}) N_{\alpha\beta} = (v^\alpha - (k^\alpha/(k_\lambda k^\lambda) + v^\alpha)) N_{\alpha\beta} = 0 \tag{5.81}$$

since $k^\alpha N_{\alpha\beta} = 0$. Then

$$\bar{e}^\mu_{(A)} e^{(c)}_\mu N_{(c)(d)} = \bar{e}^\mu_{(A)} e^{(B)}_\mu N_{(B)(d)} \tag{5.82}$$

Assembling the entire expression

$$\bar{N}_{(A)(B)} = \bar{e}^\mu_{(A)} \bar{e}^\nu_{(B)} e^{(C)}_\mu e^{(D)}_\nu N_{(C)(D)} \tag{5.83}$$

that is, the change of frame simply interchanges components in the spatial plane

perpendicular to K^α. Since Q^2+U^2, V^2, and I are invariant, this transformation corresponds to a rotation that interchanges Q and U (or changes the sign of V if the handedness of the tetrad is allowed to change).

For completeness, express the transformation of the Stokes parameters in terms of $e^\mu_{(A)}$ and $\bar{e}^\mu_{(A)}$ via:

$$\bar{Q} = Q\cos 2\theta - U\sin 2\theta \tag{5.84}$$

$$\bar{U} = U\cos 2\theta + U\sin 2\theta \tag{5.85}$$

where $\cos\theta \equiv \bar{e}^\mu_{(x)} e^{(x)}_\mu$ and $\sin\theta \equiv \bar{e}^\mu_{(x)} e^{(y)}_\mu$.

Evidently no measurement depends on the correlations $\langle \phi a_i^* \rangle$. At a single event we can change frames at will, resetting ϕ to zero in any frame we choose. We cannot set $\phi = 0$ while transporting $N^{\mu\nu}$ along a ray.

5.9 Polarized transport in a tetrad basis

What is the transport equation in a tetrad basis? Project the right hand side of Eq. (5.62) onto the tetrad basis:

$$J^{(a)(b)} + H^{(a)(b)(c)(d)} N_{(c)(d)}. \tag{5.86}$$

The left side is

$$e^{(a)}_\mu e^{(b)}_\nu k^\alpha \nabla_\alpha \left(N^{(c)(d)} e^\mu_{(c)} e^\nu_{(d)} \right) = \frac{dN^{(a)(b)}}{d\lambda} + e^{(a)}_\mu e^{(b)}_\nu N^{(c)(d)} k^\alpha \nabla_\alpha \left(e^\mu_{(c)} e^\nu_{(d)} \right). \tag{5.87}$$

The final term can be rewritten

$$N^{(c)(d)} \left(\delta^a_c \, e^{(b)}_\nu k^\alpha \nabla_\alpha e^\nu_{(d)} + \delta^b_d \, e^{(a)}_\mu k^\alpha \nabla_\alpha e^\mu_{(c)} \right) \equiv N^{(a)(d)} c^{(b)}_{(d)} + N^{(c)(b)} c^{(a)}_{(c)}. \tag{5.88}$$

This defines the rotation coefficients $c^{(a)}_{(b)}$. The full transport equation in a tetrad basis is then

$$\frac{dN^{(a)(b)}}{d\lambda} + N^{(a)(d)} c^{(b)}_{(d)} + N^{(c)(b)} c^{(a)}_{(c)} = J^{(a)(b)} + H^{(a)(b)(c)(d)} N_{(c)(d)} \tag{5.89}$$

Differentiating $e^{(a)}_\mu e^\mu_{(b)} = \delta^{(a)}_{(b)}$, we conclude that $e^{(a)}_\nu (k^\alpha \nabla_\alpha) e^\nu_{(b)} = -e^{(b)}_\nu (k^\alpha \nabla_\alpha) e^\nu_{(a)}$, so $c^{(a)}_{(b)}$ is antisymmetric.

In the plasma basis, then, $c^{(\perp)}_{(\parallel)} = -c^{(\parallel)}_{(\perp)}$ (recall that indices are raised and lowered in the tetrad basis using the Minkowski metric). For a tetrad basis that is parallel transported along the ray, $k^\alpha \nabla_\alpha e^\nu_{(a)} = 0$ and the rotation coefficients vanish.

5.10 Equivalence to Broderick & Blandford [2004] formalism

We can now derive Eqs. (17) and (18) of BB04. Notice that BB04's $N_Q = C(N^{(\parallel)(\parallel)} - N^{(\perp)(\perp)})$ where C is a constant. Then

$$\frac{dN_Q}{d\lambda} = C\left(\frac{dN^{(\parallel)(\parallel)}}{d\lambda} - \frac{dN^{(\perp)(\perp)}}{d\lambda}\right) \tag{5.90}$$

and, assuming $J = H = 0$ (vacuum),

$$\frac{dN_Q}{d\lambda} = C\left(-N^{(\parallel)(a)}c^{(\parallel)}_{(a)} - N^{(a)(\parallel)}c^{(\parallel)}_{(a)} + N^{(\perp)(a)}c^{(\perp)}_{(a)} + N^{(a)(\perp)}c^{(\perp)}_{(a)}\right). \tag{5.91}$$

Expanding the first term,

$$N^{(\parallel)(a)}c^{(\parallel)}_{(a)} = N^{(\parallel)(t)}c^{(\parallel)}_{(t)} + N^{(\parallel)(\parallel)}c^{(\parallel)}_{(\parallel)} + N^{(\parallel)(\perp)}c^{(\parallel)}_{(\perp)} + N^{(\parallel)(K)}c^{(\parallel)}_{(K)}. \tag{5.92}$$

Antisymmetry implies $c^{(\parallel)}_{(\parallel)} = 0$. Notice that

$$N^{(\parallel)(t)} = N^{(\parallel)(K)} \tag{5.93}$$

since $k_{(a)} = \{-K, 0, 0, K\}$ and $k_{(a)}N^{(a)(b)} = 0$, so

$$N^{(\parallel)(a)}c^{(\parallel)}_{(a)} = N^{(\parallel)(t)}\left(c^{(\parallel)}_{(t)} + c^{(\parallel)}_{(K)}\right) + N^{(\parallel)(\perp)}c^{(\parallel)}_{(\perp)}. \tag{5.94}$$

The term in parentheses is

$$e^{(\parallel)}_{\mu}(k^{\alpha}\nabla_{\alpha})\left(e^{\mu}_{(t)} + e^{\mu}_{(K)}\right) = e^{(\parallel)}_{\mu}(k^{\alpha}\nabla_{\alpha})\left(-\frac{k^{\mu}}{k_{\nu}u^{\nu}}\right) = e^{(\parallel)}_{\mu}k^{\mu}(k^{\alpha}\nabla_{\alpha})\left(-\frac{1}{k_{\nu}u^{\nu}}\right) = 0 \tag{5.95}$$

where the penultimate equality follows from $(k^{\alpha}\nabla_{\alpha})k^{\mu} = 0$ and the final equality follows from $e^{(\parallel)}_{\mu}k^{\mu} = 0$. Then $N^{(\parallel)(a)}c^{(\parallel)}_{(a)} = N^{(\parallel)(\perp)}c^{(\parallel)}_{(\perp)}$. Similar considerations for the other terms in Eq. (5.91) yield

$$\frac{dN_Q}{d\lambda} = C\left(-N^{(\parallel)(\perp)}c^{(\parallel)}_{(\perp)} - N^{(\perp)(\parallel)}c^{(\parallel)}_{(\perp)} + N^{(\perp)(\parallel)}c^{(\perp)}_{(\parallel)} + N^{(\parallel)(\perp)}c^{(\perp)}_{(\parallel)}\right) \tag{5.96}$$

Identify our $c_{(\perp)(\parallel)}$ with $-d\phi/d\lambda$ of BB04 (substitute λ for τ in BB04 Eq. (17)), and set BB04's $N_U = C(N^{(\parallel)(\perp)} + N^{(\perp)(\parallel)})$ to find

$$\frac{dN_Q}{d\lambda} = -2\frac{d\phi}{d\lambda}N_U, \tag{5.97}$$

which is the first of the two equations (18) in BB04; the second follows from a very similar calculation. The term $d\phi/d\lambda$ accounts for interconversion of Stokes Q and U due to rotation of the basis vectors around the K^α axis.

The sign of V is coordinate dependent since it can change if the handedness of the coordinate system changes. The plasma basis used here (identical to that used by BB04) has a definite handedness and so the sign of V does not change sign if the sign of b^μ changes; this is the only other possible frame dependent change in the invariant Stokes parameters along the ray.

5.11 Numerical approaches

Strategies for integrating the transport equation numerically can be classified according to the choice of dependent variables. Almost every integration strategy will require calculating the emissivity tensor J and the absorptivity tensor H in the plasma basis and transforming it to whatever basis is being used for N; this requires constructing the plasma basis at each point along the ray.

5.11.1 $N^{\mu\nu}$ in a coordinate basis

The conceptually simplest approach is to directly integrate $N^{\mu\nu}$ (16 real degrees of freedom) in the coordinate frame.

Procedure: (1) at each point along the ray construct a plasma tetrad $e^\mu_{(a)}$; (2) calculate J and H (or Π) in the plasma frame; (3) transform J and H to the coordinate frame; (4) calculate $\Gamma^\kappa_{\alpha\beta}$ (coordinate frame); (5) step the radiative transfer equation:

$$k^\alpha \nabla_\alpha N^{\mu\nu} = \frac{dN^{\mu\nu}}{d\lambda} + \Gamma^\mu_{\alpha\beta}N^{\alpha\nu}k^\beta + \Gamma^\nu_{\alpha\beta}N^{\mu\alpha}k^\beta = J^{\mu\nu} + H^{\mu\nu\kappa\lambda}N_{\kappa\lambda}; \tag{5.98}$$

Final measurement (at large radius) is done by casting $N^{\mu\nu}$ onto a tetrad basis, then converting (if desired) to Stokes parameters.

A disadvantage of this scheme is that all tensors in the above equation are full four-dimensional tensors.

5.11.2 $N^{(A)(B)}$ in the plasma tetrad

This is equivalent to BB04's elegant approach in which the dependent variables are the invariant intensities for each of the Stokes parameters (e.g. $N_Q \propto Q/\nu^3$).

Procedure: (1) construct the plasma tetrad; (2) calculate J and H in the plasma tetrad; (3) calculate $\Gamma^{\kappa}_{\alpha\beta}$; (4) evaluate the rotation coefficient $d\phi/d\lambda$; (5) step the radiative transfer equation

$$\frac{dN^{(A)(B)}}{d\lambda} = J^{(A)(B)} + H^{(A)(B)(C)(D)}N_{(C)(D)} + R^{(A)(C)}R^{(B)(D)}N_{(C)(D)} \tag{5.99}$$

forward ($R_{(A)(B)}$ accounts for interconversion of Stokes Q and U due to rotation of the basis vectors along the photon trajectory). The indices (A) indicate that only the (x) and (y) components of each tensor are required.

A potential weakness of this approach is that it may be difficult to evaluate $d\phi/d\lambda$ accurately when the velocity and magnetic field are specified numerically. If fluctuating magnetic and velocity fields cause the basis vectors to rotate rapidly then truncation error may be enhanced, leading to spurious interconversion of Stokes Q and U and ultimately inaccurate polarization angles.

5.11.3 $N^{(A)(B)}$ in a parallel transported tetrad

Again there are four dependent variables for the radiation field. Any orthonormal tetrad basis can be parallel transported along the ray, but a natural choice is the observer tetrad. In practice only two basis vectors are needed ($e_{(x)}$ and $e_{(y)}$), so there are a total of twelve dependent variables.

Procedure: (1) construct the plasma tetrad; (2) calculate J and H in the plasma tetrad; (3) calculate $\Gamma^{\kappa}_{\alpha\beta}$; (4) step the needed components of the orthonormal tetrad forward; (5) project J and H onto the tetrad basis; (6) step the radiative transfer equation:

$$\frac{dN^{(A)(B)}}{d\lambda} = J^{(A)(B)} + H^{(A)(B)(C)(D)}N_{(C)(D)} \tag{5.100}$$

forward. Final measurement is trivial.

This approach simplifies some aspects of the transport equation at the cost of introducing another set of dependent variables (the tetrad basis vectors) that must be parallel transported along the ray. This tetrad does not depend on the fluid variables, however, so it will rotate smoothly along the ray.

5.12 Summary

We have described a framework for covariant polarized radiative transport. The basic object that describes the polarization is the polarization tensor $N^{\mu\nu}$, defined in Eq. (5.59). Given absorption, Faraday rotation, and emission coefficients in the plasma frame, one can then calculate absorption and emission tensors in the coordinate frame (see §7). The transport equation (5.62) can then be integrated directly in the coordinate basis, or in an orthonormal tetrad.

5.13 References

Aitken, D. K., Greaves, J., Chrysostomou, A., Jenness, T., Holland, W., Hough, J. H., Pierce-Price, D., Richer, J. 2000, ApJ, 534, 173

Anderson, J. L., & Spiegel, E. A. 1972, ApJ, 171, 127

Anile, A. M. 1989, Relativistic Fluids and Magneto-fluids (Cambridge: Cambridge)

Anile, A. M., & Breuer, R. A. 1974, ApJ, 189, 39

Bildhauer, S. 1989, Class. Quantum Grav., 6, 1171

Bildhauer, S. 1989, A&A, 219, 25

Breuer, R. A., & Ehlers, J. 1980, Proc. R. Soc. Lond., 370, 389

Breuer, R. A., & Ehlers, J. 1981, Proc. R. Soc. Lond., 374, 65

Broderick, A. E., & Blandford, R. 2004, MNRAS, 349, 994

Broderick, A. E. 2006, MNRAS, 366, L10

Broderick, A. E., Loeb, A., & Narayan, R. 2009, ApJ, 701, 1357

Challinor, A. 2000, General Relativity and Gravitation, 32, 1059

Connors, P. A., Piran, T., & Stark, R. F. 1980, ApJ, 235, 224

Dautcourt, G., & Rose, K. 1978, Astron. Nachr., 299, 13

Dovčiak, M., Muleri, F., Goosmann, R. W., Karas, V., & Matt, G. 2008, MNRAS, 391, 32

Gammie, C. F., & Leung, P. K. 2010, in preparation

Gedalin, M., & Melrose, D. B. 2001, Phys. Rev. E, 64, 027401

Huang, L., Liu, S., Shen, Z.-Q., Yuan, Y.-F., Cai, M. J., Li, H., & Fryer, C. L. 2009, ApJ, 703, 557

Jackson, J. D. 1975, Classical Electrodynamics (2nd ed.; New York: Wiley)

Kosowsky, A. 1994, Ph.D. thesis, Chicago Univ.

Kosowsky, A. 1996, Ann. Phys., 246, 49

Leung, P. K., Gammie, C. F., & Noble, S. C. 2009, ApJ, submitted

Li, L.-X., Zimmerman, E. R., Narayan, R., & McClintock, J. E. 2005, ApJS, 157, 335

Lindquist, R. W. 1966, Annals of Physics, 37, 487

Marrone, D. P., Moran, J. M., Zhao, J.-H., & Rao, R. 2006, ApJ, 640, 308

Marrone, D. P., Moran, J. M., Zhao, J.-H., & Rao, R. 2007, ApJ, 654, 57

Melrose, D. B. 1980, Plasma Astrophysics (New York: Gordon and Breach)

Melrose, D. B., & McPhedran, R. C. 1991, Electromagnetic Processes in Dispersive Media (Cambridge: Cambridge)

Melrose, D. B. 2008, Quantum Plasmdynamics: Unmagnetized Plasmas (New York: Springer)

Melrose, D. B. 2009, Quantum Plasmdynamics II. Magnetized Plasmas (unpublished, obtained from author's website in July 09)

Misner, C. W., Thorne, K. S., & Wheeler, J. A. 1973, Gravitation (New York: Freeman)

Schnittman, J. D., & Krolik, J. H. 2009, ApJ, 701, 1175

Shcherbakov, R. V. 2008, ApJ, 688, 695

Thorne, K. S. 1981, MNRAS, 194, 439

Weinberg, S. 2008, Cosmology (Oxford: Oxford)

Appendix A

A.1 Additional Doppler factor in emissivity

There is some confusion in the literature about the expression for the single-electron emissivity, which can be calculated directly from Maxwell's equations [see Bekefi, 1966]. This confusion is connected to discussions of the distinction between received and emitted power first noted by Ginzburg & Syrovatskii [1968] and by Pacholczyk [1970], and discussed by Scheuer [1968], Rybicki & Lightman [1979, §6.7] and very clearly by Blumenthal & Gould [1970, §4.3, 4.4]. So, for example, Wardzinski & Zdziarski [2000, Sec. 2.1] state that an additional Doppler factor $(1 - \beta\mu\cos\theta)^{-1}$ should have appeared in their expression for the single-electron emissivity η_ν (see their equation 1), but that this factor "disappears in the case of an electron moving chaotically." Here we show there is no such factor.[1]

To find the emissivity for a distribution of electrons we need to integrate the single-electron emissivity against the distribution function over momentum space:

$$j_\nu = \int d^3p_e \frac{dN_e}{d^3p_e d^3x}\,\eta_\nu(\mathbf{p}_e) \tag{A.1}$$

where $\mathbf{p}_e$ is the electron momentum. To evaluate j_ν, we need η_ν for an electron with nonzero momentum parallel to $\mathbf{B}$, measured in the plasma rest frame. This can be calculated directly [see, e.g., Bekefi, 1966]. Here we start with the single-electron emissivity for an electron with zero momentum parallel to $\mathbf{B}$ and show explicitly that, by Lorentz boosts, one obtains the usual expression for the single-electron emissivity for an electron with nonzero momentum parallel to $\mathbf{B}$. The emissivity of a distribution of electrons in frames other than the fluid (plasma center-of-momentum) frame can then be obtained using the Lorentz invariance of j_ν/ν^2.

Here is our strategy: identify the wavevector and electron four-momentum in the fluid frame (denoted [FF]), then transform these to a frame comoving with the electron's guiding center (denoted [GCF], and also denoted by primes) and use the resulting expressions for the photon wavevector and electron four-velocity to obtain η_ν in the guiding center frame. Finally, transform η_ν back to the fluid frame.

[1] Appendices A.1 and A.2 were originally parts of chapter 3, which was submitted in 2009 to ApJ [Leung, Gammie & Noble, 2009]. Reproduction for this dissertation is authorized by the copyright holder.

The photon wavevector is ($\omega = 2\pi\nu$)

$$k^\mu[\mathrm{FF}] = \{\omega, \omega\sin\theta, 0, \omega\cos\theta\} \tag{A.2}$$

in a coordinate frame t, x, y, z. We assume, without loss of generality, that the wavevector lies in the x-z plane and the magnetic field is aligned with $\hat{z}$. The electron four-velocity is

$$u^\mu[\mathrm{FF}] = \{\gamma, \gamma\beta\sin\xi, 0, \gamma\beta\cos\xi\} \tag{A.3}$$

where ξ is the electron pitch angle. As the time-averaged emission is invariant under rotations about $\hat{z}$, we have chosen an instant of time at which the electron's velocity is (spatially) coplanar with k^μ and the magnetic field.

Now apply a Lorentz boost parallel to the magnetic field, transforming into the frame comoving with the electron guiding center:

$$\Lambda = \begin{pmatrix} \gamma_g & 0 & 0 & -\beta_g\gamma_g \\ 0 & 1 & 0 & 0 \\ 0 & 0 & 1 & 0 \\ -\beta_g\gamma_g & 0 & 0 & \gamma_g \end{pmatrix} \tag{A.4}$$

where β_g is the guiding center speed along the field line, which is $\beta\cos\xi$; the corresponding Lorentz factor is $\gamma_g^{-2} = 1 - \beta^2\cos^2\xi$.

The boosted wavevector is

$$k^\mu[\mathrm{GCF}] = \omega\{\gamma_g(1 - \beta_g\cos\theta), \sin\theta, 0, \gamma_g(\cos\theta - \beta_g)\} \tag{A.5}$$

from which we deduce that

$$\nu' = \nu\gamma_g(1 - \beta_g\cos\theta) \tag{A.6}$$

(the prime denotes the value in the [GCF]) and

$$\sin\theta' = \frac{\sin\theta}{\gamma_g(1 - \beta\cos\xi\cos\theta)} \tag{A.7}$$

and

$$\cot^2\theta' = \gamma_g^2\left(\frac{\beta\cos\xi - \cos\theta}{\sin\theta}\right)^2 . \tag{A.8}$$

The boosted four-velocity is

$$u^{\mu}[\mathrm{GCF}] = \gamma\{\gamma_g(1 - \beta\beta_g\cos\xi), \beta\sin\xi, 0, 0\} \tag{A.9}$$

from which we conclude that

$$\gamma' = \frac{\gamma}{\gamma_g} \tag{A.10}$$

and

$$\beta' = \beta\gamma_g\sin\xi\ . \tag{A.11}$$

In the guiding center frame the single-electron emissivity is [Schott, 1912]

$$\eta_{\nu}[\mathrm{GCF}] \equiv \frac{dE'}{dt'd\Omega'd\nu'} = \frac{2\pi e^2\nu'^2}{c}\sum_{n=1}^{\infty}\delta(y'_n)\left[\cot^2\theta' J_n^2(z) + \beta^2 J_n'^2(z)\right] \tag{A.12}$$

where

$$y'_n \equiv \frac{n\nu_c}{\gamma'} - \nu'\ , \tag{A.13}$$

$$z = \frac{\nu'\beta'\gamma'}{\nu_c}\sin\theta'\ , \tag{A.14}$$

and $d\Omega'$ is the differential solid angle in [GCF].

We can evaluate all the arguments of η_{ν}[GCF] in terms of [FF]quantities:

$$y'_n = \frac{n\nu_c}{\gamma'} - \nu' = \gamma_g\left(\frac{n\nu_c}{\gamma} - \nu(1 - \beta\cos\xi\cos\theta)\right) = \gamma_g y_n\ , \tag{A.15}$$

since the field strength (and therefore ν_c) is the same in both frames and y_n is defined in equation (3.17). Now

$$\delta(y'_n) = \delta(\gamma_g y_n) = \frac{1}{\gamma_g}\delta(y_n)\ . \tag{A.16}$$

Also (after substitution),

$$z = \frac{\nu'\beta'\gamma'}{\nu_c}\sin\theta' = \frac{\nu\beta\gamma}{\nu_c}\sin\theta\sin\xi\ , \tag{A.17}$$

which recovers equation (3.18). We have evaluated η_{ν}[GCF] in terms of quantities

measured in the fluid frame:

$$\eta_\nu[\mathrm{GCF}] = \frac{2\pi e^2 \nu'^2}{c} \sum_{n=1}^{\infty} \frac{1}{\gamma_g} \delta(y_n) \left[\gamma_g^2 \left(\frac{\cos\theta - \beta\cos\xi}{\sin\theta} \right)^2 J_n^2(z) + \beta^2 \sin^2\xi \gamma_g^2 J_n'^2(z) \right] \tag{A.18}$$

and we now need to find $\eta_\nu[\mathrm{FF}]$.

Since

$$\eta_\nu = \frac{dE}{dt d\Omega d\nu} = h\nu^2 \frac{dN}{\nu dt d\Omega d\nu} \tag{A.19}$$

and $\nu d\Omega d\nu$, dN are invariant, then

$$\frac{\eta'_\nu}{\nu'^2} dt' = \frac{\eta_\nu}{\nu^2} dt \ . \tag{A.20}$$

Since $dt'/dt = 1/\gamma_g$ (exercise for the reader), we are left with

$$\eta_\nu[\mathrm{FF}] = \frac{2\pi e^2 \nu^2}{c} \sum_{n=1}^{\infty} \delta(y'_n) \left[\left(\frac{\cos\theta - \beta\cos\xi}{\sin\theta} \right)^2 J_n^2(z) + \beta^2 \sin^2\xi J_n'^2(z) \right] \tag{A.21}$$

which is the usual expression, as given by Wardzinski & Zdziarski [2000] and Bekefi [1966], obtained by transformation rather than direct calculation.

A.2 Efficient Bessel Function Calculator

In order to evaluate the accuracy of approximate formulae for the synchrotron emissivity we must compare them to the exact expression (3.32), which includes the Bessel function of the first kind $J_n(z)$ [Abramowitz & Stegun, 1970]. The function is a solution of the differential equation

$$\left[z^2 \frac{d^2}{dz^2} + z \frac{d}{dz} + \left(z^2 - n^2\right) \right] J_n = 0 \tag{A.22}$$

and has the series representation

$$J_n(z) = \left(\frac{z}{2}\right)^n \sum_{k=0}^{\infty} \frac{(-1)^k \left(z/2\right)^{2k}}{k!\,\Gamma(n+k+1)} \ . \tag{A.23}$$

In our application, the order of the Bessel function is set by the resonance condition (3.17). Both z and n vary from 10^2 to $\sim 10^{13}$ for our target application [Noble et al., 2007]. Since our evaluation of $j_\nu(\theta)$ requires us to evaluate a two-dimensional

integral repeatedly, many evaluations of $J_n(z)$ are required. Further, the number of $J_n(z)$ calculations needed for the two-dimensional integral and the run-time per $J_n(z)$ evaluation using standard packages increases with ν/ν_c. This study therefore demanded we use an efficient $J_n(z)$ calculator accurate enough so that the final error in $j_\nu(\theta)$ is less than the error of our approximate expressions.

Facing the same computational hurdle as us, Chishtie et al. [2005]—who require large order calculations of $J_n(z)$ to high precision for Fourier transforming gravitational wave signals from pulsars—expanded further previously known approximate expansions for $J_n(z)$ in various limits. We demonstrate here for the first time that these expressions can be pieced together to form a continuous approximation for $J_n(z)$ up to $n \sim 10^{55}$. We do not use the more recent method described in Chishtie et al. [2008]—which is said to work over all limits in z/n—since it requires evaluating the Airy function and its derivative. The expressions given in Chishtie et al. [2005] satisfy our needs, were straightforward to implement, and relieved us from searching for a robust, efficient Airy function routine.

Our method uses three different approximate expansions, which we will call "Expansions 1-3", for three different domains: $z < n - d_1$, $z \sim n$, and $z > n + d_2$, where $d_{1,2}$ are functions of n given below. Expansions 1 and 3 use two-order extensions made by Chishtie et al. [2005] to expansions derived originally by Meissel (see Chishtie et al. [2005] for references to original works on the various series representations of $J_n(z)$). Specifically, we use equations (10-12) of Chishtie et al. [2005] for Expansion 1, and equations (12-14) of Chishtie et al. [2005] for Expansion 3. Expansion 2 is used in the so-called transition region, $z \sim n$, and is a five-term extension of Debye's "ϵ expansion" given in equations (21-22) of Chishtie et al. [2005].

The extensions made by Chishtie et al. [2005] were essential to being able to match the expansions together for all n. We empirically found the locations—i.e. $z(n)$—at which an expansion starts to deviate by more than 0.1% from trusted values[2] over $100 < n < 10^7$. These locations $z(n)$ fit the following functions well:

$$z_- = n\,(1 - b_- n^{a_-}) \quad \text{for } z < n \tag{A.24}$$

$$z_+ = n\,(1 - b_+ n^{a_+})^{-1} \quad \text{for } z > n \tag{A.25}$$

with $a_\pm$ and $b_\pm$ being different constants for each expansion. We found that each expansion's region of validity (to 0.1% level) overlaps with another expansion's valid

[2]The routine used to calculate the trusted values was the `jn` routine found in the GNU C compiler's math library [GNU Compiler Collection].

range, suggesting that at least one out of the three expansions is valid for any n, z. The boundaries dictating which expansion to use were finally chosen to be curves centered between neighboring methods' curves of validity. The curve marking the boundary between the first and second domains is

$$z_{12} = z_- \quad : \quad (a_-, b_-) \simeq (-0.66563, 1.8044) \tag{A.26}$$

and the curve separating the second and third domains is

$$z_{23} = z_+ \quad : \quad (a_+, b_+) \simeq (-0.65430, 1.8708) \ . \tag{A.27}$$

One can show that, with 32-bit double precision floating-point arithmetic, these curves are numerically indistinguishable from the curve $z = n$ for $n \gtrsim 10^{23}$; at these orders Expansion 2 is used only when $z = n$. For $n \gtrsim 10^{26}$, $J_n(z < n)$ is numerically equivalent to zero for any z numerically different from n since the function $J_n(z < n)$ becomes narrower as n increases. One may, however, resolve this issue by working in higher precision environments. Fortunately, our applications do not require us to do so since we are only interested in $n < 10^{14}$.

We have written a routine in the C programming language called `my_Bessel_J` that controls when to use which expansion and efficiently evaluates the appropriate expansion[3]. It has been extensively tested against a number of other routines, which we list in Table A.1. All tests were performed on an Intel 3.06GHz Xeon machine with the Intel C++ Compiler for Linux Version 8.0 and the GNU C Compiler Version 3.3.2.

Table A.1 Routines for Evaluating the Bessel Function $J_n(z)$. $n_{\max}$ is the approximate maximum value of n a outine can calculate $J_n(n)$ to within 10% of the value from `my_Bessel_J`.

Name	Reference	$n_{\max}$
`my_Bessel_J`	This paper, [Chishtie et al., 2005]	—
`bessjy`	[Press et al., 1992]	10^{16}
`gsl_sf_bessel_Jn`	[Galassi, 2006]	10^5
`jn`	[GNU Compiler Collection]	10^9
`s17dec`	[NAG C Library]	10^9

[3]Our routine and an example program are available to the public under the GNU Public License from the web at `http://rainman.astro.uiuc.edu/codelib/`.

Our first comparison attempts to measure the maximum value of n for which a routine can reliably calculate the Bessel function. In Table A.1, we list the order of magnitude of n at which each method's evaluation of $J_n(n)$ begins to significantly deviate from our method's values at certain n. For small order we are confident in our method since all methods agree with each other. At orders $n > 10^9$, however, only one other method is reliable (`bessjy`) and so the comparison is biased. At their limits, each method "fails" to return with a reasonable answer in different ways. Some return with obviously wrong values like $J_n(n) < 0$ (`gsl_sf_bessel_Jn` and `jn`), another reports that there is a loss of precision and returns with a null answer (`s17dec`), while the last reports that the calculation requires too many iterations and gives an inaccurate approximation (`bessjy`). Note that we are not confident in our method for $n > 10^{55}$ since this is when Expansion 2 evaluates $J_n(n) = 0$.

This survey shows that there is an existing method, `bessjy`, that can reliably calculate $J_n(n)$ at orders well above our requirements. Unfortunately, as we see in Figure (A.1), it is costly and scales as a power-law with n. `jn` has a steeper power-law scaling, while the others are practically independent of the Bessel function's order[4]. All but `gsl_sf_bessel_Jn` are significantly slower than our routine; `gsl_sf_bessel_Jn`, however, has the smallest domain of validity and cannot evaluate $J_n(z)$ at the values of n we need.

In Figure (A.2) we compare $J_n(z)$ at $n = 10^9$ to see how the three best methods compare with each other at large order over a wide range in argument. The fact that `my_Bessel_J` agrees better with `s17dec` than does `bessjy` gives credence to our method. The imperfectness of the transitions from one expansion to another exhibits itself by narrow peaks in the relative error between `my_Bessel_J` and the other methods. These peaks lie immediately about the transition points, which are indicated by the dashed vertical lines. As z increases past n, round-off errors lead to significant phase errors. `my_Bessel_J` and `s17dec` both follow the asymptotically sinusoidal trend at large z, but `bessjy` eventually returns with 0 and indicates that it has reached its reliable limit.

To measure the accuracy at even larger order, we employ the recurrence relation

$$\frac{2n}{z} J_n(z) = J_{n-1}(z) - J_{n+1}(z) \tag{A.28}$$

[4]The runtime for `s17dec` is constant up to $n \sim 10^4$, after which it is a larger constant.

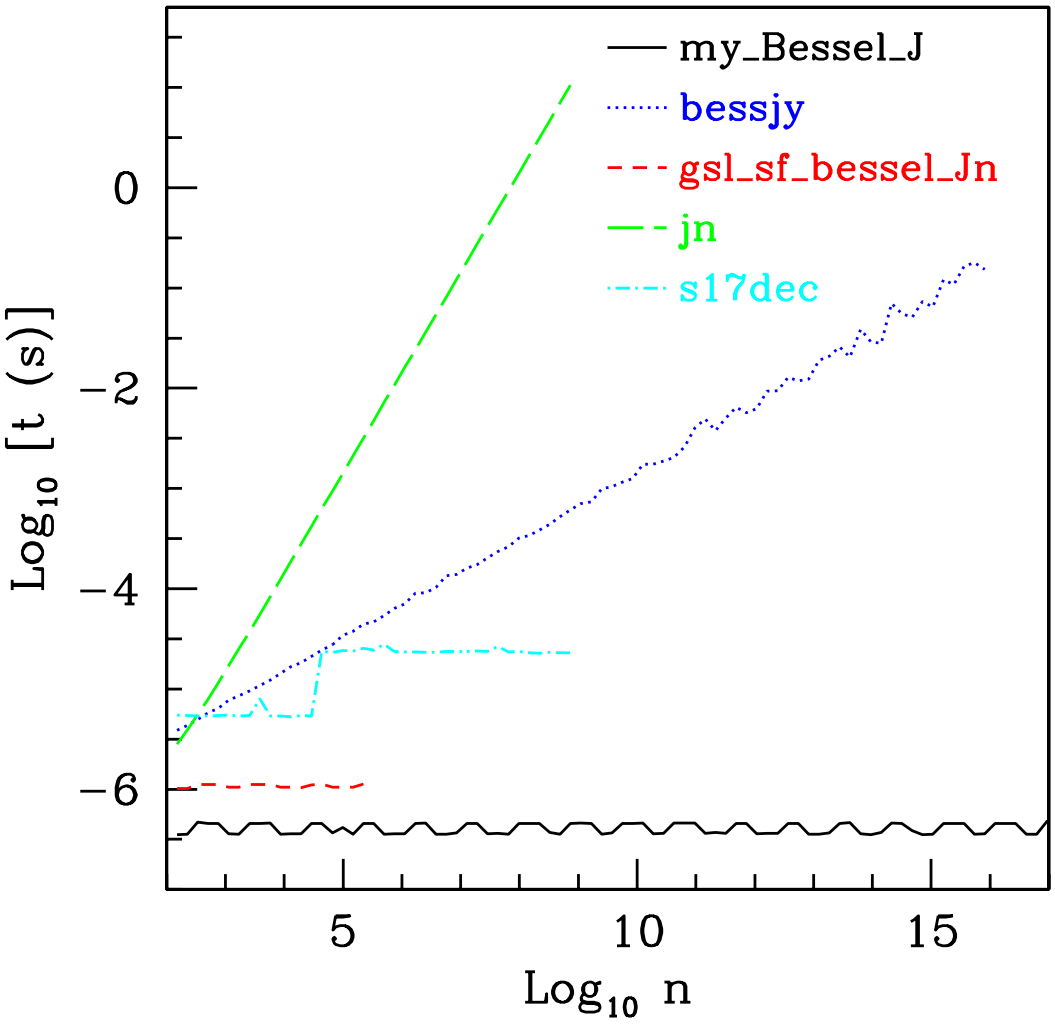

Figure A.1 The logarithm of the time per $J_n(n)$ execution in seconds versus n using the methods listed in Table A.1. A method's execution time was only measured up to its $n_{\max}$. Note that the execution time of `my_Bessel_J` remains steady through $n = 10^{55}$; the plot was truncated for illustrative purposes.

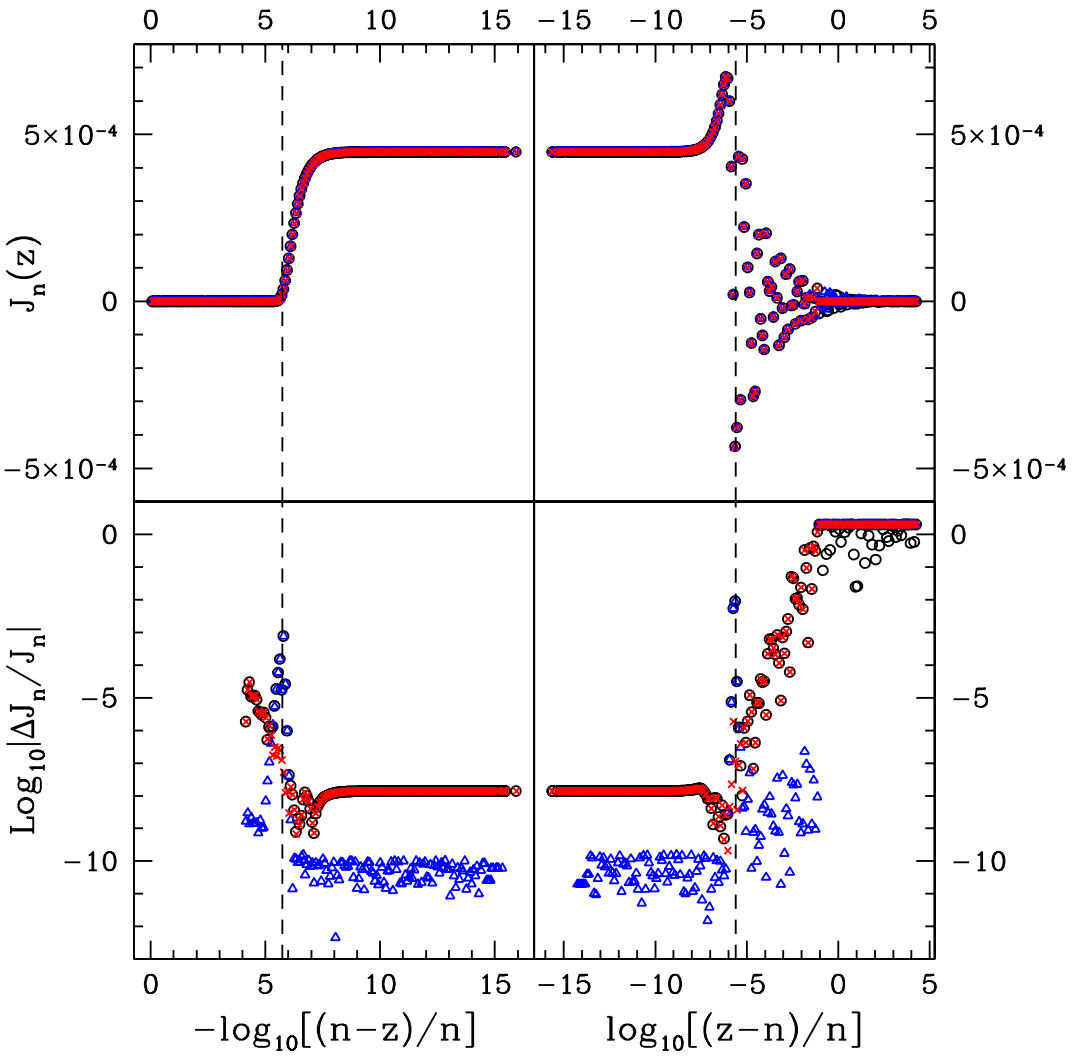

Figure A.2 Comparison between $J_n(z)$ evaluations when $n = 10^9$. Top row: $J_n(z)$ using `my_Bessel_J` (circles), `bessjy` (triangles), and `s17dec` (exes). Bottom row: the logarithm of the relative error between `my_Bessel_J` and `bessjy` (circles), `my_Bessel_J` and `s17dec` (triangles), and `bessjy` and `s17dec` (exes). The plots on the left are shown for $z < n$, while those on the right are shown for $z > n$. The vertical dashed lines in the left and right plots indicate, respectively, z_- and z_+ at $n = 10^9$.

and calculate the normalized deviation from it:

$$R_n(z) = \left| \frac{1}{J_n(z)} \left(\frac{2n}{z} J_n(z) - J_{n-1}(z) - J_{n+1}(z) \right) \right| \tag{A.29}$$

which should be identically zero. We calculate $R_n(z)$ for three different arguments over a wide range of n in Figure (A.3). Each curve uses one of the three expansions. The errors in Expansion 1 and 3 both diminish with n, except when round-off errors lead to significant phase errors in Expansion 3 for $n \gtrsim 10^8$. Expansion 2, however, always satisfies the recurrence relation to within 32-bit double precision for all n. For even higher orders $n \to 10^{55}$, we have made sure that `my_Bessel_J` satisfies the well-known upper bounds [Abramowitz & Stegun, 1970]:

$$J_n(n) < \frac{[2/(9n)]^{1/3}}{\Gamma(2/3)} , \quad |J_n(z)| \leq \frac{(z/2)^n}{\Gamma(n+1)} , \quad |J_n(n\epsilon)| \leq \left| \frac{\epsilon^n \exp\left[n\sqrt{1-\epsilon^2}\right]}{\left(1+\sqrt{1-\epsilon^2}\right)^n} \right| . \tag{A.30}$$

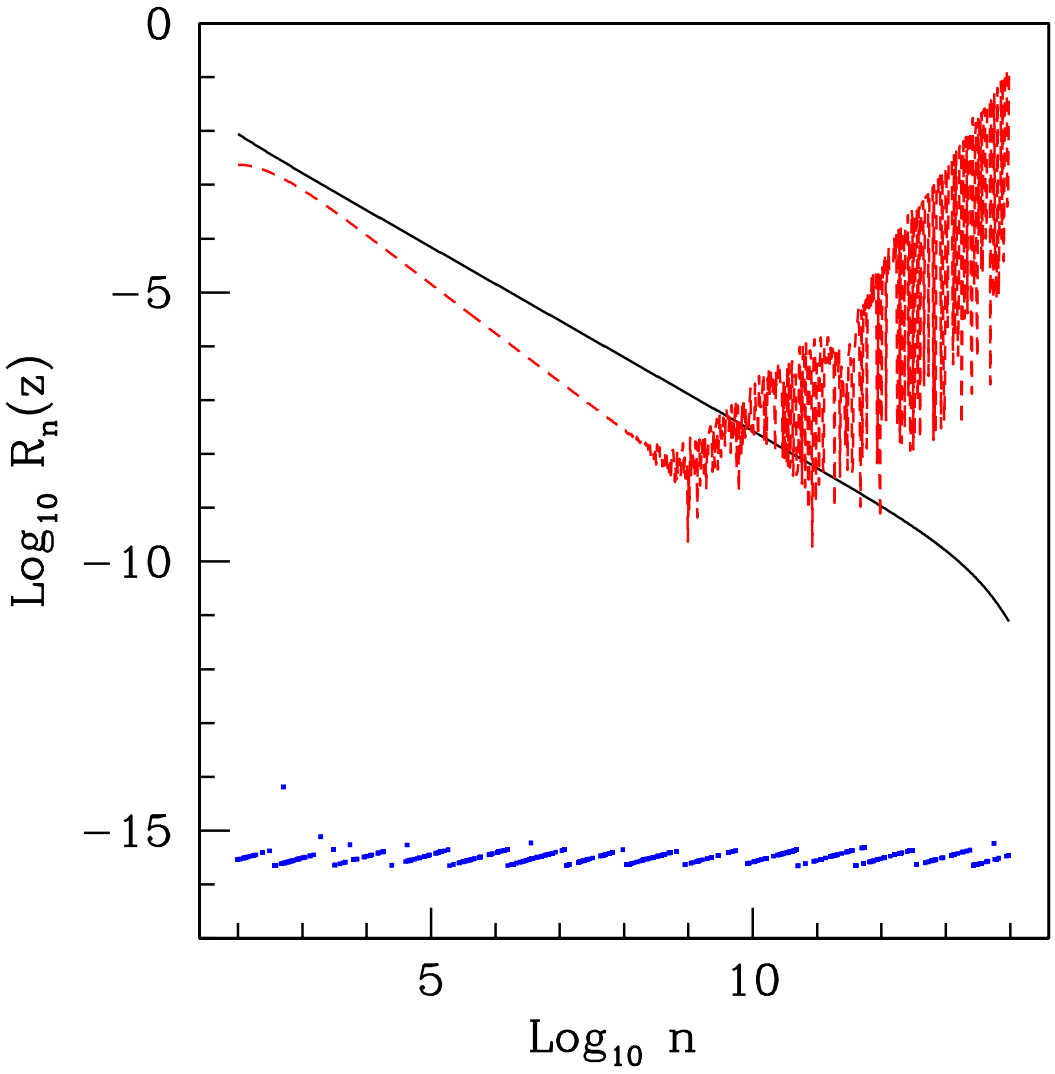

Figure A.3 The logarithm of the normalized residual of the recurrence relation for $z = (1 - \epsilon)\, z_-$ (solid curve), $z = n$ (squares), and $z = (1 + \epsilon)\, z_+$ (dashes), which—respectively—use Expansions 1-3, where $\epsilon = 10^{-13}$. Please see equation (A.29) for the definition of $R_n(z)$.

A.3 References

Abramowitz, M., & Stegun, I. A. 1970, Handbook of Mathematical Functions (New York: Wiley)

Bekefi, G. 1966, Radiation Processes in Plasmas (New York: Wiley)

Blumenthal, G. R. & Gould, R. J. 1970, Rev. of Mod. Phys., 42, 237

Chishtie, F. A., Valluri, S. R., Rao, K. M., Sikorski, D., & Williams, T. 2005, in Proceedings of the 19th Annual International Symposium on High Performance Computing Systems and Applications (HPCS 2005) (IEEE Computer Society)

Chishtie, F. A., Rao, K. M., Kotsireas, I. S., & Valluri, S. R. 2008, Inter. J. Mod. Phys. D, 17, 1197

Ginzburg, V. L. & Syrovatskii, S. I. 1968, Ap&SS, 1, 442

GNU Compiler Collection, `http://gcc.gnu.org/`

Leung, P. K., Gammie, C. F., & Noble, S. C. 2009, ApJ, submitted

Noble, S. C., Leung, P. K., Gammie, C. F., & Book, L. G., 2007, Class. Quant. Grav., 24, 259

Pacholczyk, A. G. 1970, Radio Astrophysics: Nonthermal Processes in Galactic and Extragalactic Sources (San Francisco: Freeman)

Rybicki, G. B., & Lightman, A. P. 1979, Radiative Processes in Astrophysics (New York: Wiley)

Scheuer, P. A. G. 1968, ApJ, 151, L139

Schott, G. A. 1912, Electromagnetic Radiation (Cambridge: Cambridge)

Wardzinski, G., & Zdziarski, A. 2000, MNRAS, 314, 183